Doctoral Thesis in Chemistry

Chemistry Beyond Containment

Kinetic and Mechanistic Insights into Spent Nuclear Fuel Dissolution

DANIEL OLSSON

KTH ROYAL INSTITUTE OF TECHNOLOGY

Chemistry Beyond Containment

Kinetic and Mechanistic Insights into Spent Nuclear Fuel Dissolution

DANIEL OLSSON

Academic Dissertation which, with due permission of the KTH Royal Institute of Technology, is submitted for public defence for the Degree of Doctor of Philosophy on Friday the 19th of December 2025, at 10:00 a.m. in D3, Lindstedtvägen 26, Stockholm.

Doctoral Thesis in Chemistry
KTH Royal Institute of Technology
Stockholm, Sweden 2025

TRITA-CBH-FOU-2025:36
ISBN 978-91-8106-483-4

Printed by: Universitetsservice US-AB, Sweden 2025

“The cosmos is also within us, we're made of star-stuff. We are a way for the cosmos, to know itself.”

- Carl Sagan

Abstract

Safe disposal of high-level radioactive waste is crucial for protecting human health and the environment over geological timescales. A detailed understanding of the chemical processes that govern fuel corrosion is therefore essential for reliable safety assessments. A scenario of particular concern involves groundwater intrusion following the failure of the engineered barriers designed to contain the spent fuel. In this case, groundwater in contact with the fuel becomes exposed to ionizing radiation, producing radicals and molecules that can shift the conditions from reducing to oxidizing. Among the radiolytic oxidants, hydrogen peroxide (H_2O_2) is expected to have the greatest impact on the rate of fuel oxidation. The presence of carbonate in groundwater enhances the dissolution of oxidized UO_2—the main constituent of spent nuclear fuel—through the formation of soluble uranyl–carbonate complexes. This thesis examines several aspects of the oxidative dissolution of UO_2. One aspect is the effect of uranyl ion (UO_2^{2+}) accumulation in the near-surface solution on the overall oxidation rate. It was found that increasing concentrations of UO_2^{2+} suppress H_2O_2-induced oxidation by reducing the concentration of free, reactive H_2O_2 through the formation of inert uranyl–peroxo–carbonate complexes. UO_2^{2+} was also found to affect the stability of H_2O_2 in irradiated solutions. In the presence of O_2, UO_2^{2+} can suppress the concentration of H_2O_2 through selective reduction of uranyl–peroxo–carbonate complexes by the superoxide radical. Under anoxic (N_2) atmosphere, UO_2^{2+} scavenges reducing radicals (e^-_{aq} and $H^\bullet$), which increases the H_2O_2 concentration of the γ-irradiated solution. The kinetics of carbonate-facilitated dissolution were also re-evaluated, as previous models were based on systems where oxidation and dissolution occurred simultaneously. In the absence of oxidants, dissolution itself was found to be a multistep process with an apparent activation energy of (34.8 ± 3.2) kJ mol^{-1}. The reaction order with respect to bicarbonate varied between 0.5 and 1.5 within the temperature range (283–333) K and bicarbonate concentrations of (1.3–15) mM. The dependence on the oxidation state of uranium oxide showed three distinct stages: (1) a rapid initial release of a small fraction, (2) a slower, nearly constant releases rate (independent of the remaining oxidized fraction), and (3) a gradual rate decrease as the oxidized product approached depletion. Finally, comparative studies of Pd-doped and undoped UO_2 thin films in the presence of H_2 confirmed that any uncatalyzed H2 effect is several orders of magnitude less efficient at inhibiting oxidative dissolution. Palladium was found to reduce the oxide only partially, to a U(V) intermediate, identified as UO_2OH, based on a calculated U:O atom ratio of 1:3 and an average uranium oxidation state of +5.

Key words
Deep Geological Repository, Spent nuclear fuel, Uranium dioxide, Radiolysis, Oxidative Dissolution, UO_2 Dissolution, Corrosion

Sammanfattning

Ett säkert slutförvar av radioaktivt avfall är avgörande för att skydda människors hälsa och miljön över geologiska tidskalor. En detaljerad förståelse av de processer som styr korrosionen och upplösningen av utbränt kärnbränsle är en förutsättning för robusta riskanalyser av det planerade geologiska djupförvaret. Ett scenario som särskilt beaktas är ett grundvatteninträng, till följd av nedbrytningen av de säkerhetsbarriärer som håller förvaringen intakt. I detta fall blir det inträngande vattnet exponerat för joniserande strålning från det radioaktiva bränslet. Denna bestrålning leder till radiolys av vattnet, en process som genererar reaktiva radikaler och molekyler som kan skifta förhållandena från reducerande till oxiderande. Bland de radiolysgenererade oxidanterna är det väteperoxid (H_2O_2) som förväntas ha det största inflytandet på bränslets oxidation. Karbonatjoner i grundvattnet driver upplösning av oxiderad UO_2 (huvudkomponenten i bränslet från lättvattenreaktorer) genom bildandet av lösliga uranyl-karbonat-komplex. Denna avhandling undersöker ett flertal aspekter relaterade till den oxidativa upplösningen av UO_2. En aspekt är effekten av uppbyggnaden av upplöst bränslematris (UO_2^{2+}) i vätskefasen, på den fortgående oxidationshastigheten av UO_2. Uppbyggnaden av UO_2^{2+} i vätskefasen visades hämma H_2O_2-inducerad oxidation genom en förskjutning av jämvikten från reaktiv H_2O_2 mot inerta uranyl-peroxid-karbonat-komplex. Vidare observerades at UO_2^{2+} kan både sänka och höja halten av radiolytiskt bildad H_2O_2 i karbonatlösning under bestrålning. I fall då O_2 finns löst i vattnet sänks halten av H_2O_2 genom en UO_2^{2+}-katalyserad reaktion mellan superoxidradikalen ($O_2^{\bullet-}$) och uranyl-peroxid-karbonat-komplexet. I syrefria lösningar kan UO_2^{2+} förhöja halten av H_2O_2 genom infångandet av reducerande radikaler (e_{aq}^- och $H^\bullet$). Kinetiken för karbonatdriven upplösning av oxiderad UO_2 omprövades då tidigare studier utförts under förhållanden där upplösning och oxidation sker simultant. I ett system där UO_2 oxiderades separat från själva upplösningen, observerades att upplösningen i sig är en komplex process med den observerade aktiveringsenergin (34,8 ± 3,2) kJ mol^{-1}. Reaktionsordningen med avseende på karbonat varierade mellan 0,5 och 1,5 inom temperaturintervallet (283 – 333) K och karbonatkoncentrationer mellan (1,3 – 15) mM. Beroendet av uranoxidens oxidationsgrad på upplösningshastighet visade sig ha tre distinkta faser: (1) en snabb upplösning av en mindre fraktion, (2) en långsammare upplösning med konstant hastighet (oberoende av oxiderad produkt), och (3) ett gradvis avtagande av upplöningshastighet då endast en liten fraktion av den oxiderade produkten kvarstår. Slutligen visade jämförelser

av Pd-dopade UO_2-tunnfilmer och UO_2-tunnfilmer utan Pd, i närvaro av H_2 att en potentiell H_2 effekt utan Pd-katalysator är ett flertal storleksordningar mindre effektiv i att hämma oxidationen av UO_2 jämfört med den Pd katalyserade reduktionen av oxiderad UO_2 med H_2. Palladium visade sig endast delvis reducera och skydda filmen mot korrosion, genom bildandet av en ren uran(V) intermediär (mellan $U(IV)O_2$ och $U(VI)O_3$). Denna Intermediär bedömdes mest troligt vara UO_2OH genom beräkningar av atomförhållandet U:O samt uranets oxidationstillstånd +5.

Nyckelord
Geologiskt djupförvar, Kärnbränsleavfall, Urandioxid, UO_2, Radiolys, Oxidativ Upplösning, Korrosion

Acknowledgments

I would first and foremost like to express my sincere gratitude to my main supervisor, Prof. Mats Jonsson, for his scientific guidance and support throughout this work. I am also deeply grateful to my co-supervisor Dr. Thomas Gouder and technician Frank Huber for trusting me with their sensitive equipment. The setup they have built is truly a masterpiece, and I can only hope that its future caretakers treat it as such.

To my colleagues—past and present—thank you for making my time at KTH both rewarding and enjoyable. Yi, Sawsan, and Junyi, thank you for making me feel at home from day one. Felicia, Fredrik, Aleksandar, Federica, Meng, Helena, Dunkan, and Zoë, thank you for making my final years at KTH memorable. I also want to express my deepest gratitude to my friends at the JRC, who welcomed me from the very first day and turned one of the most demanding periods of my life into something enjoyable.

To my family, some of whom I was born into, and others I have chosen along the way. Words cannot express what your support means to me. In a world of unstable nuclei, you are my ^{56}Fe. My island of stability to which I owe every success. My best friend and partner, Sofia, you believed in me, even at times when I struggled to believe in myself. Thank you for standing by my side.

Finally, I would like to express my gratitude to the Swedish Nuclear Fuel and Waste Management Company (SKB) for funding this project, and to the Joint Research Centre (JRC) and the European Commission for supporting my work in Karlsruhe.

List of papers

I. Olsson, D.; Li, J.; Jonsson, M., “Kinetic Effects of H_2O_2 Speciation on the Overall Peroxide Consumption at UO_2–Water Interfaces”. ACS Omega, 2022, 7(18), 15929-15935.

II. Olsson, D.; Aydogan, H.; Jonsson, M., “The influence of bicarbonate concentration and ionic strength on peroxide speciation and overall reactivity towards UO_2”. RSC Advances, 2024, 14, 16248-16254.

III. Olsson, D.; Jonsson, M., “The impact of uranyl ions on the radiation stability of hydrogen peroxide in aqueous bicarbonate solutions”. Manuscript.

IV. Olsson, D.; Emory, Z. C.; Jonsson, M., “On the mechanism and kinetics of dissolution of oxidized UO_2 in carbonate solutions – separating dissolution from oxidation”. Manuscript

V. Olsson, D.; Gouder, T.; Jonsson, M., “Exploring the possible inhibiting effects of H_2 on radiation-induced oxidation of UO_2 under UHV-conditions using XPS and UPS”. Manuscript.

VI. Olsson, D.; Gouder, T.; Jonsson, M., “Temperature dependent effects of Pd-catalyzed H2 reduction of uranium oxide explored under UHV-conditions with XPS and UPS”. Manuscript.

Contribution to papers

I. I participated in the planning and designing of the experiments. I performed the data analyzis and wrote the first version of the manuscript as well as the revision during peer review.

II. I did most of the planning and designing of the experiments. I performed parts of the experiments. I performed the data analyzis and wrote the first version of the manuscript as well as the revision during peer review.

III. I participated in the planning of the experiments. I performed all experiments and performed the data analyzis. I wrote the manuscript.

IV. I planned and designed the experiments. I performed most of the experiments. I performed the data analyzis. I wrote the text related to the experimetals, the results & discussion and the conclusions.

V. I participated in the planning of the experiments. I performed all experiments and performed the data analyzis. I wrote the manuscript.

VI. I participated in the planning of the experiments. I performed all experiments and performed the data analyzis. I wrote the manuscript.

List of abbreviations

HLW	High-level radioactive Waste
LET	Linear Energy Transfer, defined as the energy deposited in a medium per unit pathlength [J m^{-1}]
E_{bin}/BE	Binding Energy
XPS	Xray Photoelectron Spectroscopy
UPS	Ultraviolet Photoelectron Spectroscopy
TNS	Transition State Theory
R	Ideal gas constant
E_a	Activation energy
SA	Specific surface Area
K	Equilibrium constant
k	Reaction rate constant
r	Reaction rate
FWHM	Full Width at Half Maximum
ODE	Ordinary Differential Equation

CONTENTS

1. Introduction

In a modern society where rapid technological developments pose an increasing demand for energy, nuclear power is a valuable energy source. Like any energy source, nuclear energy poses some significant challenges. The handling and disposal of the high-level radioactive waste (HLW) produced during reactor operation is one of particular concern and has been a subject of debate for decades. As of today, HLW across the globe are piling up at reactor sites. After an initial period of heat decay through water cooling in deep pools, the still hot and highly radioactive fuel is transferred to either dry or wet intermediate storage. Dry storage usually involves placing the spent fuel in lead shielded dry casks [1, 2]. One example of wet intermediate storage is the Swedish Central Interim Storage Facility for Spent Nuclear Fuel, where eight meters of water shields against radiation. A more permanent solution to the waste problem will eventually become an inevitable part of any nuclear fuel cycle. In January 2022, a decision was made by the Swedish government to approve the construction of a deep geological repository in Forsmark, for permanent disposal of HLW. In January 2025, the groundbreaking ceremony for the constructions above ground took place.

The repository under construction will have the design of the KBS-3 system. The Nuclear Fuel Safety (KBS) project was initiated in the early 1980s as a response to the Swedish government passing the so-called “Stipulation Act” in 1977, which required nuclear reactor operators to demonstrate solutions for an absolute safe and permanent disposal of spent fuel [3]. The first comprehensive KBS-3 report was handed to the government in 1983, presenting a 3-level safety barrier system where HLW is sealed in a copper clad iron cannister, embedded in a buffer layer of bentonite clay and buried in the crystalline bed rock at the depth of around 500 m sub ground level [4]. In 1984, a review of the KBS-3 plan [5] by the American National Research Council was sent to the (now former) Minister of the Environment, Birgitta Dahl. The KBS-3 was formally accepted as a viable option for permanent waste disposal. In the late 1990s, SKB published SR-97, a report based on a three-year safety assessment research project regarding the long-term, post-closure safety of the KBS-3 repository [6]. The report underwent international peer review organized by the OECD Nuclear Energy Agency (NEA) [7]. The review concluded that KBS-3 provided a robust multi-layered safety barrier concept. They further concluded that SKB's strategy to achieve and demonstrate safety was well founded but not yet sufficiently well presented in SR-97. Extensive and systematic research led by SKB has since been conducted, assessing the long-term performance of the various components of the KBS-3 concept as well as the suitability of various potential repository sites based on geological factors such as climate, ground- and groundwater composition. Since SR 97, three safety assessments have been performed. The latest safety assessment of the spent nuclear fuel repository at Forsmark was published in 2022 [8].

Even if much knowledge has been gained over the years, some questions and issues remain. One such issue concerns the spent nuclear fuel dissolution in a repository environment. The vast timescales (100 000 y) involved in the safety assessment poses the need for extreme extrapolation from any available data, on which a model can be based. This in turn puts high demand on our level of understanding of the mechanisms involved in the processes related to spent nuclear fuel dissolution.

For the past two decades, numerous mechanistic and kinetic studies of the radiation induced corrosion of UO_2 (the main component of the uranium-based fuel used in Light Water Reactors) have been carried out, with the aim of providing a robust mechanistic description of spent nuclear fuel dissolution. This thesis builds on previous findings and addresses new aspects that had yet to be addressed prior to this work. The project focuses on three main parts:

(I) Aqueous phenomena – The impact of uranyl ions on the radiation stability of hydrogen peroxide and aqueous bicarbonate solutions.

(II) Heterogenous (solid-liquid interface) phenomena:

   a. The effect of uranyl ions on the reactivity of peroxide towards UO_2.
   b. A revised mechanistic and kinetic description of carbonate fassilitated uranyl dissolution.

(III) Solid phase phenomena – The role of ε-particles in redox-stability of UO_2.

A theoretical basis for each of these concepts will be provided in the chapters to follow. It should be emphasized that safe disposal and long-term geological confinement of spent nuclear fuel is a unique challenge. To fully understand the radiation induced geochemistry in a failed repository requires the integration of multiple scientific disciplines, including material science, physics, geology and chemistry. Ideally, each field comes with a unique viewpoint that enhances our overall understanding. If not treated with care, however, differences in viewpoints and scientific conventions can easily become sources of confusion and miscommunication. In this thesis, the mechanisms behind radiation induced UO_2-corrosion are investigated both through analysis of concentration changes in the liquid phase, and through changes in the chemical/electronic environment of surface near atoms in the solid material. My aim is to provide mechanistic descriptions that explain the observations made from both perspectives and thereby speak to the chemists, the physicists and the material scientists alike.

This work contributes to the scientific foundation required for the robust safety-assessments of permanent nuclear waste disposal. This is an essential component of achieving the UN Sustainable Development Goals related to health and well-being, clean energy, and responsible production (Goals 3, 7, 12).

1.1 Radiolysis - Radiation induced SNF corrosion

The nuclear fuel used in the commercial Light Water Reactors (LWR) such as the ones operating in Sweden consists of UO_2, with 95 percent ^{238}U and a 3 – 5 percent enrichment of the fissile isotope ^{235}U [9, 10]. At the time when ^{235}U is nearly depleted and criticality of nuclear fission can no longer be sustained, the ~ 95 percent ^{238}U remains (except for a small fraction that has formed heavier actinides through neutron capture). From the fission and subsequent decay of the remaining ~5 percent are elements across the periodic table, including some instable isotopes of fission products and long-lived heavier actinides (from neutron capture by ^{238}U), responsible for the high radioactivity and heat-generation of the HLW post reactor operation. As spent fuel ages, radioactivity becomes increasingly dominated by α-radiation [11].

In the event of multi-barrier failure, the surface of a still radioactive fuel would become wetted by groundwater intrusion. The low solubility of UO_2 prevents the bulk of the fuel matrix from dissolving in the absence of oxidants [12, 13]. Oxidation of UO_2 into hexavalent uranium oxide (UO_3) sharply enhances the solubility [14], with uranium released as uranyl ions UO_2^{2+}. The solubility is further raised by the presence of carbonate [15], which binds as ligands to form readily soluble $UO_2(CO_3)_3^{4-}$ [16-18]. At the planned depth of the repository the conditions are reducing [19, 20]. However, the irradiation of water at the fuel interface leads to water radiolysis (the splitting of water molecules through excitation and ionization), a process that forms highly reactive radicals and molecules, including both oxidants and reductants [11, 21, 22]:

$$H_2O \rightsquigarrow e^-_{aq}, H^\bullet, H_2, HO^\bullet, HO_2^\bullet, H_2O_2 \qquad (1.1)$$

The hydroxyl radical is one of the strongest known oxidants with a reduction potential of 1.77 – 1.98 V vs NHE [23, 24]. Although it is much more reactive towards UO_2, its ability to undergo reduction by one-electron transfer or H-abstraction with a wide range of ions and molecules, makes it extremely short lived under most conditions. Consequently, only a small fraction of the $HO^\bullet$ (formed in very close proximity to the fuel interface) could be expected to react with the fuel directly. H_2O_2 on the other hand is a relatively stable two-electron oxidant. The oxidation state of the oxygen atoms (O^{-I}) sits between that of O_2 (O^0) and H_2O (O^{-II}) and is thermodynamically unstable [25, 26]. In the absence of a catalyst, H_2O_2 degradation is slow, with typical half-lives on the scale of hours found in natural waters [27 - 29]. This in turn allows for the potential buildup of relatively high H_2O_2 concentrations in irradiated aqueous systems. Additionally, H_2O_2 readily oxidizes UO_2 and is considered the radiolytic oxidant with the main impact on the rate at which wet SNF is oxidized (when α-radiation dominates) [30].

2 The oxidation of uranium dioxide

This chapter covers the current mechanistic description of UO_2 oxidation. The corrosion of UO_2 has been studied extensively in the past, by selective addition of specific oxidants (i.e. O_2 or H_2O_2) [31-37], and in more complex systems where oxidation is promoted by the mixed molecular and radical products of α- or γ-radiolysis [37, 38-42]. Electrochemical studies have shown that the shape of the corrosion potential as a function of time is the same independent of the oxidant driving the corrosion as well as its concentration [43]. A common oxidation mechanism is therefore expected for the H_2O_2-, O_2- and plasma-induced oxidation applied for mechanistic- and kinetic studies in this work.

Stoichiometric $UO_{2.0}$ has a fluorite-type (CaF_2) structure where uranium forms an FCC lattice and oxygen atoms occupy tetrahedral sites. Each U is coordinated by 8 O and each O by 4 U. The first few monolayers of UO_2 are highly reactive and in the presence of O_2 they are oxidized already at negative potentials of -800 to -400 mV vs SHE [43]. Under more oxidizing conditions a layer of $UO_{2.33}$ (U_3O_7) forms, and its thickness increases with increasing potential. $UO_{2.33}$ is a distorted form of fluorite structure and sits on the edge of the FCC, with any additional incorporation of interstitial O inducing significant lattice changes [44]. The low solubility of UO_2 is maintained up to $UO_{2.33}$, after which dissolution rates have been observed to increase sharply [37, 43]. The structures of the more stable phases of uranium oxide UO_2 [44, 45], $UO_{2.25}$ (U_4O_9) [46], $UO_{2.67}$ (U_3O_8) [47, 48] and UO_3 [49-51] have been determined through neutron diffraction. $UO_{2.33}$ remains largely unknown but later studies have described the phase as a derivative of the fluorite structure with excess oxygen in cuboctahedral clusters [52, 53]. The mechanism of oxidation as a function of increasing potential has been described as follows [43]:

$$UO_2 \rightarrow UO_{2+x}(\text{monolayer}) \rightarrow UO_{2+x} \rightarrow UO_{2.33} \rightarrow UO_{2.5} \rightarrow UO_{2.67} \rightarrow UO_3 \qquad (2.1)$$

The oxidation of UO_2 induced by H_2O_2 has often been described in terms of a mechanism involving homolytic cleavage of the peroxide (O-O) bond, with the formation of a radical intermediate referred to as surface bound hydroxyl radicals [34]. The mechanism is provided as follows:

$$H_2O_2 + 2\,UO_2 \rightarrow 2HO^{\bullet}_{ads} \quad (2.2)$$

$$HO^{\bullet}_{ads} \rightarrow UO_2^{+} + OH^{-} \quad (2.3)$$

$$HO^{\bullet}_{ads} + H_2O_2 \rightarrow HO_2^{\bullet} + H_2O + UO_2 \quad (2.4)$$

$$HO_2^{\bullet} + HO_2^{\bullet} \rightarrow H_2O_2 \quad (2.5)$$

The implication of the mechanism is that the surface bound hydroxyl radical intermediate (surface bound $HO_{ads}^{\bullet}$) are consumed in one of two ways; (I) by oxidation of UO_2 into UO_2^{+} which induces oxidative dissolution (via an unknown second oxidation step forming UO_2^{2+} which is assumed to be fast) or (II) by the scavenging by H_2O_2 which leads to the formation of O_2 and H_2O. The relative contribution of these pathways is studied in terms of H_2O_2' s oxidative efficiency (determined by the ratio dissolved UO_2^{2+} : consumed H_2O_2). This efficiency is referred to as the dissolution yield.

New insights related to the mechanism of UO_2 oxidation were recently reported by Perrot et al., where formation of studtite was studied in α- and β-irradiated, ^{18}O-labeled water [54]. Studtite is a secondary phase consisting of peroxo-coordinated UO_2^{2+} which readily forms in the presence of H_2O_2 and absence of other strong complexing ligands such as CO_3^{2-}. The authors reported UO_2^{2+} with equatorial oxygen atoms consisting of both ^{18}O and ^{16}O which shows that oxidation may occur both through incorporation of ^{18}O (likely via $H^{18}O^{\bullet}$) and through electron transfer without oxygen incorporation ($^{16}O{=}U{=}^{16}O$ + $2e^-$). Meanwhile, the clean ^{18}O-signal observed for the O_2^{2-} ligand (coordinated peroxide) in α-irradiated solutions and direct exposure to ^{18}O-labeled H_2O_2 showed that studtite formation occurs through precipitation of intact O_2^{2-} from aqueous H_2O_2.

Studies of UO_2 oxidation with XPS have frequently reported significant buildup of pentavalent U(V) in the solid [55, 56]. This indicates a meta stable intermediate, the mechanistic role of which has yet to be understood. Disproportionation of two U(V) into U(VI) and U(IV) [57] could possibly drive the formation of surface-near U(VI) and prevent long-term stability of U(V)-rich phases such as $UO_{2.33}$. This would explain the observation of a gradual disappearance of U(V) in oxidized UO_2 pellets kept in bicarbonate solutions [56].

The rate of corrosion of spent nuclear fuel is set in part by properties of the fuel itself. Short-term (after reactor operation), γ-radiation will account for a significant fraction of the total energy deposition. Over geological timescales however, α-radiation will persist and dominate in the long-term. Although the same oxidants are formed, the yields (G-values) are very different, with γ-radiation favoring radical yields and α-radiation largely favoring molecular products through enhanced radical-radical recombination due to more local energy deposition events [58]. Not only the properties of the fuel, but the nature of the irradiated environment has been found to greatly impact the rate of corrosion. Jégou et al. [59] found that the rate of fuel alteration dropped by an order of magnitude with 4 % H_2 + Ar atmosphere (compared with air), along with three orders of magnitude drop of the H_2O_2 steady state concentration. The role of H_2 in countering UO_2 oxidation has been found to be multifold. H_2 has been found to suppress the H_2O_2 yield under low Linear Energy Transfer (LET) rate - conditions (i.e. γ-radiation). Pastina and LaVerne found this effect to be negligible under high-LET (α-radiation) [57], suggesting that much higher H_2 pressures are required to influence the local chemistry (in radiolytic spurs) induced by α-radiation. These results have since been disputed by Trummer and Jonsson (2010) [60], reporting that H_2 can suppress radiolytically formed H_2O_2 with a magnitude that depends on the α-dose rate as well as on [HCO_3^-].

A second effect of H_2 is the well-known interaction between H_2 and metallic inclusions, the most common of which are Mo, Tc, Ru, Pd, Rh [61]. The metallic inclusions, sometimes referred to as ε-particles, have a size range from a few nanometers up to several micrometers due to agglomeration/aggregation of smaller particles into larger clusters [62, 63]. Metallic inclusions (particularly the inclusion of palladium) have been found to catalyze H_2 induced reduction of uranium oxide, suppressing oxidative dissolution [61, 64-68]. The catalytic effect of palladium can most likely be attributed to its remarkable ability to absorb and diffuse H_2 (Through formation of Pd-H) which was discovered already in 1866 by the chemist T. Graham [69]. Metallic inclusion of Pd has also been observed to catalyze the H_2O_2- and O_2 – induced oxidation through near diffusion-controlled kinetics [65, 66, 70]. The net effect has been found to be reducing, with the inclusion of 3 wt.-% Pd shown to inhibit dissolution through reaction with radiolytically formed H_2, whilst significantly less (0.1 wt.-%) was found to be sufficient in preventing dissolution under 1 bar H_2 atmosphere [66]. More recently, Maier and Jonsson [67] found that powder suspensions of Pd effectively catalyze both reduction of aqueous UO_2^{2+} (resulting in precipitation) and H_2O_2. In a later work, Hansson and Jonsson [68] assessed the relative contribution of three H_2 effects-; (1) effect on radiolytic oxidant production, (2) reduction of U(VI) and (3) reaction with surface bound hydroxyl radicals, - in inhibiting oxidative dissolution of UO_2. Through numerical simulations, the authors found the first effect to be of minor importance, whilst the second could fully account for the observed inhibition of oxidative dissolution of Pd doped UO_2 in the presence of H_2. The third contribution was suggested to be responsible for the inhibiting effect of H_2 in the absence of noble metal inclusions.

3 XPS and UPS as Probes of Oxidation state in Uranium Oxides.

As SNF corrosion is enabled by the oxidation of UO_2 into more soluble phases of higher oxide content, the redox state of uranium oxides (UO_x) is an important metric by which corrosion mechanisms and rates can be analyzed. One of the great benefits of photoelectron spectroscopy methods is their high surface sensitivity (shallow probing depth). This allows for characterization of a very thin surface layer. It is within this layer that uranium atoms are in immediate contact with the surrounding environment, and consequently it is the reactivity/inertness of this layer towards the surrounding environment that largely determines the long-term integrity of the fuel. This chapter will focus on the basic working principles of X-ray Photoelectron Spectroscopy (XPS) and Ultraviolet Photoelectron Spectroscopy (UPS) and their application in characterization of uranium oxides.

3.1 Binding Energy and peak/signal intensity

The electronic configuration of an atom is composed of a discrete set of quantized energy levels. In molecular orbital theory, these levels are described as spatial probability distributions (orbitals) representing regions in which the electron has the highest probability of being found. According to the Pauli exclusion principle, each atomic orbital can accommodate a maximum of two electrons with opposite spins.

As free atoms approach one another to form a solid, the outer atomic orbitals overlap such that the electrons of one atom experience the potential of neighboring nuclei. These electrostatic interactions give rise to energy band formation and chemical shifts as electrons in a given type of orbital become slightly non-degenerate due to differences in their local chemical environment [71].

In photoelectron spectroscopy, these differences are detected by measuring the energy required to remove (ionize) an electron from a specific atomic or molecular (hybridized) orbital. This energy is referred to as the binding energy (BE/E_{bin}). When monochromatic light of a sufficiently high photon energy (hν) hits atoms of a solid material, electrons of $E_{bin} \leq h\nu$ are ejected from the material. The kinetic energy (E_{kin}) of the emitted electrons is measured by an electron energy analyzer and is related to the binding energy by the photoelectric equation [71, 72]:

$$E_{bin} = h\upsilon - E_{kin} - \phi \qquad (3.1)$$

where Φ is the work function of the spectrometer, determined experimentally using a calibration standard. Due to its chemical inertness, Au ($4f_{7/2}$ at 84.0 eV or fermi edge at 0 eV) is often used [73, 74].

The detected photoelectron signal appears as a peak in a spectrum where intensity (typically counts) is plotted as a function of binding energy. The intensity and sharpness of each peak depend not only on the surface concentration of the corresponding element or orbital, but also on factors such as the photoionization cross section, inelastic mean free path (IMFP) of the emitted electrons, and experimental geometry. Instrumental specific transmission factors, angular distribution of photoemission and spectral redistribution into separate features referred to as “satellite peaks” or “shake-ups” further influences the observed intensities. A comprehensive theoretical treatment of these effects is beyond the scope of this thesis; the reader is referred to the literature for more in depths descriptions [71, 72, 75].

For quantitative purposes the photoemission intensity can be described in terms of a few key parameters and a "catch-all" parameter P [76]:

$$I_{PE} = I_{hv} * n * \sigma * [U] * P \qquad (3.2)$$

where I_{hv} is the intensity of the incident light, n the number of electrons in the given state, σ the photoionization cross section and [U] the concentration/abundance of uranium within the probing depth of XPS (~1 – 10nm [77, 78]). Notably, σ describes the probability for a core electron to be emitted by the excitation and depends on hν. In this work, reference values for σ as tabulated in *Handbook of X-ray photoelectron spectroscopy* were used for quantifying relative atom concentrations.

3.2 Spectral features and interpretation of XPS data

The coupling of quantum angular momentum (l) and quantum spin (s = 1/2) in core electrons gives the total angular momentum quantum number j = l ± s. For the f electrons (l = 3) in uranium, a split signal is obtained (j = 7/2 and j = 5/2). The relative intensity of the split peaks is set by the statistical degeneracy:

$$\text{degeneracy} = 2j + 1 \qquad (3.3)$$

Thus, the ratio of U4f 7/2 : U4f 5/2 becomes 8 : 6 [71, 72, 73]. Additional peak splitting is often observed in the U4f region (370 – 405 eV). When core electrons are ejected, valence electrons such as the U5f electrons can respond by undergoing simultaneous excitation. If excitation occurs, the measured kinetic energy of the emitted core electron will be lower than the corresponding emission in absence of excitation, and a satellite peak appears, shifted towards higher binding energies relative to the main line. This perturbation is known as the shake-up process [71]. For stoichiometric $UO_{2.0}$ the U4f satellite of U^{4+} is prominent. It appears diminished and further shifted in U^{5+} and weaker still and further shifted in U^{6+} [55, 79]. This occurs as the filled f orbital of U^{4+} ($5f^2$ configuration) renders the probability of simultaneous excitation higher than with fewer or absent 5f electrons in U^{5+} ($5f^1$) and U^{6+} ($5f^0$). Conveniently, these differences make the shape and energy shift of the U4f shake-up satellite a useful tool when estimating the oxidation state of the uranium oxide surfaces.

4 Reaction Kinetics (quantifying the evolution of chemical systems)

Although a deep mechanistic understanding of a process is valuable, its mathematical description (model) is what enables foresight and predictions related to the evolution of the process over time. Moreover, quantification can also yield information about the underlying mechanism itself. This chapter will provide the fundamental knowledge required to understand the kinetic descriptions used throughout this thesis. Some fundamental knowledge within chemistry and thermodynamics is assumed.

4.1 Homogenous (solution) kinetics

Reactions in homogenous (aqueous) mixtures are among the most studied. The rate of many such reactions can be expressed by empirical rate equations [80]. Consider the general reaction

$$\alpha A + \beta B \rightarrow C \qquad (4.1)$$

The rate of reaction 4.1 is given by the empirical rate expression

$$r = k[A]^{\alpha}[B]^{\beta} \qquad (4.2)$$

The rate constant k and the exponents (reaction orders) α and β are time and concentration independent quantities that are generally determined experimentally, although quantum mechanical calculation methods have in recent years been shown to yield predicted rate constants of high accuracy [81]. Despite the simplicity of Eqn 4.2, simulating the evolution of [A] and [B] with time is not always straightforward. In many chemical systems of practical interest, chemical species are involved in several reactions occurring in parallel. This is certainly true for the chemical stage of water radiolysis, with the most complete description including 72 reactions for pure water alone [58]. For such a set, the kinetic descriptions of all reactions comprise a system of ordinary differential equations (each described by Eqn 4.2), ODE. The system of equations can be solved numerically. Computational cost often increases sharply with the number of reactions (and reactants), and simplified radiolysis models with < 20 reactions have been shown to yield predictions with accuracy comparable to the more extensive ones [82].

4.2 Heterogenous kinetics (reactions at the solid-liquid interface)

Oxidation of UO_2 and subsequent dissolution of UO_2^{2+} are surface-controlled processes, in which reactive species in solution must first adsorb onto the solid surface before reaction can occur. A primary distinction from homogenous reactions is the geometry of the reactive interface. As the reactive sites sit on the UO_2 surface, the overall rate of the reaction naturally scales with the UO_2 specific surface area (SA) [83, 84]. Another key difference is that reaction orders of bulk species reacting with the surface (α and β of Eqn 4.2) are typically concentration dependent. This is because the surface reaction at some point is unable to keep up with the adsorption, at which point the surface becomes saturated [85, 86]. The correlation between the reaction rate and surface saturation is described by introducing an equilibrium isotherm to the rate expression. The Langmuir-Hinshelwood (LH) model is widely used for such kinetics [80, 87, 88]. The model is easily extended to include several species. It assumes a monolayer with identical sites and no lateral interactions (adsorption equilibrium independent on surface coverage).

$$\theta_i = \frac{K_i C_i}{1+\sum_j K_j C_j} \qquad (4.3)$$

with the rate for two species, each with a 1st order reaction dependence expressed as

$$r = k\theta_A\theta_B = k\frac{K_A C_A}{1+\sum_j K_j C_j}\frac{K_B C_B}{1+\sum_j K_j C_j} \qquad (4.4)$$

In the case of UO_2 oxidation, where an oxidant in solution adsorbs to react with the surface itself Eqn 4.4 is reduced to

$$r = \frac{kKC_{ox}}{1+KC_{ox}} \qquad (4.5)$$

Saturation is reached when $KC_{ox} >> 1$, in which case r becomes independent on C_{ox} (0th order) and can be approximated as ~ k. In the other extreme, where the surface is far from saturation ($KC_{ox} << 1$), r displays 1st order dependence on C_{ox} with r ~ kKC_{ox}.

4.3 The Influence of Temperature on the Equilibrium Constant (K) and the Rate Constant (k): Where Kinetics and Thermodynamics meet"

Based on the second law of thermodynamics and Gibbs' formulation of free energy, Jacobus Henricus van 't Hoff derived what is now known as the van 't

Hoff equation [89], describing the relationship between the equilibrium constant of a (reversible) chemical process and temperature.

$$\frac{d\ln K}{dT} = \frac{\Delta H^{o}}{RT^{2}} \qquad (4.6)$$

Shortly after, Svante Arrhenius empirically derived the temperature dependence for the rate constant of a chemical process, now known as the Arrhenius' equation [90].

$$k = Ae^{-\frac{E_a}{RT}} \qquad (4.7)$$

E_a is referred to as the activation energy of a reaction. During the later development of transition state theory (TST), a similar relation known as the Eyring equation [91] was derived on a statistical mechanical basis

$$k = \frac{\kappa k_B T}{h} e^{-\frac{\Delta G^{\ddagger}}{RT}} \qquad (4.8)$$

where k is the rate constant of the reaction, κ is the called the transmission coefficient (often expressed as unity), k_B is the Boltzmann constant, h the Planck constant and $G^{\ddagger}$ the Gibbs energy of activation. Using the relationship between Gibbs' free energy, enthalpy ΔH and entropy ΔS, Eqn 4.8 can be written on the form:

$$\ln\frac{k}{T} = -\frac{\Delta H^{\ddagger}}{RT} + \ln\frac{\kappa k_B}{h} + \frac{\Delta S^{\ddagger}}{R} \qquad (4.9)$$

TST provides the bridge between kinetics and thermodynamics by linking the rate constant of a chemical process to the thermodynamic properties of the activated complex (TS). The rate constant reflects the probability that reacting species acquire sufficient energy for a chemical change to occur. This probability is governed by $G^{\ddagger}$.

5 Dissolution of oxidized $UO_{2.x}$

This section summarizes reported observations related to the mechanism of $UO_{2.x}$ dissolution. Notably, far less has been reported about this process compared to the oxidation. This is because previous works have studied uranium release in systems where dissolution and oxidation occur jointly as parallel processes. Any knowledge related to an individual process (oxidation or dissolution) extrapolated from such systems, therefore heavily rests upon an assumption that a parameter under investigation affects one process and not the other. The results later presented in this thesis demonstrate that the process of dissolution is poorly understood and possibly as complex as the mechanism behind oxidation.

In the presence of complexing ligands, uranium release from oxidized UO_x ($x > 2.33$) occurs in the form of uranyl ions (UO_2^{2+}). Extensive work by Schortmann and DeSesa was published in 1958 [83], where the dependency of several critical parameters on the uranium release rate in carbonate media was determined, including active surface area (SA), oxygen partial pressure, temperature and carbonate/bicarbonate concentration. Based on their experimental findings, the authors derived a rate equation for the overall process of oxidative dissolution:

$$-\frac{dC}{dt} = \frac{k\frac{SA}{V}\,p_{O_2}^{1/2}C_L^2 e^{-\frac{E_a}{RT}}}{K_2+C_L^2} \qquad (5.1)$$

where

C = concentration of solid uranium dioxide
k = the rate constant for the oxidation process

t = time

SA/V = the solid surface area to liquid volume ratio

p_{O_2} = the oxygen partial pressure

C_L = the ligand (HCO_3^-/CO_3^{2-}) concentration

E_a = the activation energy (56.1 kJ per mole U)

R = The gas constant

T = The absolute temperature

K_2 = constant at constant pressure

The derived rate expression (Eqn 5.1) suggests that a single activation energy can be used to describe the combined process of oxidative dissolution. Additionally, it states that the carbonate concentration dependence on the overall rate -dC/dt can vary within the boundaries of two extreme cases; (I) 2nd order dependence ($R \propto C_L^2$), when $C_L^2 << K_2$ such that the denominator of Eqn 5.1 can be approximated as K_2 and (II) 0th order when $C_L^2 >> K_2$, such that the concentration cancels out from Eqn 5.1 and a concentration independent rate expression is obtained. To the best of my knowledge, this is the first and only reported account of a 2nd order carbonate dependence on UO_2^{2+} dissolution. Later works have consistently reported carbonate dependencies ≤ 1 [92-94].

Schortmann and DeSesa further laid out a mechanistic interpretation of the joint oxidation-dissolution process. A competitive interplay between oxidation and dissolution was described in terms of a surface equilibrium where oxidation is dependent on the surface area of UO_2, whilst carbonate facilitated dissolution is dependent on the surface area of the oxidized product (referred to as UO_3). The authors further proposed that the activated complex of the dissolution process is $UO_2(CO_3)^{2-}$ and involves the attachment of both carbonates. Although numerous experiments support limited solubility for product of the first carbonate attachment ($UO_2CO_{3\,(s)}$) [95-98] and dissolution occurs after the inclusion of the second carbonate, the typical 1st order carbonate dependence observed in later studies indicates that only one carbonate is involved in the rate determining step. This would mean that one of the carbonate attachments (the first or the second) is the slowest step in the overall dissolution mechanism while the other must occur rapidly.

A second mechanistic description of the oxidative dissolution of UO_2 was proposed by De Pablo and co-authors [92]. The proposed mechanism consisted of the three steps shown below.

Step 1 (oxidation)

$$UO_2 + \frac{1}{2}O_2 \underset{k_{-1}}{\overset{k_1}{\rightleftarrows}} UO_3 \qquad (5.2)$$

Step 2 (surface coordination of UO_3 by HCO_3^-)

$$UO_3 + HCO_3^- \overset{k_2}{\rightarrow} UO_3 - HCO_3^- \qquad (5.3)$$

Step 3 (detachment)

$$UO_3 - HCO_3^- \overset{k_3}{\rightarrow} \text{"}U(VI)_{(aq)}\text{"} \qquad (5.4)$$

The derived rate expression for the proposed mechanism was provided as:

$$r = \frac{k_1 k_2 \{UO_x\}_{tot}[O_2][HCO_3^-]}{k_{-1} + k_2[HCO_3^-] + k_1[O_2]} \qquad (5.5)$$

This rate expression suggests a reaction order ≤ 1 with respect to $[O_2]$ on the rate of oxidation unlike the strict $\sqrt{[O_2]}$ dependence derived by Schormann and DeSesa. Moreover, Eqn 5.5 dictates that the carbonate concentration dependence may vary between 0^{th} and 1^{st} order but never proceed to reach the 2^{nd} order dependence reported by Schortmann and DeSesa.

Aside from the rate models, some additional findings are worth mentioning. A study on the effect of temperature and bicarbonate concentration on the kinetics of the oxidative dissolution was published by de Pablo and co-authors. There, a change in carbonate concentration dependence on the dissolution rate with temperature was reported, with a square root dependence observed at room temperature (298.15 K), and 1^{st} order dependence at two higher temperatures (313.15 K and 333.15 K). Estimated activation energies for the first 2 of the 3 proposed steps (see kinetic model by de Pablo et al. above) [92] was reported by fitting k_1, k_{-1} and k_2 to Eqn 5.5. The value E_{a2} was reported as (35.7 ± 0.2) kJ mol^{-1}. This remains (to the best of my knowledge) the only reported estimate of the temperature dependence on the pure dissolution rate, up to date.

6 Experimental

This section covers experimental set-up and procedures as well as the materials, chemicals and instrumentations used. The information will be presented in separate sections for each of the three parts of the project presented on page 4.

6.1 Chemicals and materials

All chemicals used were reagent grade or higher. Solutions were prepared using deionized, 18.2 MΩ cm Merck Milli-Q water.

6.1.1 Paper I, II, III and VI

The UO_2 powder (supplied by Westinghouse Electric AB) was characterized as $UO_{2.34}$, with a BET surface area of 5.4 ± 0.2 $m^2\ g^{-1}$ prior to this work [33]. Stock solutions of UO_2^{2+} were prepared from uranyl nitrate hexa-hydrate ($UO_2(NO_3)_2 \times 6H_2O$, Merck). An exception was made in paper III where a stock solution of $UO_2(CO_3)_3^{4-}$ was prepared through oxidative dissolution of the UO_2 powder in O_2 saturated, 10 mM $NaHCO_3$ solution. This was to avoid the interference of NO_3^- which is reactive towards radiolytic reductants (e_{aq}^- and $H^\bullet$) [99-104]. Stock solutions of H_2O_2 were prepared from (stabilizer free) perhydrol (30 w/w% H_2O_2, Sigma-Aldrich). Carbonate solutions were prepared from $NaHCO_3$ (Merch).

6.2 Analysis and quantification

6.2.1 Spectrophotometric detection and quantification (Paper I, II, III and VI)

Detection and quantification of aqueous UO_2^{2+} was performed using the Arsenazo III method [105-107]. Direct detection in UV-vis is enabled by the formation of U(VI)-(1,8-dihydroxynaphthalene-3,6-disulphonic acid-2,7-bis[(azo-2)-phenylarsonic acid]) complex which strongly absorbs at 653 nm in acidic solution (pH 1 – 4 for optimal detection). The calibration for the Arsenazo III detection of $UO_2^{2+}$was prepared from standard uranyl nitrate solutions, whose concentrations were calculated from the known mass of the dissolved salt.

Hydrogen peroxide concentrations were determined by the triiodide spectrophotometric method introduced by Ghormley, 1952 [108]. Aliquots from the filtered sample solution were mixed with excess I^- (potassium iodide from

Sigma-Aldrich) and a 1:1 acetic acid / acetate buffer containing ammonium molybdate catalyst. The reaction leads to rapid and full conversion of H_2O_2 into I_3^-, the absorbance of which was measured at 360 nm where a second maximum occurs without interference from UO_2^{2+}. The calibration was performed by determination of the H_2O_2 concentration through permanganate titration. The obtained extinction coefficients for the method $\varepsilon_{360nm} = 2.41 \times 10^4$ M^{-1} cm^{-1} and $\varepsilon_{350nm} = 2.59 \times 10^4$ M^{-1} cm^{-1} is within the range of reported calibrations for the method $(2.32 – 2.76) \times 10^4$ M^{-1} cm^{-1} [109-111].

The (Tris(hydroxymethyl)-aminomethane) (tris) scavenging method was used for detection and quantification of the of surface-bound HO• upon decomposition of H_2O_2 on ZrO_2. Tris, upon reacting with H-abstracting radicals, forms formaldehyde (HCHO) as one of the stable products. The formaldehyde was detected through a modified version of the Hantzsch reaction. The procedure was carried out as described by Li et al [112]. The absorbance of the pyridyl derivative (product of the Hantzsch reaction) was measured at 368 nm.

6.2.2 Solid surface analysis with XPS and UPS

Oxidation/reduction of uranium oxide thin films was probed through changes in the core level- and valence band spectra in X-ray photoelectron spectroscopy (XPS) and the valence band in Ultraviolet photoelectron spectroscopy (UPS). The Specs Phoibos 150 hemispherical analyzer was used for the XPS analysis. Excitation was induced by Al-Kα (1486.6 eV) radiation from an XRC-1000 µ-focus source, equipped with a monochromator operating at 120 W. The spectrometer was calibrated using the peaks Au-4f7/2 (83.9 eV) and Cu-2P3/2 (932.7 eV) of metallic Au and Cu. UPS measurements were taken using He II (40.81 eV) UV excitation, produced by a high intensity windowless discharge lamp. All XPS and UPS spectra were obtained at room temperature.

The average charge of the uranium atom (U^{x+}) in undoped uranium oxide films was calculated by comparing the relative area of the U5f to U4f signal as proposed by el Jamal et al. [76]. The U4f signal works as an internal intensity reference with no change in the number of 4f electrons upon oxidation whilst the intensity of the U5f is directly proportional to the number of electrons in the 5f valence state (n_{5f}). n_{5f} decreases during oxidation with $5f^2$ for U(IV), $5f^1$ for U(V) and $5f^0$ for U(VI). Additionally, U^{x+} was calculated through deconvolution of the U4f 7/2 peak into the three component U(IV), U(V) and U(VI). U4f 7/2 peak centers were found at 380.3, 380.9 and 381.6, with FWHM = 1.57, 1.43 and 1.21 for pure U(IV), U(V) and U(VI) respectively. Fitting of the U4f 7/2 peak was done using Voight functions with Shirley background correction. Some variation of both peak centers and peak widths was allowed during optimization (internal ref ± 0.2 eV).

The calculated oxidation states were qualitatively verified by comparisons of the characteristic energy separation of the U4f signal and its shakeup satellite which has been uniquely determined and reported for pure U(IV), U(V) and U(VI) [79].

Another method for quantitative analysis of the oxidation state of the uranium oxide film is the analysis of the change in O1s to U4f signal ratio proposed by el Jamal et al. [76]. Although this method was applied in the same way in this work, our interpretation of the results differs. My argument for this is that this ratio reflects the O atom concentration relative to the U atom concentration (UO_y) and not the charge of the uranium atoms U^{x+} as lattice oxygen cannot be assumed to strictly exist in the form of O^{2-}.

6.2.3 Rate model for radiolysis simulations (Paper III)

Escape yields for primary production of radiolysis products used in the radiolysis model (R3 – R6) are the values reported by Pastina & LaVerne [58]. Fast equilibria for the carbonate and superoxide speciation are assumed such that the calculated concentrations of H_2CO_3, HCO_3^- and CO_3^{2-} as well as $HO_2^\bullet$ and $O_2^{\bullet-}$ reflect the concentrations at thermodynamic equilibrium given the total concentration of acid/base pairs at the given pH (specified in the simulation). A pH of 8.4 (as measured for a newly prepared 10 mM $NaHCO_3$ solution) in the calculations presented under section 7.2.1.

The pH dependent fractions of HCO_3^- and CO_3^{2-} were calculated as [113]:

$$\mathrm{f_{HCO_3^-}} = \frac{10^{-\mathrm{pKa_1}}10^{-\mathrm{pH}}}{10^{-2\mathrm{pH}}+10^{-\mathrm{pKa_1}}10^{-\mathrm{pH}}+10^{-(\mathrm{pKa_1}+\mathrm{pKa_2})}} \quad \text{and} \quad f_{CO_3^{2-}} = 1 - \mathrm{f_{HCO_3^-}} \qquad (6.1)$$

The pH dependent apparent rate constant k_{app} for superoxide disproportionation (R7 in Table 1) was calculated using the pH dependence reported by Bielski and Allen [114], which the authors demonstrated to accurately describe the observed rate over the full pH range:

$$\mathrm{k_{R7}} = \frac{7.61*10^5+8.86*10^7*10^{-pKa}*10^9}{(1+10^{-pKa}*10^{pH})^2} \qquad (6.2)$$

The pKa used was 4.8 based on reported values within the range 4.7 – 4.9 for $HO_2^\bullet$/ $O_2^{\bullet-}$ [114-116].

Concentration profiles as functions of time were calculated numerically using MATLAB's built-in solver for stiff ODEs (ode15s), using the relative tolerance 10^{-9} and absolute tolerance 10^{-12}, which define the allowable local integration error and ensure high numerical accuracy of the solution.

Table 6.1. Radiolysis model

Reaction nr	Reaction	Rate specific quantities (k/pk$_a$/G-values)	Comment	Ref.
R1	$H_2CO_3 \overset{K_{a1}}{\leftrightarrow} HCO_3^- \overset{K_{a2}}{\leftrightarrow} CO_3^{2-}$	$pKa_1 = 6.35$, $pKa_2 = 10.33$	Assumed fast equilibrium.	[117]
R2	$HO_2^\bullet \overset{K_a}{\leftrightarrow} O_2^{\bullet-}$	$pKa = 4.8$	Assumed fast equilibrium.	[114-116]
R3	$G(H_2O_2)$	$G(H_2O_2) = 7.3 \times 10^{-8}$ mol J^{-1}	Rate $= \dot{D} * G(H_2O_2)$ [M s^{-1}]	[58]
R4	$G(HO_2^\bullet)$	$G(HO_2^\bullet) = 2.1 \times 10^{-9}$ mol J^{-1}	Rate $= \dot{D} * G(HO_2^\bullet)$ [M s^{-1}]	
R5	$G(e_{aq}^-)$	$G(e_{aq}^-) = 2.7 \times 10^{-7}$ mol J^{-1}	Rate $= \dot{D} * G(e_{aq}^-)$ [M s^{-1}]	
R6	$G(H^\cdot)$	$G(H^\cdot) = 6.8 \times 10^{-8}$ mol J^{-1}	Rate $= \dot{D} * G(H^\bullet)$ [M s^{-1}]	
R7	$2\ O_2^{\bullet-}(+2H^+) \rightarrow H_2O_2$	Eqn 6.2	pH dependent k_{app}	[114]
R8	$HO^\bullet$ + carbonate $\rightarrow CO_3^\bullet\ (+OH^-/H_2O)$	$k' = 8.5 \times 10^6 * f_{HCO_3^-} + 3.9 \times 10^8 * f_{CO_3^{2-}}$	pH dependent k_{app}	[118]
R9	$CO_3^{\bullet-} + H_2O_2 \rightarrow O_2^{\bullet-}$ + carbonate	$4 \times 10^5\ M^{-1}s^{-1}$		[119]
R10	$CO_3^{\bullet-} + CO_3^{\bullet-}(+2H^+) \rightarrow H_2O_2 + 2CO_2$	$1.4 \times 10^7\ M^{-1}s^{-1}$	Assumed instant decay of $C_2O_6^{2-}$ into O_2^{2-} (and CO_2)	[118]

R11	$O_2^{\bullet-} + CO_3^{\bullet} \rightarrow \text{carbonate} + O_2$	$6.5 \times 10^{8}\ M^{-1}s^{-1}$		[120]
R12	$HO^{\bullet} + H_2O_2 \rightarrow O_2^{\bullet}(+H^{+} + H_2O)$	$2.7 \times 10^{7}\ M^{-1}s^{-1}$		[121, 122]
R13	$2HO^{\bullet} \rightarrow H_2O_2$	$3.6 \times 10^{9}\ M^{-1}s^{-1}$		
R14	$e_{aq}^{-} + H_2O_2 \rightarrow HO^{\bullet}(+OH^{-})$	$1.1 \times 10^{10}\ M^{-1}s^{-1}$		[58]
R15	$e_{aq}^{-} + O_2^{\bullet-}(+2H^{+}) \rightarrow H_2O_2$	$1.3 \times 10^{10}\ M^{-1}s^{-1}$		
R16	$e_{aq}^{-} + HO^{\bullet} \rightarrow (OH^{-})$	$3 \times 10^{10}\ M^{-1}s^{-1}$		
R17	$e_{aq}^{-} + CO_3^{\bullet} \rightarrow \text{carbonate}$	$2 \times 10^{10}\ M^{-1}s^{-1}$	Assumed as no constant has been reported.	-
R18	$e_{aq}^{-} + O_2 \rightarrow O_2^{\bullet-}$	$2 \times 10^{10}\ M^{-1}s^{-1}$		[58, 123, 124]
R19	$e_{aq}^{-} + N_2O\ (+H^{+}) \rightarrow HO^{\bullet}(+N_2)$	$9 \times 10^{9}\ M^{-1}s^{-1}$		[123, 125]
R20	$H^{\bullet} + H_2O_2 \rightarrow HO^{\bullet}(+H_2O)$	$9 \times 10^{7}\ M^{-1}s^{-1}$		[126]
R22	$H^{\bullet} + O_2 \rightarrow O_2^{\bullet-}(+H^{+})$	$1.4 \times 10^{10}\ M^{-1}s^{-1}$		[123]
R23	$H^{\bullet} + N_2O \rightarrow HO^{\bullet}(+N_2)$	$2.1 \times 10^{6}\ M^{-1}s^{-1}$		[127]
R24	$O_2^{\bullet-} + H_2O_2 \rightarrow HO^{\bullet}(+OH^{-} + O_2)$	$0.13\ M^{-1}s^{-1}$		[128]

6.3 Experimental procedures

6.3.1 Paper I and II

The UO_2 powder was washed consecutively in 10 mM $NaHCO_3$ solutions before exposure to remove pre-oxidized U(VI). Five consecutive replacements of the washing solution were carried out, throughout which magnetic stirring was used. After full sedimentation (as indicated by a clear solution) the liquid was removed with a syringe. Before the first exposure, successful removal of pre oxidized U(VI) was confirmed through analysis of the last washing solution where [UO_2^{2+}] was found to be under the detection limit 1×10^{-7} M.

Solutions of uranyl nitrate, sodium bicarbonate and sodium perchlorate (if used) were first mixed and added to the powder. Hydrogen peroxide was added last, marking the start of the exposure. N_2-purging was kept constant throughout the exposure.

6.3.2 Paper III

The stock solution of $UO2(CO3)3^{4-}$ was prepared by oxidative dissolution of

UO_2 powder in O_2 (≥99.999%) saturated, 10 NaHCO3 (Merck). The powder was separated from the solution through consecutive centrifugation at 12000 rpm. The complete removal of the powder was determined by the absence of a change in the measured absorbance after the final centrifugation. The initial concentrations of 200μM H_2O_2 and 300μM UO_2^{2+} in uranyl containing solutions were chosen as to correspond to an equal amount of μ-η^2:η^2-peroxo and free H_2O_2 at the start of the irradiation [129].

Continuous purging with N_2O (≥98.0%), N_2 (≥99.999%) or O_2 (≥99.999%) were used during irradiation. The glass needle used as gas inlet was kept submerged in the irradiated solution. Irradiation was carried out in a MDS Nordion Gammacell 1000 Elite, equipped with a 137Cs source. The γ-rays emitted upon decay of ^{137m}Ba (formed from β-decay of ^{137}Cs) → ^{137}Ba + γ, has the photon energy 0.6617 MeV [130]. The dose rate was determined by Fricke dosimetry as 0.1851 ± 0.0023 Gy s^{-1}. The Fricke calibration was carried out as described by Spinks and Woods [21] by irradiating a solution of 1 mM ferrous ammonium sulfate, 1 mM NaCl and 0.4 M H_2SO_4. The absorbance of Fe^{3+} was measured at 304 nm.

The uranyl concentration was measured before and after irradiation. No change in the uranyl concentration was observed under any of the atmospheres used (N_2O-, N_2- or O_2 – purged).

6.3.3 Paper IV

The UO_2 powder was initially reduced to stoichiometric $UO_{2.0}$ through calcination in a furnace kept at 650°C for 3 hours under 5% H_2 + Ar atmosphere. Successful reduction was confirmed in XRD through comparison with reference spectra. The reduced powder was left to oxidize in milli-Q water sparged with O_2 (≥99.999%) for 30 days. The oxidation state after the oxidation was calculated as $UO_{2.47}$ based on deconvolution of the U4f 7/2 peak in XPS. The deconvolution is shown in Fig. 6.3.

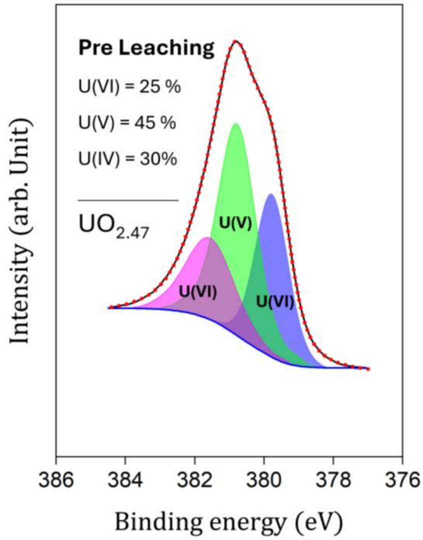

Fig 6.1. Deconvolution of U4f 7/2 for the pre-exposed uranium oxide powder before leaching.

A setup for dissolution exposures was designed to avoid the intrusion of atmospheric oxygen during leaching and allow for accurate and stable temperature control. A schematic representation of the setup is shown in Fig. 6.4.

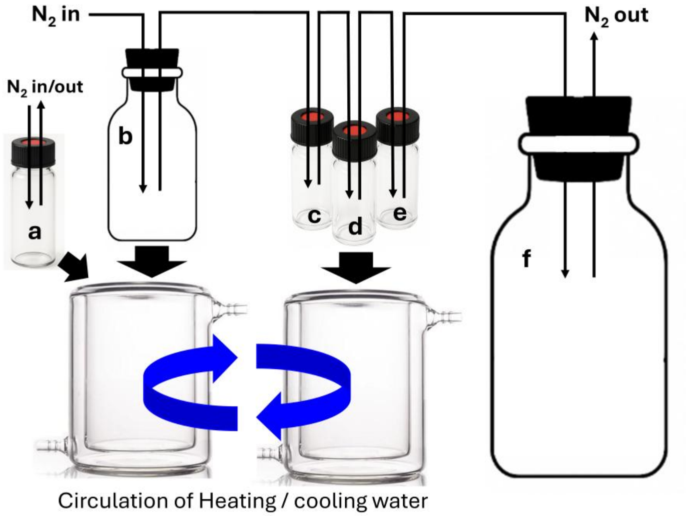

Fig 6.2. Schematics of the experimental setup with a separate vessel for purging and temperature regulation of the carbonate solution (a), humidifier and temperature regulator for the in gas (b), exposure vessels for 5-, 10- and 15 mM bicarbonate (c-e) and an N_2 reservoir preventing air backflow (f).

Two jacketed beakers were connected to a Huber Polystat K6 heat / cooling circulator. The inner beaker was filled with water in which temperature regulated glass vessels were submerged. $NaHCO_3$ solutions were prepared in (a) followed by 5-minute purging and temperature regulation to reach the desired temperature of the dissolution before being introduced to the powder. Solutions were transferred from (a) to the exposure vessel (c, d, e) and sampled using a syringe and needle. The solution was replaced for each point of measurement to avoid the build-up of [UO_2^{2+}] above the order of 10^{-5} M as it was found to influence the rate of dissolution through adsorption/desorption equilibria. The gas was temperature regulated and humidified in vessel (b) before entering the exposure vessels. This avoids a cooling effect of the N_2, and humidification ensures minimal water loss to the otherwise dry gas which would otherwise lead to significant concentration change due to evaporation at high temperature exposures. Lastly, the outgoing N_2 passed through a large beaker which served as an N_2 reservoir. This was necessary as the extraction of sample volume from the exposure vessels c, d and e creates a vacuum. The large volume of air free gas thus prevents atmospheric O_2 from entering through back suction.

6.3.4 Paper V and VI

The full experimental procedure from deposition of the UO_2 thin films to plasma exposure was carried out within stations of an integrated system under ultra-high vacuum (UHV).

UO_2 films were deposited on gold substrates through plasma deposition in the film synthesis chamber. The acceleration of ionized argon towards the uranium target (U^0 at -700 V) causes collision. The kinetic energy of the colliding argon ions causes separation of U atoms from the target, some of which are captured on the Au substrate. The presence of a controlled amount of O2 mixed with the argon results in a stoichiometric UO2 film, as confirmed by analysis in XPS. The partial pressures used were 6.3×10^{-3} mbar for Ar and 2×10^{-6} mbar O_2.

Pd doping was obtained through vaporization. The piece of Pd metal was clamped onto a tungsten heating filament, connected to two electrodes and placed ~ 4 cm away from the uranium oxide film. The setup is shown in Fig 6.1. A steady deposition rate was obtained by keeping the current fixed at 10.1 A through the tungsten filament. At this rate a 15 percent Pd / U ratio was reached after 3 min deposition, as estimated by core level analysis of the ratio between U4f and Pd3d and their relative ionization cross section (Pd3d having approximately half that of U4f). This ratio is averaged over the XPS information depth, and the palladium is not expected to be uniformly distributed in this region. The palladium forms nano sized spherical metal particles which diffuse within UO2-based thin film at temperatures (150-200 °C) [131, 132]. The estimated atom percentage of Pd was mainly useful for confirming the reproducibility of the deposition procedure. The second synthesis chamber was also used for removal of the UO_x films through sputter cleaning of the Au substrate with argon plasma before deposition of a new film.

Fig. 6.3. Palladium vapor deposition on a UO_2 thin film.

Plasma exposures were carried out in a third chamber. A photo of the setup is shown in Fig 6.2. Water, hydrogen, oxygen plasmas were generated using an electron cyclotron resonance (ECR) plasma source (Tectra GmbH, Frankfurt/M – Gen I). The atomic flux was specified to > 1×10^{16} cm^{-2} s^{-1}, corresponding to an exposure rate of > 1.33×10^{-3} Pa s^{-1} [133]. The plasma was introduced through an array of small capillaries located approximately 5 cm above the sample holder. H_2 gas was introduced through a separate inlet positioned close to the sample. The temperature of the sample stage was regulated using a pyrolytic boron nitride (PBN) heater mounted beneath the sample holder. The composition of the exposure atmosphere was monitored by a residual gas analyzer (RGA) equipped with a quadrupole mass spectrometer. Owing to the indirect positioning of the RGA relative to the plasma inlet, signals from highly reactive transient species (e.g., O, OH) were strongly attenuated by recombination reactions and interactions with metallic surfaces of the chamber components.

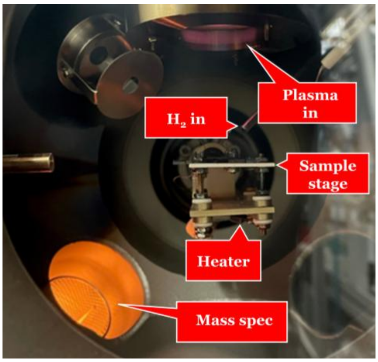

Fig. 6.4. Sample holder under an ECR plasma source.

7 Results & Discussion

7.1 The effect of uranyl μ-η^2:η^2-peroxo coordination on the reactivity of H_2O_2 towards UO_2

UO_2^{2+} strongly coordinates peroxide. This coordination often causes formation of secondary phases (i.e. studtite) on the surfaces of UO_2-based fuels. In such phases, the peroxide binds as a side-on bridging ligand with both oxygens of the peroxide coordinating two uranyl ions (μ-η^2:η^2) [134]. This bridge formation may be extended to form macro size crystals. If sufficient carbonate is present however, significant growth is prevented by formation of $(UO_2)_x(O_2)_y(CO_3)_z^{2x-2y-2z}$ complexes, the most stable configuration of which is typically $(UO_2)_2(O_2)(CO_3)_4^{6-}$ [135]. Many kinetic studies of H_2O_2 induced UO_2 dissolution have been carried out as batch reactions where $[UO_2^{2+}]$ buildup to some degree inevitably occur. It is therefore crucial to assess the potential change in peroxide reactivity towards UO_2 as the peroxide speciation shifts from H_2O_2 to UO_2^{2+}-coordinated μ-η^2:η^2-peroxo.

A series of UO_2 powder exposures were performed in 10mM $NaHCO_3$ solutions. An initial 200 μM H_2O_2 was used, high enough to accurately measured with the triiodide method and low enough as to not cause a significant change in the UO_2 powder surface area. The solutions were spiked with UO_2^{2+} by addition of uranyl nitrate before exposure to shift the speciation of the peroxide. The initial UO_2^{2+} concentrations were set to 0-, 0.3- and 0.6 mM corresponding to approximately 100-, -50 and 10 percent of the peroxide in the form of free H_2O_2 at the start of the exposure.

Fig. 7.1 shows the total peroxide concentration (a), the uranyl concentration (b) and dissolved UO_2^{2+} per amount of peroxide consumed (c) as functions of exposure time. The peroxide speciation (log concentrations as functions of exposure time) calculated with the set och equilibrium constants presented by Zanonato et al. [135] are shown in Fig 7.2.

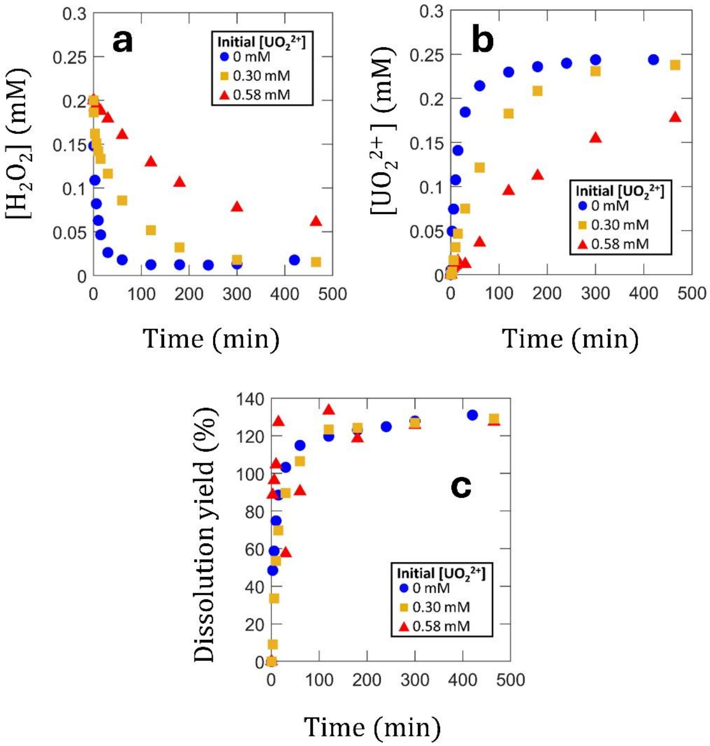

Fig 7.1 Measured peroxide- (a) and uranyl (b) concentrations and dissolution yields (c) as functions of exposure time.

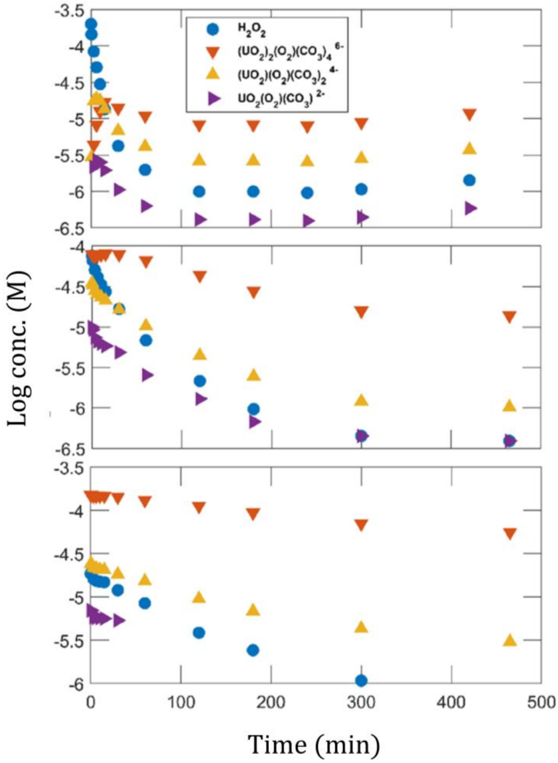

Fig. 7.2. Peroxide speciation as functions of exposure time for 0- (a), 0.3- (b) and 0.6 (c) mM initial $[UO_2^{2+}]$ and 0.2 mM initial [peroxide].

It is observed in Fig. 7.2 b that the rate of dissolution is suppressed by the presence of uranyl. This suppression is reflected by reactivity of the peroxide which clearly decreases as $[UO_2^{2+}]$ increases. The dissolution yield (i.e. amount of dissolved UO_2^{2+}) appears unaffected which means that UO_2^{2+} merely slows down the rate of peroxide consumption without interfering with the pathway through which it is consumed. This is consistent with a mechanism where an increasing fraction of the peroxide becomes inert due to the shifting of the equilibrium towards UO_2^{2+}-coordinated μ-η²:η²-peroxo.

If the coordination effect alone is responsible for the lower reactivity of the peroxide in the presence of uranyl, a first order rate dependence with respect to the fraction of free H_2O_2 is expected. This was tested by attempting to reproduce the rates observed by Barreiro Fidalgo et al [34]. In their dataset, the initial H_2O_2 concentration was varied. This ultimately leads to variations in the UO_2^{2+}

concentration, which increases with the turnover of H_2O_2. Calculated concentrations of free H_2O_2 as functions of the reported peroxide and UO_2^{2+} concentrations are shown in Fig 7.3.

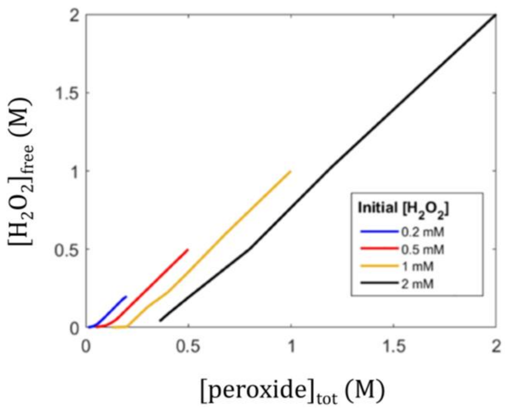

Fig. 7.3. Simulated free H_2O_2 vs measured peroxide [33].

The expected effect of the μ-η^2:η^2-peroxo coordination is mainly a parallel shift, such that the rate of peroxide consumption would appear to stop while a measurable amount of peroxide remains in the solution (due to a very limited fraction of free H_2O_2 available to react with the UO_2 surface). The authors reported an isotherm like behavior where the rate of peroxide consumption appears to depend on the relative H_2O_2 surface coverage. This cannot be explained by speciation effects as it is observed well before enough UO_2^{2+} has been dissolved to cause a significant shift in the peroxide speciation. It is clear however that the parallel shifts of Fig 7.3 are also reflected in their rates.

Comparison of their experimental rates (solid lines) and calculated rates based on first order kinetics with respect to the simulated concentration of free H_2O_2 (dashed lines) are shown in Fig. 7.4 a, with the corresponding comparison for the UO_2^{2+} spiked solutions shown in Fig. 7.4 b. The surface saturation effect has been accounted for by determining the rate constant for each solution separately from the initial rate of the peroxide consumption where speciation effects are negligible.

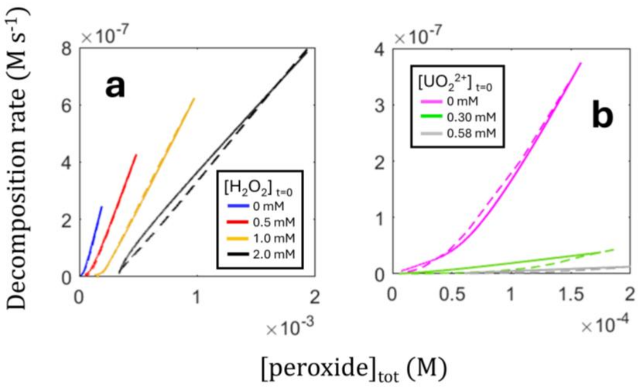

Fig. 7.4. Measured- and predicted (speciation adjusted) rates as functions of total peroxide concentration without added uranyl (a) and with added uranyl (b).

Clearly, there is agreement between observed rates and calculated rates based on first order kinetics with respect to the fraction of free H_2O_2. Peroxide consumption can therefore be accounted for by the reaction between H_2O_2 and UO_2 with no other pathways for peroxide consumption which also explains the lack of change in the dissolution yield. This observation was further supported by studying the catalytic decomposition of H_2O_2 on ZrO_2 in the presence of tris (hydroxymethyl) aminomethane (Tris, CAS: 77-86-1). Tris is known to react with H-abstracting radicals (including the surface bound HO• formed upon splitting of H_2O_2 on ZrO_2). Formaldehyde is one of the products formed which can be quantified using a modified version of the Hantzsch reaction [112].

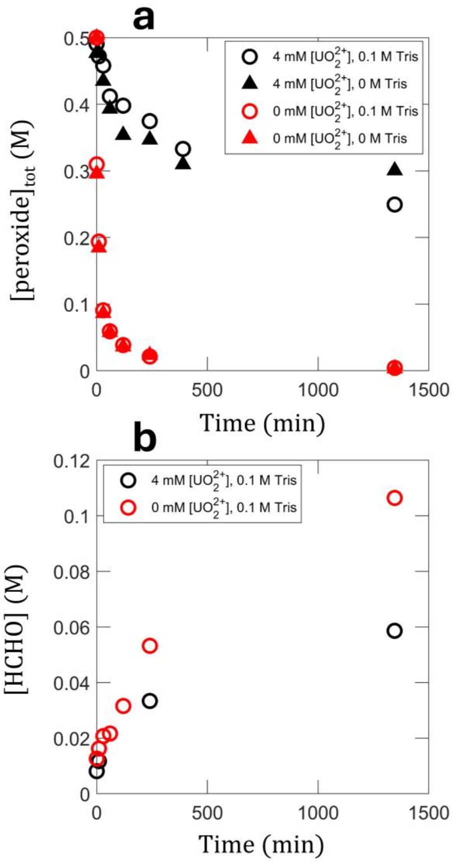

Figure 7.5. Measured peroxide- (a) and formaldehyde (b) concentrations as functions of exposure time.

The yield of formaldehyde was found to be the same in the presence and absence of uranyl while the rate was found to be significantly suppressed by the presence of UO_2^{2+}, further supporting the idea of kinetic suppression without change of decomposition mechanism.

7.1.1 The effect of uranyl μ-η^2:η^2-peroxo coordination at various carbonate concentrations

The investigation of suppressed peroxide reactivity due to μ-η²:η²-peroxo coordination was extended to included several carbonate concentrations over the range of carbonate concentrations relevant for groundwater at planned repository sites (1 – 10) mM.

UO_2 powder exposures were performed in 1, 2, 5, and 10 mM $NaHCO_3$ with an initial H_2O_2 concentration of 200 μM and no initial UO_2^{2+} spike. The measured peroxide- and UO_2^{2+} concentrations are shown in Figure x a and b respectively.

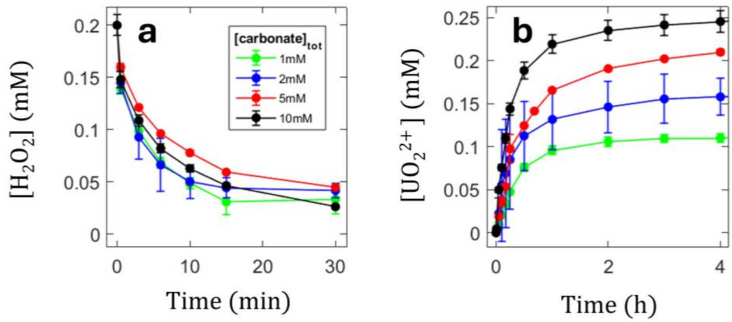

Fig. 7.6. Measured peroxide- and uranyl concentration as functions of exposure time.

The peroxide concentrations in Fig. 7.6 a are observed to proceed to near full depletion at a relatively rapid rate for all carbonate concentrations. However, the dissolution yield appears affected by variations in carbonate concentration. This could either be caused by solubility limitations with most of the oxidized UO_2^{2+} adsorbed to the powder at lower carbonate concentrations, or by changes to the peroxide consumption mechanism, resulting in a lowering of the dissolution yield with lower bicarbonate concentration. Corresponding exposures were performed with an initial spike of 300 μM UO_2^{2+}. Measured peroxide- and UO_2^{2+} as functions of reaction time is shown in Fig. 7.7 a and b respectively.

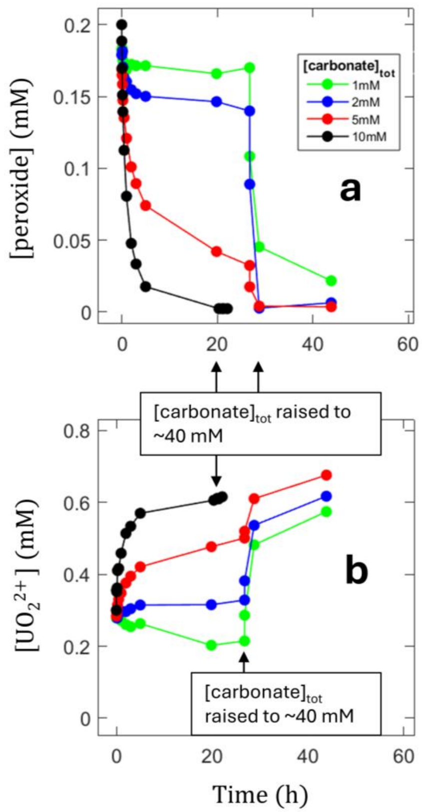

Fig. 7.7. Measured peroxide- and uranyl concentration as functions of exposure time in carbonate solutions with 0.3 mM added UO_2^{2+}.

A clear suppression of the peroxide reactivity is observed in Fig. 7.7 a, which becomes increasingly prominent at lower carbonate concentrations. At carbonate concentrations < 2 mM, a small fraction of the peroxide is initially consumed whilst further consumption of the remaining peroxide appears almost completely blocked. When raising the carbonate concentration to 40 mM, suppression is immediately lifted and most if not all UO_2^{2+} is recovered, suggesting that the initial peroxide drop observed at 1- and 2 mM bicarbonate also occurs via oxidation of UO_2. The fractions of free peroxide (H_2O_2) and free carbonate (HCO_3^-+CO_3^{2-}) for the UO_2^{2+} spiked solutions are shown in Fig 7.8 a and b respectively. The fractions have been calculated for three different time points of the exposure; (1) start of exposure, (2) after the initial peroxide drop (~5 h) and (3) prior to carbonate addition (20/26 h).

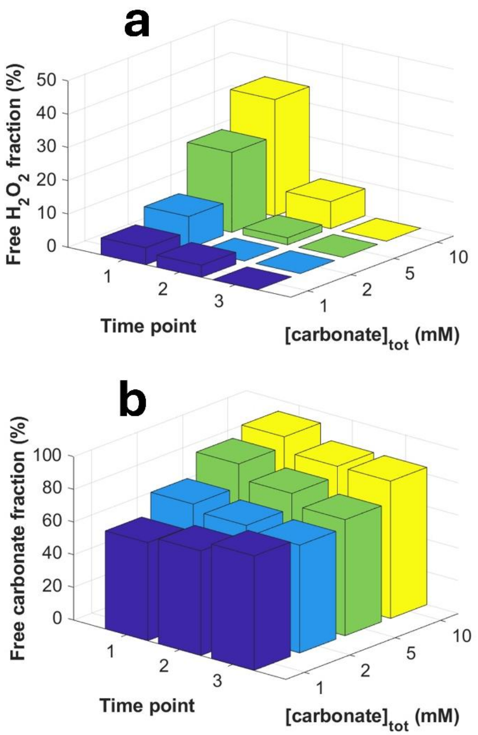

Fig. 7.8. Calculated fractions of free H_2O_2 (a) and free carbonate/bicarbonate as functions of carbonate concentration at three stages of the reaction; 1: start of the exposure, 2: after initial peroxide drop (~5h) and 3:prior to carbonate addition (20/26h).

Based on the speciation calculations, the fraction of free H_2O_2 (Fig. 7.8 a) is expected to be limited whilst a significant amount of free carbonate (Fig. 7.8 b, HCO_3^-+CO_3^{2-}) is expected to be available in all solutions throughout the exposures. The lifting of the suppression of peroxide reactivity as the carbonate concentration is raised becomes clear by considering the shifting of the uranyl speciation. The calculated speciation at the time of the carbonate addition is shown in Fig 7.9.

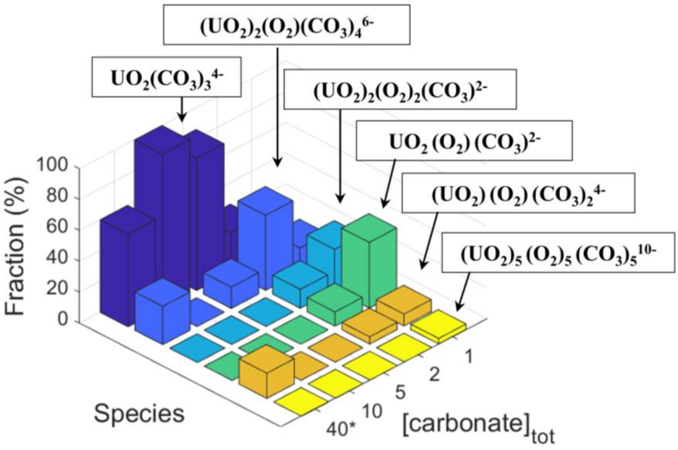

Fig. 7.9. Uranyl speciation at the time of carbonate addition.

As CO_3^{2-} competes with O_2^{2-} for UO_2^{2+} coordination centers, the additional carbonate shifts the uranyl speciation away from UO_2^{2+}-coordinated peroxo ligands towards the carbonate complex $UO_2(CO_3)_3^{4-}$. This causes the release of reactive H_2O_2 (by dissociation of O_2^{2-} and UO_2^{2+}-centers). The results above show that the suppression of peroxide reactivity towards UO_2 by UO_2^{2+}-coordination becomes increasingly significant at lower carbonate concentrations and the ratio between UO_2^{2+} and carbonate is thus crucial for the overall reactivity of peroxide.

The impact of ionic strength at high (10 mM) and low (1 mM) carbonate concentration was assessed, to test the early hypothesis that the lower reactivity of the coordinated peroxide is caused by electrostatic repulsion between the complex and the surface. The ionic strength was varied by the addition of $NaClO_4$ due to the weak interaction between ClO_4^- and UO_2^{2+}. Measured peroxide- and UO_2^{2+} concentrations as functions of exposure time in 10mM bicarbonate are shown in Fig. 7.10 a and b respectively. The corresponding data for exposures in 1 mM bicarbonate are shown in Fig 7.11 a and b.

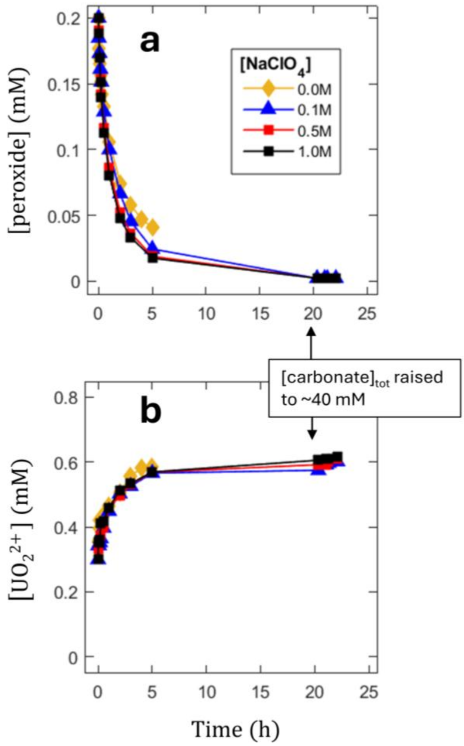

Figure 7.10. Peroxide (a) and uranyl (b) concentration as functions of exposure time in 20 ml solutions containing 10 mM bicarbonate, 0.3 mM initial uranyl and 0–1 M $NaClO_4$, with 30 mg UO_2 powder suspension (SA/V = 8100 m^{-1}).

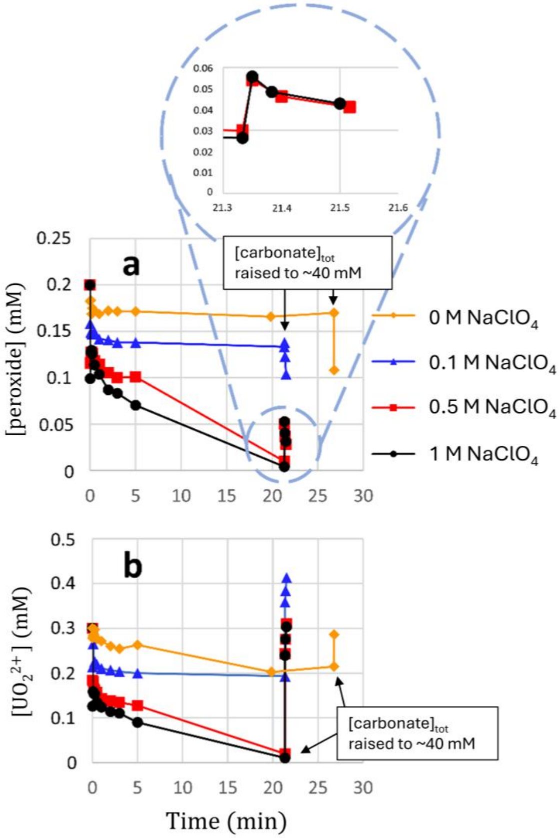

Figure 7.11. Peroxide (a) and uranyl (b) concentration as functions of exposure time in 20 ml solutions containing 1 mM bicarbonate, 0.3 mM initial uranyl and 0–1 M $NaClO_4$, with 30 mg UO_2 powder suspension (SA/V = 8100 m^{-1}).

The increase in ionic strength does not appear to significantly change the peroxide reactivity (or UO_2^{2+} dissolution rate) in solutions of 10 mM bicarbonate as seen in Fig. 7.10.

In 1 mM bicarbonate solutions, increasing the ionic strength impacts the solubility of both the peroxide and UO_2^{2+}. In Fig 7.11 a, a gradual decrease in the peroxide concentration is observed at high ionic strengths ([$NaClO_4$] ≥ 0.5 M). The same drop is reflected in the measured UO_2^{2+} concentration. This is therefore not the typical reaction observed between H_2O_2 and UO_2 but rather adsorption and formation of a secondary phase. Based on the 1:1 ratio of the lost H_2O_2 to lost UO_2^{2+} this is likely studtite formation. At lower ionic strength

([$NaClO_4$] ≤ 0.1 M) raising the carbonate concentration once again activates the peroxide. Increasing the carbonate concentration at high ionic strength confirms the secondary phase formation as the lost UO_2^{2+} is immediately recovered along with partial recovery of the peroxide.

7.2 The effect of uranyl μ-η^2:η^2-peroxo coordination on the stability of H_2O_2 in irradiated bicarbonate solutions

In this section, the impact of UO_2^{2+} on the H_2O_2 stability in irradiated solutions is elucidated. This stability is of key importance as it reflects the probability of radiolytically formed H_2O_2 surviving long enough to interact with the UO_2 surface, which ultimately determines the rate of oxidation induced by H_2O_2.

γ-radiation induces H_2O decomposition and subsequent formation of radiolytic oxidants ($HO^\bullet$, $HO_2^\bullet/O_2^{\bullet-}$, H_2O_2) and reductants (e^-_{aq}, $H^\bullet$, H_2). Escape yields, as reported by Pastina & LaVerne [58] are listed in Table 7.1.

Table 7.1. Escape yields (γ radiation)

Species	G-values (μmol J^{-1})
G($HO^\cdot$)	0.28
G(H_2O_2)	0.073
G($HO_2^\cdot$)	0.0021
G(e_{aq}^-)	0.27
G($H^\cdot$)	0.068
G(H_2)	0.047

Buildup of H_2 is prevented by continuously purging the solution during irradiation. In the aqueous solution, H_2O_2 is formed through local radical recombination in spurs with an escape yield 7.3×10^{-8} mol J^{-1}. This corresponds to a formation rate of ~1.4×10^{-8} M s^{-1} (at dose rate 0.1851 J kg^{-1} s^{-1}). Secondary H_2O_2 formation occurs due to disproportionation of superoxide and its protonated form ($HO_2^\bullet$).

$$\mathrm{HO_2^\bullet + O_2^{\bullet -} + H_2O \rightarrow O_2 + H_2O_2 + OH^-} \quad (7.1)$$

$$\mathrm{2\,HO_2^\bullet \rightarrow O_2 + H_2O_2} \quad (7.2)$$

The second order rate constants have been reported as $k_{7.1}$ = 7.61 ± 0.55) × 10^5 M^{-1} s^{-1} and $k_{7.2}$ = (8.86 ± 0.44 × 10^7 M^{-1} s^{-1} and the apparent rate of disproportionation can be expressed as a function of pH and total superoxide ($O_2^{\bullet -}$ + $HO_2^\bullet$) concentration

$$k_{app} = \frac{k_x + k_y * 10^{-pKa} * 10^9}{(1+10^{-pKa} * 10^{pH})^2} \quad (7.3)$$

as derived by Bielski and Allen [114]. The pKa of $HO_2^\bullet$ has been reported within the range 4.7 – 4.9 [114-116]. Disproportionation requires at least one of the radicals to be in the protonated form. Consequently, the apparent rate increases at lower pH.

H_2O_2 is consumed through oxidation by $HO^\bullet$ as well as through reduction by e^-_{aq} and $H^\bullet$. In 10mM bicarbonate nearly all HO will react with HCO_3^-/CO_3^{2-} to form the carbonate radical ($CO3^{\bullet -}$). This radical consumes H_2O_2 through H-abstraction with reported rate constants (4 – 8) × 10^5 M^{-1} s^{-1} [118, 119].

To elucidate the impact of UO_2^{2+} on the various pathways for peroxide consumption and production, three different conditions were studied:

(i) N_2O-purged solutions
(ii) N_2-purged solutions
(iii) O_2-purged solutions

Under the first condition, e^-_{aq} and $H^\bullet$ are effectively scavenged by N_2O to form $HO^\bullet/O^{\bullet -}$ which subsequently react with carbonate species to form $CO_3^{\bullet -}$.

$$\mathrm{N_2O + e^-_{aq} \rightarrow N_2 + O^{\bullet -}} \quad (7.4)$$

$$\mathrm{N_2O + H^\bullet \rightarrow N_2 + HO^\bullet} \quad (7.5)$$

Consequently, peroxide is consumed almost exclusively via oxidation by $CO_3^{\bullet -}$.

Under the second condition, the purge gas (N_2) is inert and merely facilitates the continuous removal of O_2. In the absence of scavenger, e^-_{aq} and $H^\bullet$ are expected to reduce peroxide until the peroxide concentration is low enough to allow competition with radical-radical reactions.

Under the third condition the O_2 serves as a second type of scavenger for e^-_{aq} and $H^\bullet$. Unlike scavenging under the 1st condition, the product ($HO_2^\bullet/O_2^{\bullet -}$) is not strongly reactive towards H_2O_2. Rather than consuming H_2O_2 it is mainly expected to contribute to H_2O_2 formation via superoxide disproportionation. The various pathways for peroxide consumption and production are schematically represented in Fig. 7.12.

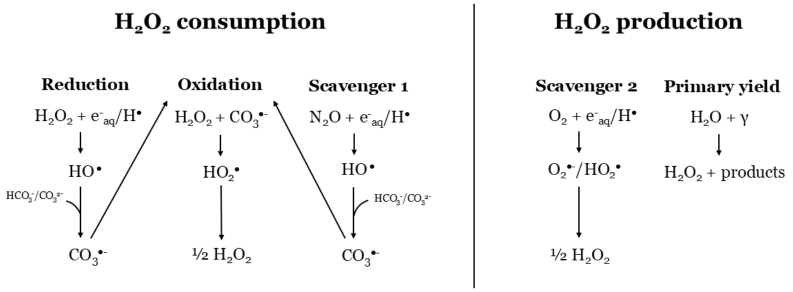

Fig. 7.12. Schematic representation of the pathways for peroxide consumption and peroxide production in irradiated 10mM bicarbonate solutions.

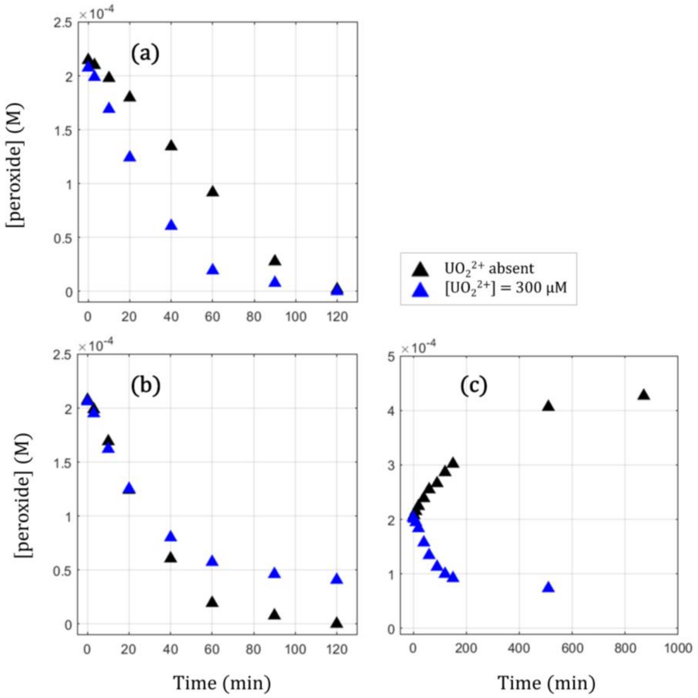

Fig. 7.13. Measured peroxide concentrations as functions of time under irradiation, in N_2O-purged (a), N_2-purged (b) and O_2-purged (c) 10mM $NaHCO_3$ solutions with 0/300μM UO_2^{2+}.

In the N_2O-purged solution (Fig. 7.13 a) the presence of 300μM UO_2^{2+} approximately doubles the net consumption rate (compared to the corresponding solution without UO_2^{2+}).

In the N_2-purged solution (Fig. 7.13 b) the initial rate of peroxide consumption appears to be the same in the presence and absence of 300μM UO_2^{2+}. The two rates diverge as the solution containing 300 μM UO_2^{2+} appears to approach steady state at [peroxide] ~ 400 μM whilst consumption proceeds further in the UO_2^{2+}-free solution. Note the similarity between the UO_2^{2+}-free N_2-purged solution (Fig. 7.13b, black triangles) and the N_2O-purged solution containing 300 μM UO_2^{2+} (Fig. 7.13a, blue triangles). The reason for this similarity will be discussed below.

In the O_2-purged solution (Fig. 7.13 c) the buildup of peroxide is clearly suppressed by the presence of UO_2^{2+}. The scavenging of e^-_{aq} and $H^\bullet$ by O_2 blocks the pathway of peroxide reduction and the consumption is expected to primarily be oxidation of H_2O_2 by $CO_3^{\bullet-}$. 300μM UO_2^{2+} is expected to double the net peroxide consumption rate as was observed in the N_2O-pruged solution. The double net peroxide consumption, however, cannot explain the over 5 times higher steady state observed in the O_2-purged UO_2^{2+}-free solution, compared to the corresponding solution with 300μM UO_2^{2+}. This is more likely caused by UO_2^{2+} catalyzing a reaction between superoxide and H_2O_2. The uncatalyzed reduction of H_2O_2 by $O_2^{\bullet-}$ is known as the Haber-Weiss reaction. This reaction is slow, with varied reports of $k_{7.6}$ from $< 1 \times 10^{-4}$ [137] – to 2.3 $M^{-1}\,s^{-1}$ [138] with the later estimate 0.13 $M^{-1}\,s^{-1}$ [128].

$$O_2^{\bullet-} + H_2O_2 \rightarrow O_2 + HO^{\bullet} + OH^{-} \qquad (7.6)$$

If catalyzed by UO_2^{2+} however, the reduction of peroxide by $O_2^{\bullet-}$ would enable a chain reaction, where the formation of $HO^\bullet$ ultimately regenerates superoxide via peroxide oxidation (see Fig. 7.12).

To visualize the expected contributions of the various peroxide consumption and production pathways, calculations of the relative contributions were made through implementation of the simplified kinetic model presented under section 6.2.3.

7.2.1 Simulated vs experimental [H_2O_2] and simulated H_2O_2 production/consumption pathway fractions in the UO_2^{2+}-free solutions

The accuracy of the simplified radiolysis model will first be discussed in terms of the agreement between the simulated [H_2O_2] and the experimental observations for the UO_2^{2+}-free N_2O-, N_2- and O_2-purged solutions. Comparison of simulated and measured H_2O_2 concentrations as functions of irradiated time with initially spiked H_2O_2 concentrations of 2×10^{-4} M is shown in Fig. 7.14 a. Additionally, comparisons of the simulated vs the measured buildup of H_2O_2 (from zero initial [H_2O_2]) in N_2O purged and O_2 solutions are presented in Fig 7.14 b and c respectively. The H_2O_2-spiked solutions provide an assessment of the quality of the simulation in systems where H_2O_2 production and consumption occur with little competition from radical-radical reactions. The pure 10mM bicarbonate solutions (Fig. 7.14 b and c) on the other hand, show the quality of the simulations under conditions where more radical-radical competition is expected. The steady state of H_2O_2 in the N_2-purged solution is below the detection limit of the Ghormley method. The N_2-purged system can therefore only be studied in terms of net consumption observed with an initial H_2O_2 spike.

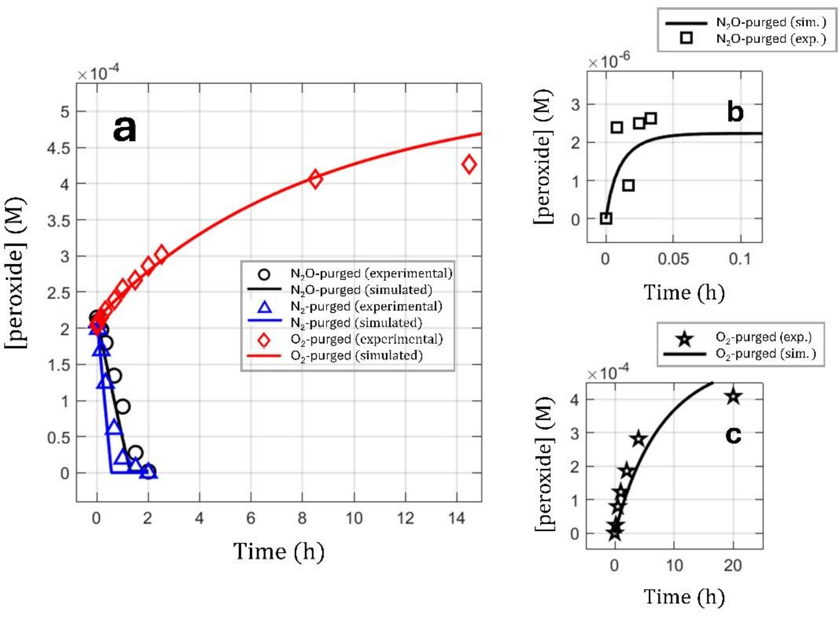

Fig. 7.14. Comparison of simulated (solid lines) and measured peroxide (open symbols) in H_2O_2-spiked (a) and unspiked (b and c) 10 mM bicarbonate solutions. Simulations were performed using the model as presented in Table 1.

As shown in Fig. 7.14 a, the model shows good agreement with the overall trends observed for $CO_3^{\bullet-}$ driven peroxide consumption (N_2O-purged system), mixed $CO_3^{\bullet-}$, e^-_{aq} and $H^\bullet$ driven peroxide consumption (N_2-purged system) and $CO_3^{\bullet-}$ driven peroxide consumption with increased $O_2^{\bullet-}$ induced peroxide formation (O_2-purged system). Notably, the experimental rates of peroxide consumption are lower than the predicted rates for both the N_2O-purged and N_2-purged solutions. The discrepancy between the experimental- and predicted rate appears more prominent at low [H_2O_2] in the N_2-purged solution, indicating an underestimation of radical-radical reactions in solutions with both oxidizing and reducing radicals present. This does not appear to be the case for the N_2O-purged system where only oxidizing radicals ($CO_3^{\bullet-}$) are present, in which case the predicted steady state appears to be in good agreement with the experimental data (Fig. 7.14 b). The initial peroxide formation in the O_2-purged solution is notably faster than the predicted rate as shown in Fig. 7.14 c. Additionally, the steady state of H_2O_2 is slightly overestimated by the model (500 vs 430 μM).

The model was used to quantify the relative contributions of the various pathways for peroxide production and consumption. These are presented as fractions Φ, where the rate of each pathway leading to peroxide production/consumption r_i, is divided by the sum of rates for all pathways leading to peroxide production/consumption ($\Phi \equiv \frac{r_i}{\sum_j r_j}$). Data from the simulations of UO_2^{2+}-free N_2O-, N_2- and O_2-purged solutions are shown in Figures 7.15 – 7.17, including measured vs simulated peroxide (a), log concentrations of radiolytic species (b), and the relative contributions of each peroxide formation (c) and consumption (d) reaction.

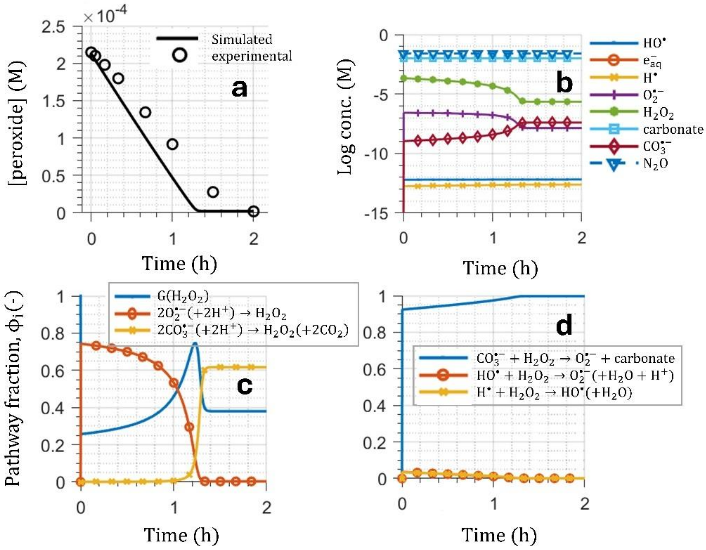

Fig. 7.15. N_2O-purged, UO_2^{2+}-free. (a) H_2O_2 concentration vs irradiation time, (b) Simulated $\log_{10}$ concentrations of included radiolytic species. Fractional contribution of; (c) H_2O_2-formation reactions and (d) H_2O_2-consumption reactions. Reaction fractions $\phi i \equiv ri/\sum_j r_j$ (unitless); fractions at each time sum to 1.

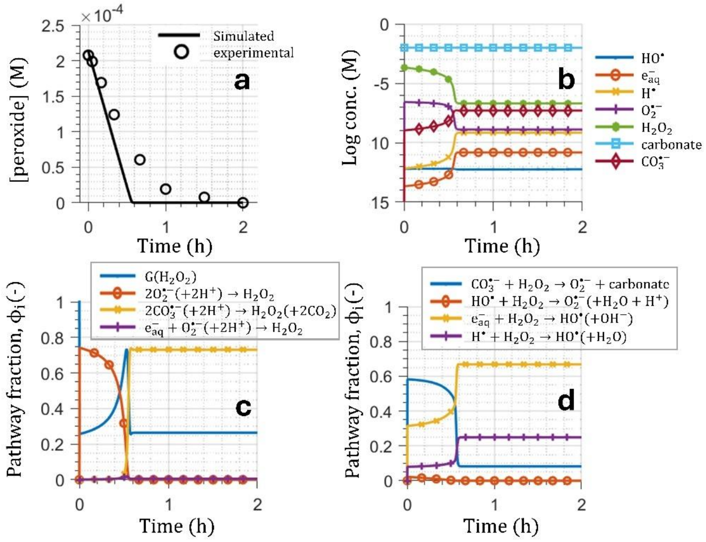

Fig. 7.16. N_2-purged, UO_2^{2+}-free. (a) H_2O_2 concentration vs irradiation time, (b) Simulated $\log_{10}$ concentrations of included radiolytic species. Fractional contribution of; (c) H_2O_2-formation reactions and (d) H_2O_2-consumption reactions. Reaction fractions $\phi i \equiv ri/\sum_j r_j$ (unitless); fractions at each time sum to 1.

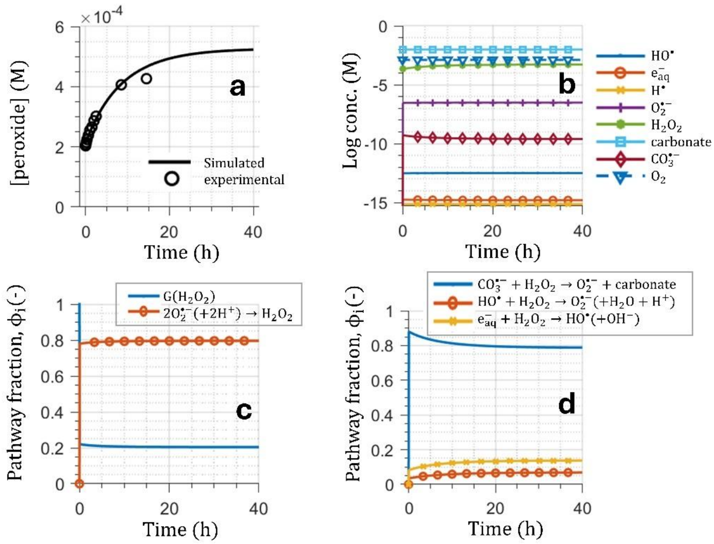

Fig. 7.17. O_2-purged, UO_2^{2+}-free. (a) H_2O_2 concentration vs irradiation time, (b) Simulated $\log_{10}$ concentrations of included radiolytic species. Fractional contribution of; (c) H_2O_2-formation reactions and (d) H_2O_2-consumption reactions. Reaction fractions $\phi_i \equiv r_i/\sum_j r_j$ (unitless); fractions at each time sum to 1.

As expected for the N_2O-purged solution, the model predicts a peroxide consumption almost exclusively driven by the reaction between H_2O_2 and $CO_3^{\bullet}$ as shown in Fig 7.15 d. This consumption produces superoxide which is predicted to be the main driver for peroxide formation until surpassed by $G(H_2O_2)$ at $[H_2O_2]$ below ~50 µM and finally by the radical combination reaction $CO_3^{\bullet}$+ $CO_3^{\bullet}$ as shown in Fig. 7.15 c.

In the N_2-purged solution, the relative contributions of the formation reactions are similar as shown in Fig. 7.16 c. The absence of scavenger for e^-_{aq} and $H^{\bullet}$ significantly changes the relative contribution of the peroxide consumption reactions as shown in Fig. 7.16 d, with 60 percent induced by $CO_3^{\bullet}$ and the remaining 40 percent by reduction.

In the O_2-purged solution, the main peroxide consumer is $CO_3^{\bullet}$ with a minor contribution from e^-_{aq} as well as direct oxidation by $HO^{\bullet}$ as shown in Fig. 7.17 d. As expected, the main peroxide formation is caused by disproportionation of $O_2^{\bullet-}$ (80 percent) with contribution from $G(H_2O_2)$ (20 percent) as shown in Fig 7.17 c. If the enhanced peroxide decomposition is caused by a UO_2^{2+}-catalyzed Haber-Weiss type mechanism, then the largest UO_2^{2+} effect is expected in the

O_2-purged solution where the contribution of superoxide disproportionation is the highest. By fitting the Haber-Weiss rate constant to the experimental rate observed in the O_2 system and using the same constant to simulate the UO_2^{2+} effect in the N_2O system, the quality of the proposed mechanism can be assessed based on the level of agreement between simulated and experimental rates in the latter case.

7.2.2 Assessing the agreement between observed UO_2^{2+} effects and predicted effects of a UO_2^{2+} catalyzed Haber-Weiss reaction

Good agreement between experimental and predicted data is obtained for both the H_2O_2 steady state and the net H_2O_2 consumption rate when the Haber-Weiss constant is set to k_{cat} = 4.3×10² M^{-1} s^{-1}. The simulated data for the O_2-purged system using the model with an updated Haber-Weiss rate constant is shown in Fig. 7.18.

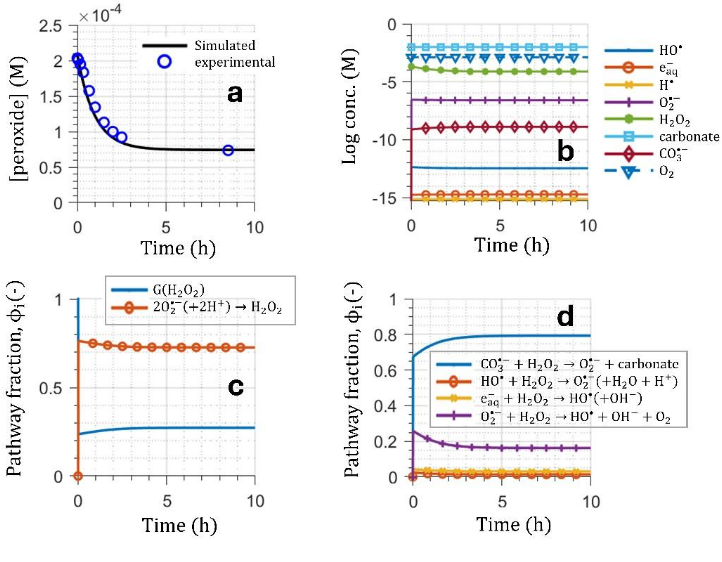

Fig. 7.18. O_2-purged, with UO_2^{2+} (simulated as Haber-Weiss constant k_{cat} = 4.3×10² M^{-1} s^{-1}). (a) H_2O_2 concentration vs irradiation time, (b) Simulated $\log_{10}$ concentrations of included radiolytic species. Fractional contribution of; (c) H_2O_2-formation reactions and (d) H_2O_2-consumption reactions. Reaction fractions $\phi i \equiv ri/\sum_j r_j$ (unitless); fractions at each time sum to 1.

As shown in Fig. 7.18 b, no significant change of the superoxide concentration is expected due to the reformation of superoxide in the Haber-Weiss chain reaction. Consequently, the rate of H_2O_2 formation would remain unchanged.

The main change here is the contribution of $O_2^{\bullet -}$-induced peroxide consumption shown in Fig. 7.18 d which accounts for ~15 percent of the overall consumption but in turn also generates $HO^{\bullet -}$ which enhances the rate of peroxide oxidation.

The comparison between experimental and predicted [H_2O_2] using the model with updated k_{cat} = 4.3×10² M^{-1} s^{-1} for the N_2O-purged solution is shown in Fig. 7.19.

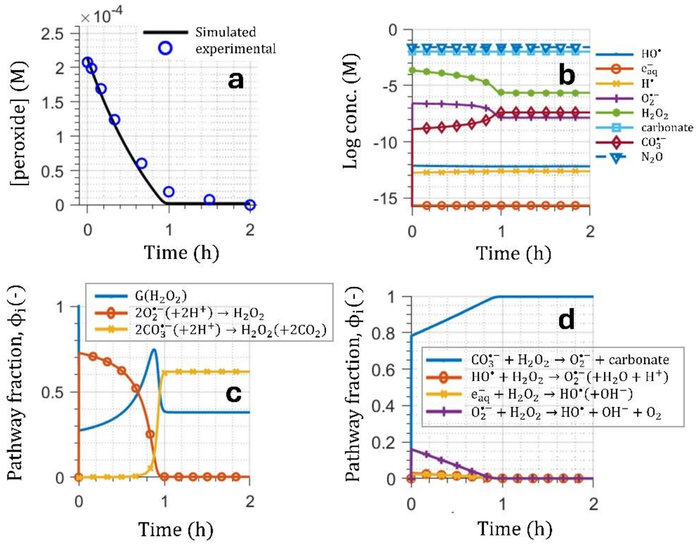

Fig. 7.19. N_2O-purged, with UO_2^{2+} (simulated as Haber-Weiss constant k_{cat} = 4.3×10² M^{-1} s^{-1}). (a) H_2O_2 concentration vs irradiation time, (b) Simulated $\log_{10}$ concentrations of included radiolytic species. Fractional contribution of; (c) H_2O_2-formation reactions and (d) H_2O_2-consumption reactions. Reaction fractions $\phi_i \equiv r_i/\sum_j r_j$ (unitless); fractions at each time sum to 1.

As shown in Fig. 7.19 a, the updated k_{cat} (fitted to the experimental data of the O_2-purged, 300 μM UO_2^{2+} solution) also accurately reproduces the enhanced rate and shape of the peroxide consumption in the N_2O-purged, 300 μM UO_2^{2+} solution.

There is obviously less agreement between predicted and observed data when no scavenger for reducing radicals is present (i.e. the N_2-purged solution) even in the absence of UO_2^{2+}. For the sake of clarity (and transparency), a comparison between observed and predicted UO_2^{2+} effect is still included in Fig. 7.20.

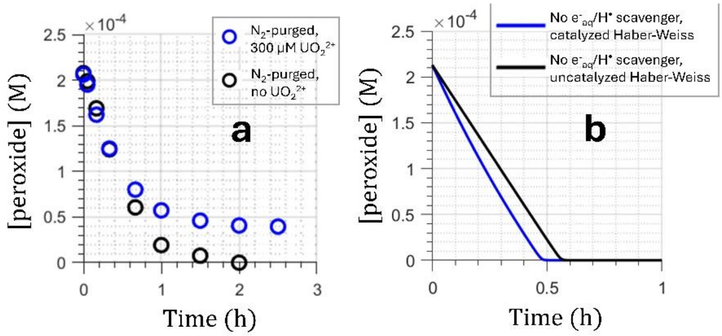

Fig 7.20. N_2-purged, with and without UO_2^{2+}. (a) Observed effect of UO_2^{2+} and (b) predicted effect based on enhanced Haber-Weiss constant $k_{cat} = 4.3\times10^2$ M^{-1} s^{-1} .

As shown in Fig. 7.20 a, there is no clear distinction between the initial rates in the presence and absence of UO_2^{2+}. This is consistent with the simulation as the difference in rate caused by the catalyzed Haber-Weiss reaction is expected to be quite small for the N_2-purged system. However, the rate of peroxide consumption is clearly affected by the presence of UO_2^{2+} for reasons that are not explained by the catalytic process alone. The radiolytic reductants in the absence of a scavenger can reduce UO_2^{2+} into UO_2^{+} [139, 140]. This could potentially serve as a sink for reductants, to lower the fraction of radiolytic reductants inducing peroxide consumption. Such an effect could easily mask the small, predicted difference (Fig. 7.20 b) caused by the catalysis of the Haber-Weiss reaction.

It should be noted that in the absence of O_2, UO_2^{2+} enhances peroxide stability in the γ-irradiated solution, likely through scavenging of reducing radicals which are expected to account for approximately 90 percent of the H_2O_2 consumption in the absence of UO_2^{2+} as shown in Fig. 7.16 d.

7.2.3 The impact of varied [UO_2^{2+}] on the peroxide stability under O_2 atmosphere

To assess the uranyl concentration dependence on peroxide stability in irradiated bicarbonate solutions under O_2 atmosphere, additional irradiations were performed at several uranyl concentrations within the range 0 – 300 µM. Measured peroxide concentrations as functions of irradiation time is shown in Fig. 7.21 with 0 – 100 µM uranyl shown in a and 300 µM uranyl shown separately in b with and without H_2O_2 spike.

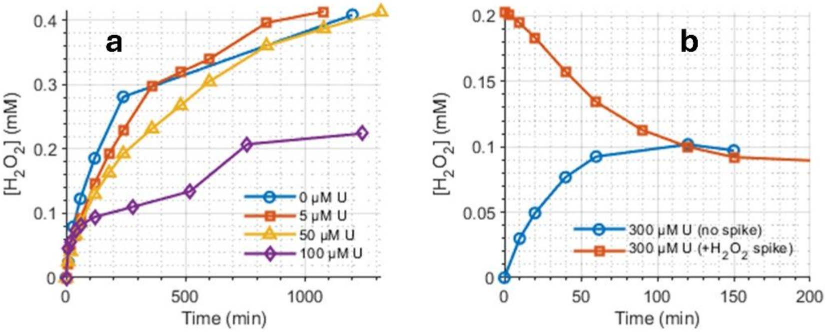

Fig 7.21. Measured peroxide in 10 mM bicarbonate solutions at uranyl concentrations 0 – 100 µM (a) and 300 µM (b).

In Fig. 7.21, several trends, crucial for the understanding of the catalytic effect can be distinguished. Firstly, the initial rates of peroxide formation in Fig. 7.21 a do not appear to be suppressed by the presence of uranyl. Only with sufficient buildup of H_2O_2 can a [UO_2^{2+}] dependent catalytic reduction be distinguished. This is a strong indication that the reduction by superoxide occurs selectively for μ-η^2:η^2-peroxo and does not involve the reduction of free UO_2^{2+} ions.

Secondly, the [UO_2^{2+}] dependence on the peroxide stability is complex. For [UO_2^{2+}] ≤ 100 µM, the peroxide formation proceeds at an exceedingly suppressed rate with increasing [UO_2^{2+}]. Remarkably, the final steady state does not appear to be influenced by UO_2^{2+} within this concentration range, meaning the catalytic effect must eventually become outcompeted by uncatalyzed superoxide phenomena such as disproportion and the uncatalyzed Haber-Weiss process. This can be explained by a saturation of available UO_2^{2+}-coordination centers, at which point the UO_2^{2+}-catalyzed Haber-Weiss type reaction becomes insensitive to further increase of the peroxide concentration. If a net positive rate of peroxide formation is maintained at the critical concentration when saturation of UO_2^{2+}-coordination centers is reached, then peroxide buildup is expected to proceed to the same steady state as the uranyl free, O_2-saturated bicarbonate solution (~ 4.5×10^{-4} M). On the other hand, if sufficient UO_2^{2+} is present to change the net rate from positive (+) to negative (-) before saturation occurs, then a lower steady state of peroxide is expected, as observed for 300 µM UO_2^{2+} (Fig. 7.21 b).

7.3 Carbonate mediated dissolution of oxidized UO_2 in the absence of simultaneous oxidation

The carbonate mediated dissolution of oxidized UO_2 had only been studied in conjunction with the oxidation process. The only published estimate of the temperature dependence for the dissolution mechanism, E_a = (35.7 ± 0.2) kJ mol^{-1}) [92], has been extrapolated from a complex mechanism where the apparent rate of UO_2^{2+} can be limited by either oxidation or dissolution (or even a combination of the two). Additionally, reported carbonate dependencies on the dissolution kinetics are inconsistent, with the apparent reaction orders n ≤ 2 reported by Schortmann and DeSesa [83] and n ≤ 1 by Nicol and Needs [94] and by de Pablo et al. [92, 93].

In this section, the temperature- and concentration dependence for the pure dissolution kinetics is studied in the absence of the oxidation process. This was obtained by pre-oxidizing $UO_{2.0}$ in O_2-saturated Milli-Q water for 30 days. The exposure starts as the powder is exposed to $NaHCO_3$ solutions, at which point the reaction vessel is kept anoxic (by continuous purging with N_2) and temperature regulated (externally through circulation of tempered water). The solution had to be replaced at each time point as the dissolution would otherwise quickly reach solubility limitations (particularly at lower bicarbonate concentrations (≤ 5 mM). Interference of atmospheric oxygen was avoided by pre purging the $NaHCO_3$ solution with N_2 in a separate vessel. The volume was extracted from the purge vessel with a syringe and injected into the reaction vessel through a septum.

Leching exposures with 5-, 10- and 15 mM $NaHCO_3$ at 6 different temperatures in the range (10 – 60) ^{o}C are shown in Fig. 7.22.

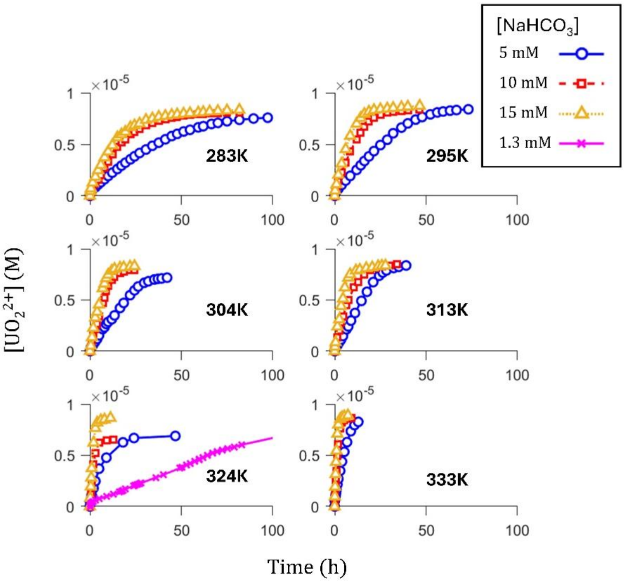

Fig. 7.22. Leaching of hyperstoichiometric $UO_{2.47}$ powder in bicarbonate solutions of (1.3-) 5-, 10, and 15 mM at six different temperatures within the range 283 – 333 K.

Fig. 7.22. shows that the amount of oxidized U(VI) available for dissolution is independent of both temperature and the time required to reach full dissolution (depletion of the oxidized product). This is crucial for the overall quality of the experiment as it shows that (I) interference from atmospheric oxygen during the leaching is negligible and (II) the measurement error which is accumulated for each measured point (due to replacement of the solution) is very small. Note that an additional concentration (1 mM $NaHCO_3$) was first used but was found to be too slow for convenience. Additionally, the solution quickly reached solubility limitations. A minimum of 5 mM was therefore used in later exposures. Nevertheless, the 1 mM exposure is included for the only temperature where it was used (50^{o}C /324 K).

Two key trends for the dissolution mechanism can be distinguished in Fig. 7.22. Firstly, the reaction order with respect to carbonate appears to be closer to 1st order than 2nd order with respect to carbonate (as reported by at least two earlier accounts [93, 94]). Secondly, the rate of dissolution appears near constant until the fraction of remaining oxidized product is small ~20 percent, as indicated by the lack of curvature in the amount of dissolved UO_2^{2+} vs time before approaching full dissolution. This 0th order dependence on the oxidized product can only be explained if the surface available to the carbonate remains unchanged which can only occur if the surface layer available to the carbonate is thin compared to the thickness of the oxidized surface layer. The constant composition of the reactive interface can be interpreted in two different ways. If the oxidized layer has an even degree of oxidation throughout, the outer layer available to the carbonate may be gradually removed to reveal the same surface underneath. Alternatively, the surface available to the carbonate may be regenerated from oxidized sites deeper within the film. Regeneration could occur by direct transport of interstitial oxygen (U(VI) sites) towards the outer surface or by U(V) disproportionation followed by U(VI) transport. Intuitively, the two explanations can be distinguished based on whether the apparent dependence- of the amount of oxidized product remaining in the solid – on the rate of dissolution changes with the carbonate concentration or not. The reasoning here is that the dependence would not change in the first scenario, as the underlying surface that is gradually revealed is already set by the degree of oxidation irrespective of how fast the outer film is removed. On the other hand, if the outer layer is continuously regenerated from within the film, this process may at some point become rate limiting. As a result, a stronger dependence of the fraction of oxidized product remaining in the solid on the rate of dissolution is to be expected.

In Fig. 7.23, dissolution rates are shown as functions of the remaining fraction of oxidized product. This fraction is calculated as:

$$\theta = \frac{n_{final} - n_t}{n_{final}} \qquad (7.7)$$

where n_{final} is the total amount of dissolved UO_2^{2+} at depletion of the oxidized product and n_t is the amount of dissolved UO_2^{2+} at a given time of the exposure, t.

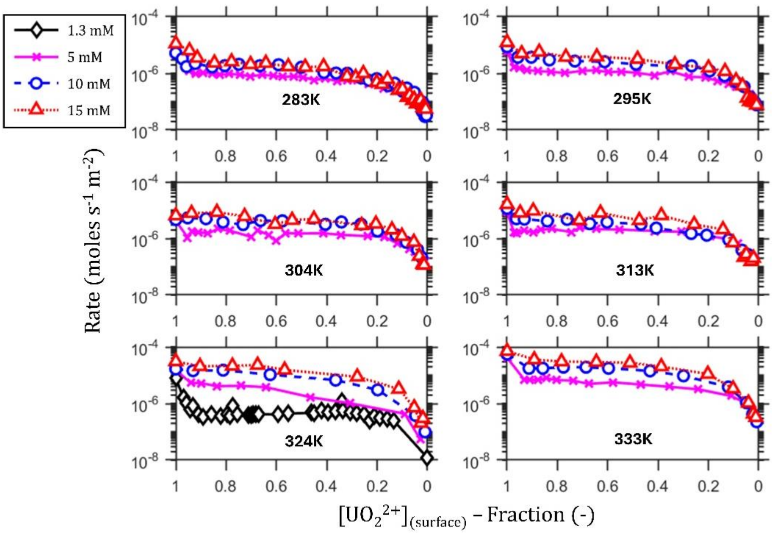

Fig. 7.23. Dissolutions rates as functions of the remaining fraction of oxidized product (goes from 1 – 0 during leaching) at various temperatures within the range 238 – 333 K.

In Fig. 7.23 an initial drop in the rate of dissolution appears in the early stage of dissolution. This is possibly due to a higher oxidation state of the outermost surface at the very start of the exposure. The dissolution then proceeds at a near constant rate until approximately 10 – 20 percent of the oxidized product remains, where are rapid drop in the rate occurs. There is no clear correlation between the carbonate concentration and the fraction at which the drop in the dissolution rate occurs, although the lowest concentration (1.3 mM) appears more flat than the other concentrations in the "fraction independent region" (0.9 – 0.1), this is the only indication of a carbonate effect on the remaining $UO_2^{2+}{}_{(surface)}$ – fraction dependence on the dissolution rate. Therefore, a clear distinction between the two possible explanations provided above cannot be made from this set of data.

The temperature dependence data for dissolution rates 5-, 10- and 15 mM $NaHCO_3$ is shown in Fig. 7.24, with rate vs T on a linear y-axis in (a) and log y-axis in (b), Arrhenius plot in (c) and apparent activation energies as functions of [$NaHCO_3$] in (d).

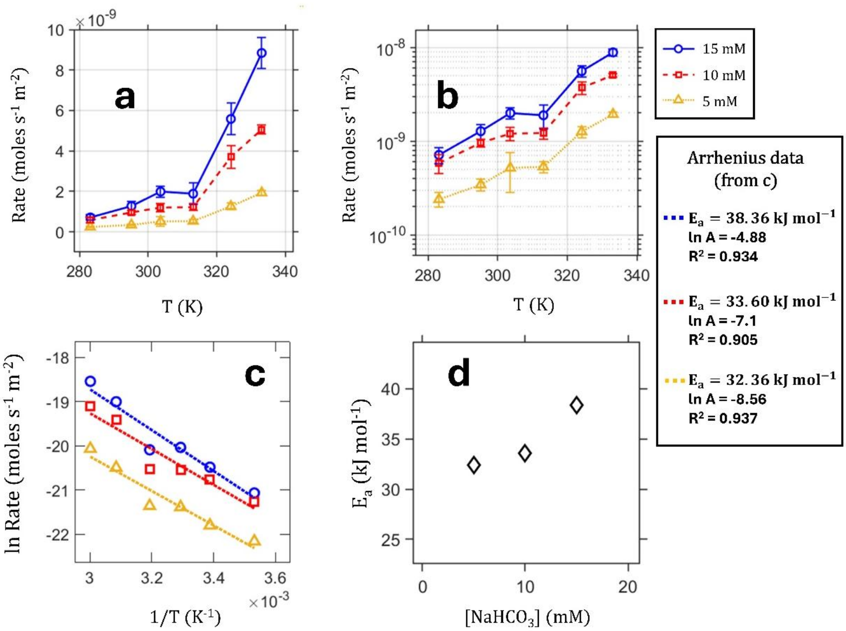

Fig 2.24. Temperature dependence data with dissolution rate as functions of temperature on linear y-axis in (a) and log y-axis in (b), Arrhenius plot (c) and apparent activation energies as functions of [NaHCO3] in (d).

As seen in Fig. 2.24 a-c, a deviation from the overall trend is observed at T = 313 K (1/T ~3.2×10^{-3}). This deviation appears as a temperature independence from (295 – 313) K whilst the overall temperature dependence follows the characteristic linear Arrhenius trends shown in Fig. 2.24 c. Taking the mean of the three slopes of Figure x c and inserting into the log form of the Arrhenius equation:

$$\ln k = -\frac{E_a}{R}\left(\frac{1}{T}\right) + \ln A \qquad (7.8)$$

Yields E_a = (34.8 ± 3.2) kJ mol^{-1}. This value overlaps with E_a = (35.7 ± 0.2) kJ mol^{-1} reported by de Pablo et al [92]. To further clarify the role of carbonate in the dissolution mechanism, the carbonate dependence, n, in the empirical rate law

$$r = k[HCO_3^-]^n \qquad (7.9)$$

has been investigated. In Fig. 7.25. a, n has been fitted by the log form of Eqn 7.9

$$\ln r = \ln k + n \ln [HCO_3^-]) \qquad (7.10)$$

The error bars of Fig. 7.25 a represents the standard error of the slope SE, mathematically determined as

$$SE = \frac{s}{\sqrt{S_{xx}}} \qquad (7.11)$$

with

$$s = \sqrt{\frac{RSS}{m-2}}, \quad RSS = \sum(y_i - \hat{y}_i)^2 \text{ and } S_{xx} = \sum(x_i - \hat{x})^2 \qquad (7.12)$$

where y_i represents the ln rate at concentration i, $\hat{y}_i$ the corresponding ln rate predicted by the linear regression, x_i the log concentration, $\hat{x}$ the mean ln concentration and m the number of observations (measured points).

In Fig. 7.25 b the carbonate dependence is instead shown separately for the three concentration regions 1 – 5 mM, 5 – 10 mM and 10 – 15 mM. n is then determined from

$$\frac{r_{i+1}}{r_i} = \left(\frac{C_{i+1}}{C_i}\right)^n \Rightarrow n = \frac{\ln\left(\frac{r_{i+1}}{r_i}\right)}{\ln\left(\frac{C_{i+1}}{C_i}\right)} \qquad (7.13)$$

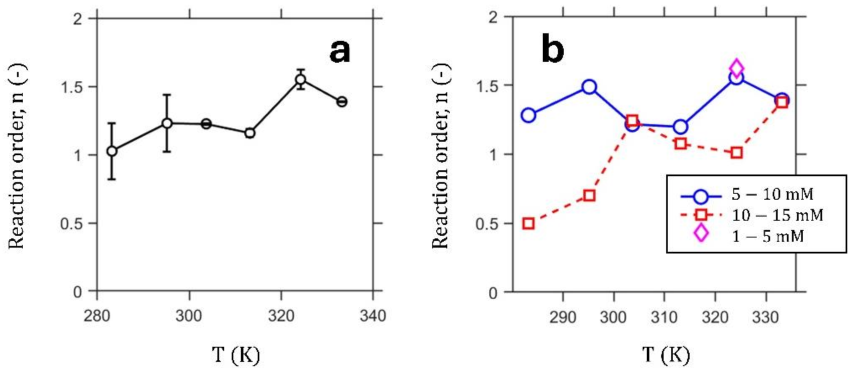

Fig 7.25. Carbonate dependencies on the rate determined by fitting of the ln rates vs bicarbonate concentrations over the full range (1)5 – 10 mM (a) and carbonate dependencies calculated for each step in bicarbonate concentration separately (b).

In Fig. 7.25 a, n appears to vary between 1 – 1.5. The standard error is significantly larger at the lower temperatures (10 – 22) °C. This is also reflected in Fig. 7.25 b where a lower carbonate dependence (0.5 – 0.7) is observed at the higher carbonate concentration range (10 – 15) mM compared to the lower carbonate concentration range (5 – 10) mM (with the carbonate dependence 1.3 – 1.5). The carbonate dependence appears to become more similar for the various concentration ranges as the temperature increases. This trend is consistent with a stronger adsorption expected at lower temperatures and indicate that the (10 – 15) mM carbonate range sits within the region where surface saturation affects the apparent reaction order. The lower concentration region (5 – 10) mM (and the (1 – 5) mM at 50°C) consistently show a carbonate dependence greater than 1. This is in line with the higher carbonate dependence reported by Schortmann and DeSesa [83], where the carbonate dependence was suggested to vary between 0 and 2. If the rate-limiting step of the dissolution is the coordination of the second carbonate by the insoluble complex $UO_2(CO_3)$, a carbonate dependence exceeding 1 can be explained by reversibility of the first carbonate attachment. The apparent reaction order could approach two at a temperature where $UO_2(CO_3)$ becomes short-lived to the point where the two carbonates must approach almost instantaneously for dissolution to occur.

7.4 ε-particle catalyzed vs non- catalyzed H_2-effect (on the inhibition of oxidative dissolution of UO_2)

It is well known that some of the metals formed through fission can catalyze H_2 induced reduction of $UO_{2.x}$ which counteracts the process of oxidative dissolution. This is sometimes referred to as the ε-particle catalyzed H_2 effect. Some recent studies have shown that H_2 may directly counter oxidative dissolution induced by H_2O_2 in the absence of ε-particles, supposedly by scavenging surface bound hydroxyl radicals [141-144]. In this section, the role of H_2 in countering the surface oxidation is studied in presence and absence of Pd doping (used as a proxy for ε-particles). The oxidation is expected to mainly be induced by $HO^•$, generated with an electron cyclotron resonance (ECR) plasma source, a more detailed description of the experimental setup is provided in section 6.3.3. The excitation and ionization of H_2O molecules in the vapor leads to dissociation and formation of radical- and molecular products, including $HO^•$, $H^•$, $HO_2^•$, O, O_2, H_2 and H_2O_2 [145]. Due to the relatively low kinetic energy of the electrons obtained in the ECR, water dissociation is expected to mainly occur through excitation. The two modes of dissociation are $H_2O^* \rightsquigarrow$; (I) $H^• +$ $HO^•$ and (II) H_2 + O, with 87 percent of the dissociation occurring through (I)

[146]. Due to the low pressure of the water vapor (~ 10^{-6} mbar), the probability of radical recombination is low. This means that most of the oxidation is expected to be caused by direct exposure to $HO^{\bullet}$.

Stoichiometric UO_2 thin films with an approximate thickness of 20 nm were deposited on Au substrates by Ar-sputter deposition under Ar/O_2 mixed atmosphere. The films were exposed to H_2O-plasma to generate $HO^{\bullet}$. An elevated temperature of 400°C was used to prevent diffusion limitations. Oxidation was traced by analysis of the core level features in XPS as well as valence band features in XPS and UPS. The average charge of the uranium atoms U^{x+} was calculated based on the change in the ratio of U5f to U4f signal (method 1), by deconvolution of the U4f 7/2 peak into the three components U^{4+}, U^{5+} and U^{6+} (method 2) and qualitatively compared to the characteristic energy separation between U4f 7/2 and its shakeup satellite (method 3, 6.9 eV for U^{4+}, 7.9 eV for U^{5+} and 9.7 eV for U^{6+}) [79]. The relative oxygen atom concentration (UO_y) was calculated from the change in ratio of the O1s to U4f signal (method 4).

7.4.1 H_2O plasma exposure of undoped UO_2 at 400°C

An undoped UO_2 film, heated to 400°C was kept under H_2O plasma for 5 minutes. The surface was continuously flushed with H_2 through the gas inlet. The H_2 gas pressure as high as could be sustained without overloading the vacuum pump (8×10^{-5} mbar). Data related to the calculations of oxidation state U^x and oxygen atom concentration UO_y, recorded before and after the exposure are provided in Table 7.2.

Table 7.2. XPS data obtained for an undoped UO_2 thin film after 5 min H_2O plasma exposure at 400°C with constant flushing of the surface with H_2.

Treatment	U5f/U4f	Main peak-Satellite separation ΔE (eV)	O1s/U4f	U(x) (methods 1, 2, 3)	UO_y (method 4)
Before exposure	0.0462	6.9	0.205	4.0 (ref)	2.0 (ref)
After exposure	0,0249	7.9	0.317	4.9, 4.9, 5.0	3.1

The core levels U4f and O1s are shown before and after 5 minutes exposure under H_2O plasma in Fig. 7.26 followed by the corresponding valence band features (recorded with He II UPS and XPS) in Fig. 7.27. and the deconvoluted U4f 7/2 in Fig. 7.28.

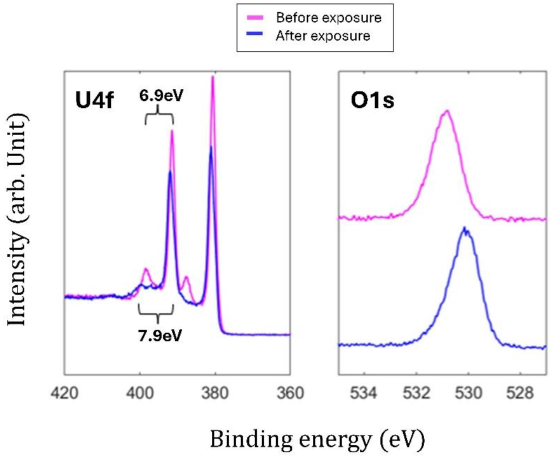

Fig. 7.26. XPS spectra showing features of the U4f and O1s regions before and after exposure, recorded pre-exposure (magenta) and after 5 minutes under water plasma at 400ºC with continuous flushing with H_2 (blue). The intensities of O1s are intensity-normalized.

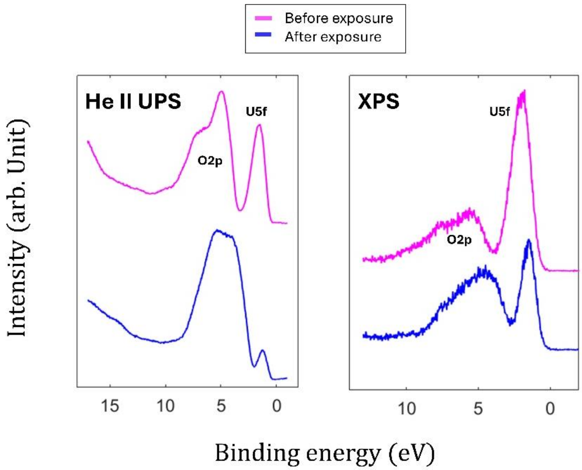

Fig. 7.27. He II UPS- and XPS spectra showing features of the valence band region, recorded pre-exposure (magenta) and after 5 minutes under water plasma at 400ºC with continuous flushing with H_2 (blue). The intensities of the valence bands are intensity-normalized with respect to O2p.

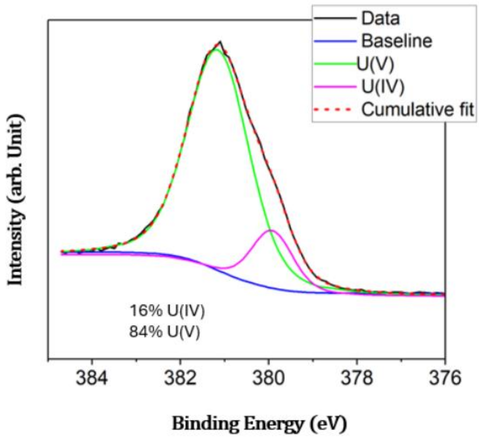

Fig. 7.28. Deconvoluted U4f 7/2 peak recorded after 5 minutes under water plasma at 400°C with continuous flushing with H_2.

The exposure resulted in significant oxidation as seen by the decrease in U5f signal, increased O1s signal relative to the U4f and the higher energy separation between the U4f 7/2 main peak and the shake-up satellite. The calculated average uranium charge U^{x+} is 4.9 for method 1 and 4.8 for method 2 (16% U^{4+} and 84% U^{5+}). This is in line with the 7.9eV separation of the shake-up satellite which is characteristic for U^{5+}. The oxygen atom concentration, calculated based on the change in the O1s to U4f ratio, suggests 3 O per 1 U. This would require charge compensation by H^+ and the structure is therefore likely UO_2OH. The degree of oxidation is in line with what was observed by El. Jamal et al after 5 min exposure under H_2O plasma at 400°C without flushing with H_2 [76]. The uncatalyzed H_2 effect must therefore be negligible under these conditions.

7.4.2 H_2O plasma exposure of Pd doped UO_x at 400°C

A second UO_2 film was doped with 15 percent Pd (as determined by the ratio of Pd3d to U4f) by vapor deposition using the procedure by Stumpf et al. The procedure produces spherical Pd particles of the size 1 – 3 µm (ε-particles) which are formed through agglomeration of smaller spheres (0.3 – 1 µm) [133]. The doped film was consecutively exposed to H_2O plasma at 400°C for 5 min. The H_2 pressure was gradually lowered for each new exposure. The core levels and valence band features recorded after each exposure are presented in Fig. 7.29 and Fig. 7.30 respectively.

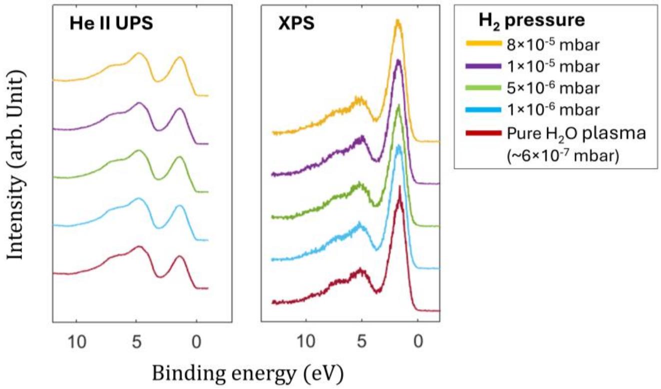

Fig. 7.29. He II UPS- and XPS spectra showing features of the valence band region recorded after consecutive 5-minute exposure to water plasma at 400°C with continuous flushing with H_2. The H_2 pressure was gradually lowered for each consecutive exposure and turned off for the final exposure. The intensities are normalized with respect to O2p.

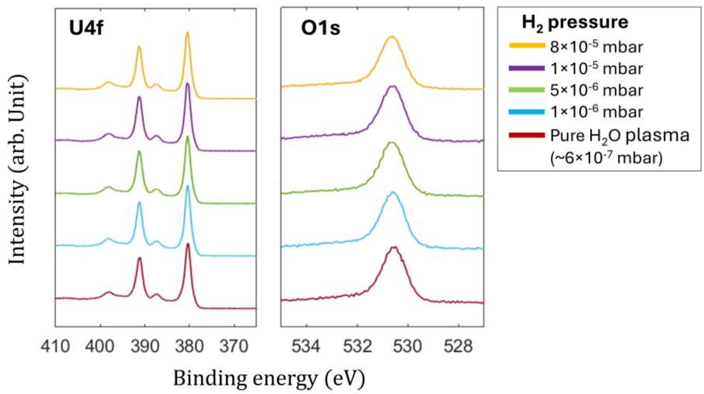

Fig. 7.30. XPS spectra showing features of the U4f and O1s core-level region recorded after consecutive 5-minute exposure to water plasma at 400°C with continuous flushing with H_2. The H_2 pressure was gradually lowered for each consecutive exposure and turned off for the final exposure. The intensities of O1s are intensity-normalized.

As is clear by the lack of change in the valence band features as well as the preservation of the characteristically sharp shake-up satellite with a 6.9 eV energy gap from the main U4f signal, the ε-particles effectively prevent oxidation of the UO_2 film even in the absence of H_2 other than what is formed by the recombination of H• in the H_2O plasma. This was confirmed by performing the same Pd doping of a fully oxidized UO_3 film which was exposed to H_2O plasma at 400°C for 5 min. The core level features recorded before Pd doping, after Pd doping prior to exposure, and after 5 min water plasma exposure shown in Fig. 7.31, followed by the corresponding valence band features in Fig. 7.32.

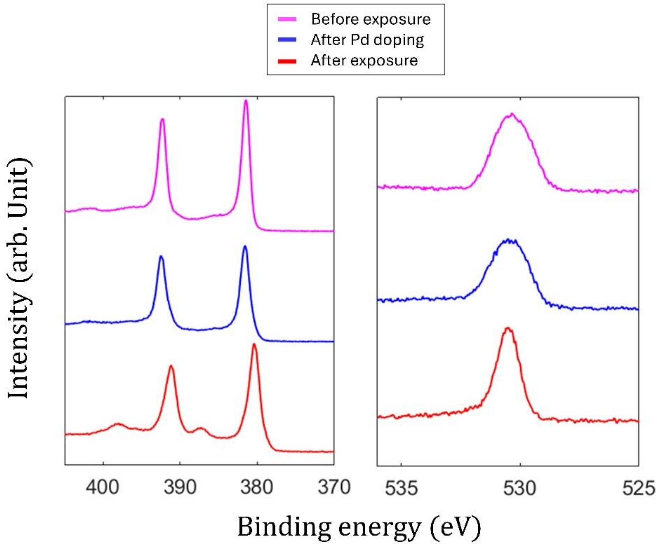

Fig. 7.31. XPS spectra showing features of the U4f and O1s core-level region recorded for an undoped UO_3 film, the same film after Pd deposition, and after 5 minutes of exposure under water plasma at 400°C. The O1s signals are intensity-normalized.

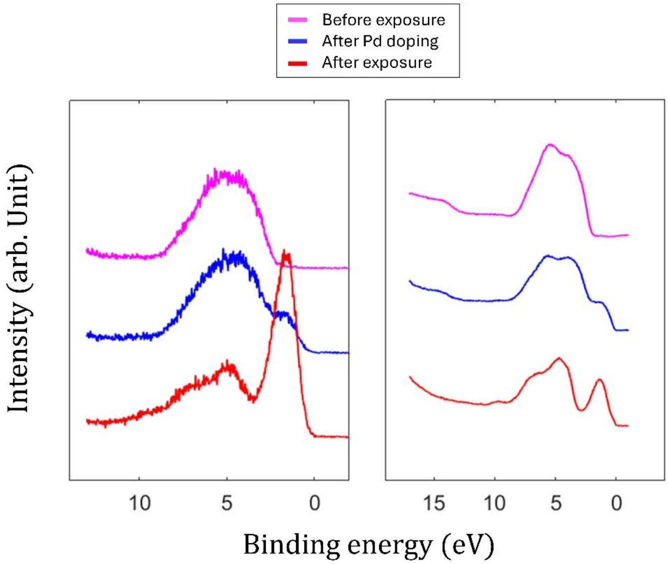

Fig. 7.32. He-II UPS and XPS spectra showing features of valence band region recorded for an undoped UO_3 film, the same film after Pd deposition, and after 5 minutes of exposure under water plasma at 400°C. The intensities are normalized with respect to O2p.

It is clear from both the appearance of the U5f signal and the narrowing of the energy gap for the U4f main peak and the shake-up satellite that the UO_3 film reduces to UO_2 during the 5 min H_2O plasma exposure. The H_2 generated through combination of H• must therefore be sufficient to shift the plasma condition from oxidizing to reducing for the Pd doped film. This is clearly not the case for the undoped which was observed to oxidize to near pure U(V) for the same duration under the plasma (Table 3) and has been reported to oxidize further ~ UO_3, during 10 minutes of continuous exposure [76].

7.4.3 H_2O plasma exposure of Pd doped UO_x at room temperature

To investigate the effect of temperature on the ε-particle catalyzed H_2 effect, a UO_2 film doped with 15 percent Pd was exposed for 5 min under H_2O plasma at room temperature. The valence band- and core level features (recorded before and after Pd deposition and after the plasma exposure of the doped film) are shown in Fig 7.33. The deconvoluted U4f 7/2 peak recorded after the plasma exposure of the Pd doped film is shown in Fig 7.34.

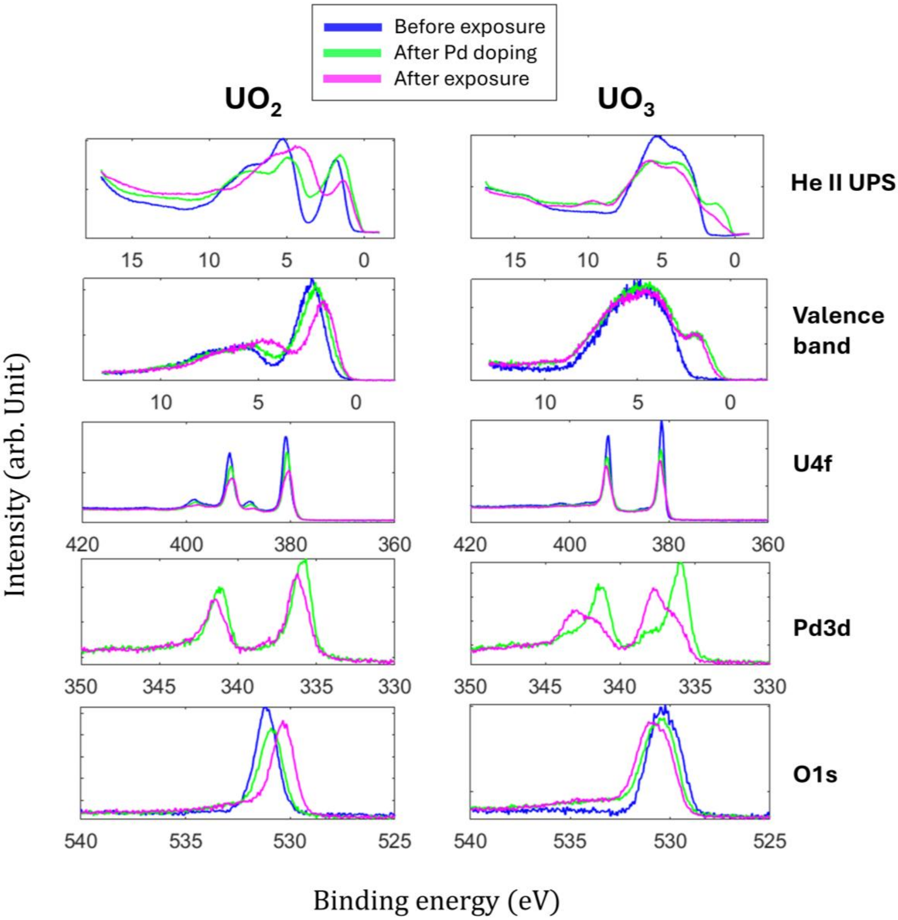

Fig. 7.33. He-II UPS and XPS spectra showing features of valence band region, and XPS spectra of the U4f, Pd3d and O1s core-level regions recorded for undoped UO_3 and UO_2 films, the same films after Pd deposition, and after 5 minutes of exposure under water plasma at room temperature (~298 K).

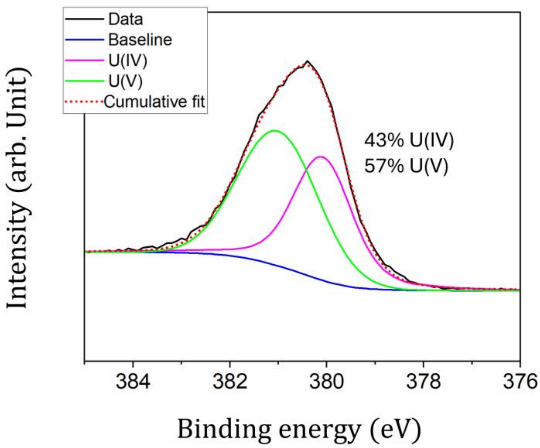

Fig. 7.34. Deconvoluted U4f 7/2 peak recorded for a Pd doped UO_2 thin film after 5 minutes under water plasma at room temperature (~298 K).

As is clear from the valence band features (He II UPS and XPS) in Fig. 7.33, The doping of the film with Pd results gives rise to a signal that overlaps with the U5f and O2p. This is attributed to the Pd4d valence electrons [147]. Due to this overlap, the oxidation state of the uranium cannot be determined by the change in ratio of U5f to U4d. The Pd doping also appears to induce asymmetry in the O1s peak, complicating the determination of oxygen concentration by comparison of O1s to U4f. It is clear however that oxidation occurs for the UO_2 film, based on the partial disappearance of the U4f shake-up satellite. Deconvolution of the U4f peak for the doped UO_2 film after the exposure (Fig. 7.34) resulted in the calculated average uranium charge $U^{4.57+}$ (43% U^{4+} and 57% U^{5+}). Splitting of the Pd3d 5/2 and 3/2 is noticeable for the doped UO_3 film before exposure. This splitting is characteristic for a mixture of Pd^0 and $Pd^{II}O$ [148], suggesting that some of the lattice/interstitial oxygen in the UO_3 film are coordinated by Pd. For the UO_3 film, the PdO signal outweighs the Pd^0 signal after the plasma exposure. This is crucial information as it shows that the catalytic effect is thermally activated whilst inactivation could occur when Pd is unable to sustain its own reduction. For the Pd doped UO_2 film, the splitting of the Pd3d is noticeable after the plasma exposure but most of the Pd3d signal still comes from Pd^0. This indicates that O atoms sitting in the oxide film are at equilibrium with O atoms sitting in ε-particles. This would explain why ε-particles formed in the UO_3 (oxygen saturated film) oxidized significantly more than the ones in the UO_2 film during exposure under the same conditions.

The efficiency of the ε-particle catalyzed H_2 effect at room temperature was further investigated by consecutive exposures of a Pd doped UO_3 film at various H_2 pressures. The core level features, valence band features and deconvoluted U4f peaks are shown in Fig. 7.35, Fig. 7.36 and Fig. 7.37 respectively.

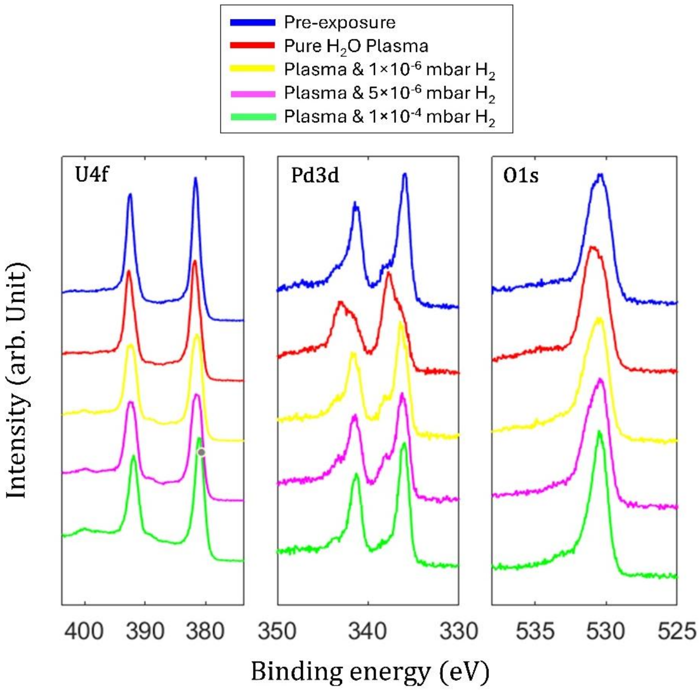

Fig. 7.35. XPS spectra showing features of the U4f, Pd3d and O1s core-level region recorded for a Pd doped film after consecutive 5-minute exposures to water plasma at room temperature (~298K) with continuous flushing with H_2. The H_2 pressure was gradually raised for each consecutive exposure. The O1s signals are intensity-normalized.

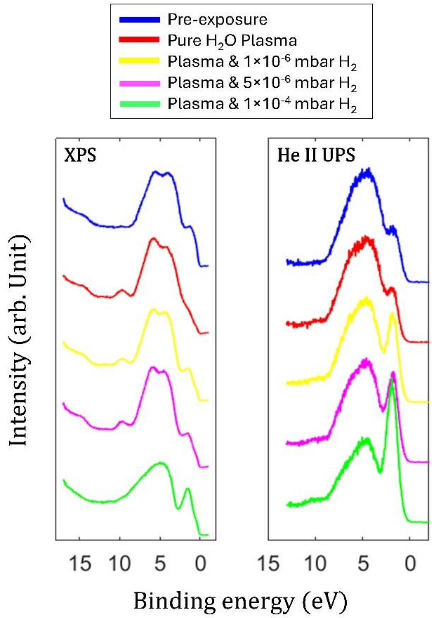

Fig 7.36. He-II and XPS spectra showing features of the valence band region recorded after consecutive 5-minute exposures of a Pd doped film to water plasma at room temperature (~298K) with continuous flushing with H_2. The H_2 pressure was gradually raised for each consecutive exposure. The intensities are normalized with respect to O2p.

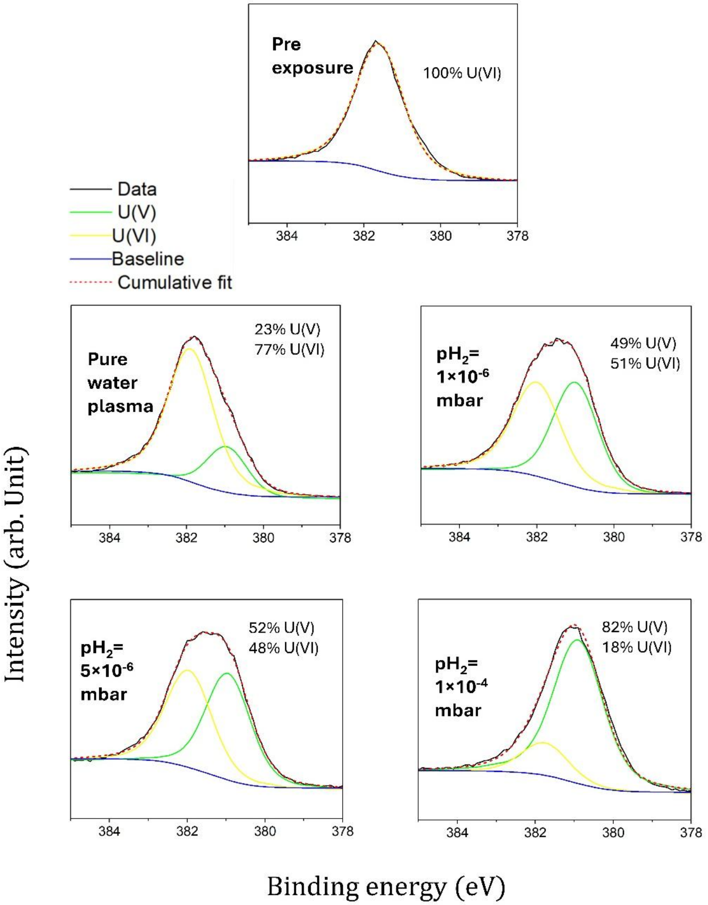

Fig. 7.37. Deconvoluted U4f 7/2 peaks after consecutive 5-minute exposures of a Pd doped film to water plasma at room temperature (~298K) with continuous flushing with H_2. The H_2 pressure was gradually raised for each consecutive exposure.

The ε-particle are again observed to undergo oxidation under the pure H_2O plasma (observed by the higher shifted Pd3d signal from PdO). The consecutive exposures with H_2 purging show that the U^{6+} are gradually reduced to U^{5+} with no indication of further reduction of U^{5+} to U^{4+}. Although the presence of PdO is noticeable, the Pd3d signal is mainly Pd^0 already at $1{\times}10^{-6}$ mbar H_2. Despite this activation, the reduction appears to stop at a pure U^{5+} film even as the H_2 pressure is increased by two orders of magnitude as seen by the deconvolutions in Fig. 7.37. As the H_2 supply is constant, this likely means that the film forms a pure UO_2OH film, whilst further supply of H• (via Pd catalyzed splitting of H_2) binds reversibly and eventually recombine to form H_2. A stable U(V) intermediate is in line with previous observations that the UO_2 was oxidized to near pure U(V) during 11 days of α-irradiation (3.30 MBq, ^{241}Am) [149].

A broadening of the O2p is visible in the He II UPS spectrum of Fig 7.36. This broadening is uncharacteristic for UO_x. The Pd3d peak area relative to the initial area (pre-exposure) is shown in Fig. 7.38.

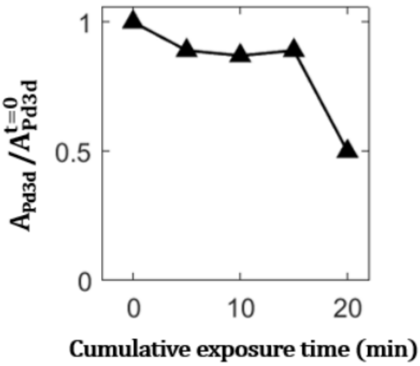

Fig 7.38. Change in Pd3d : initial Pd3d signal ratio as function of cumulative time under water plasma at room temperature.

Clearly the broadening is accompanied by a significant change in the Pd3d signal, recorded after the last exposure. A possible explanation for this loss is that radiolytic oxidants, H_2 or a combination of two induces embrittlement of Pd/PdO, leading to disintegration of ε-particles to form a $U_xPd_yO_z$ alloy.

7.4.4 Reversibility of the thermal activation/deactivation of the ε-particle catalyzed H_2 effect

A Pd doped UO_2 film was consecutively exposed to H_2O plasma while alternating between low temperature (25°C) and high temperature (400°C). Core level- and valence band spectra recorded after film deposition, after pd doping and after each consecutive exposure are shown in Fig. 7.39, followed by core-level spectra in Fig. 7.40.

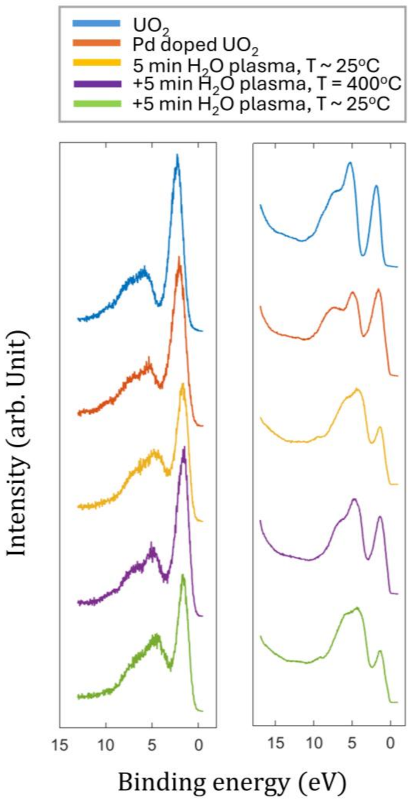

Fig. 7.39. XPS and He II-UPS spectra showing the valence band region recorded after consecutive 5-minute exposures of a Pd doped film to water plasma, with temperature alternated between low (~25°C, oxidizing) and high (400°C, reducing). The intensities are normalized with respect to O2p.

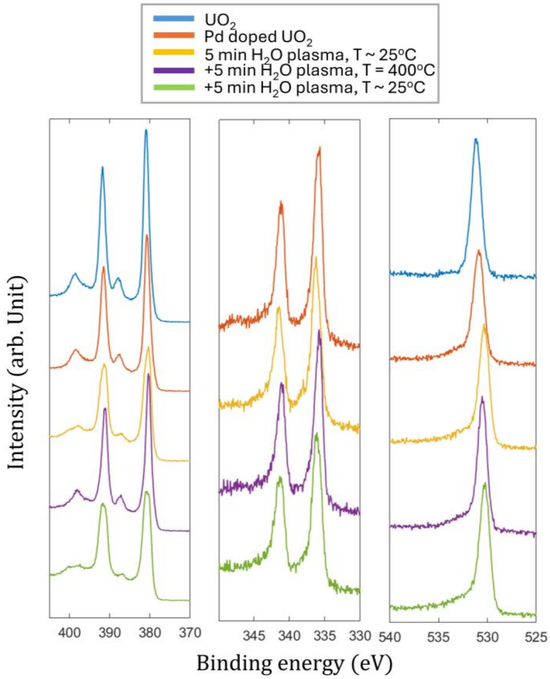

Fig. 7.40. XPS spectra showing U4f, Pd3d and O1s core-level regions recorded after consecutive 5-minute exposures of a Pd doped film to water plasma, with temperature alternated between low (~25°C, oxidizing) and high (400°C, reducing). The O1s peaks are intensity-normalized.

Clearly, there is a reduction in the U5f signal after each exposure at room temperature. The U5f signal intensified during the high temperature exposure, confirming that the ε-particle catalyzed reduction is reversibly activated/inactivated by temperature variation.

To evaluate the efficiency of catalyzed H_2 effect as a function of temperature, a Pd doped UO_2 film was consecutively exposed to water plasma. The temperature was altered as follows:

- 5 min at 25°C
- 5 min at 400°C
- 5 min at 100°C
- 5 min at 400°C
- 5 min at 200°C

Deconvolutions of the U4f peaks after exposure are shown for each temperature in Fig. 7.41.

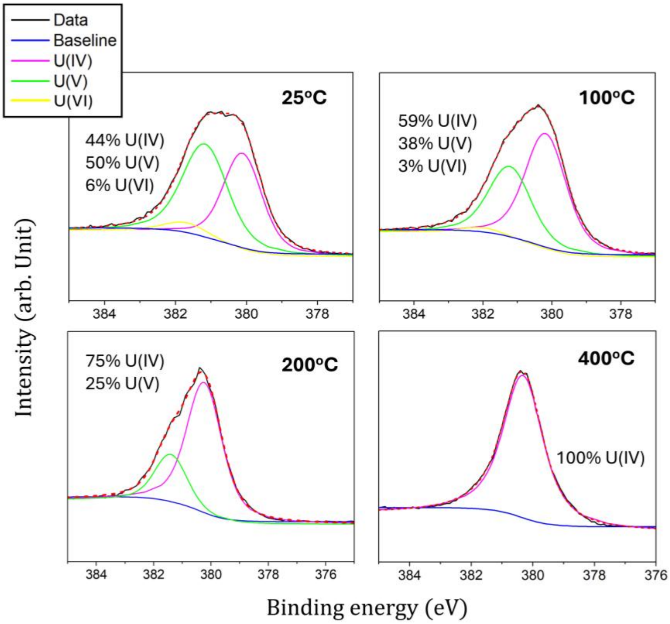

Fig. 7.41. Deconvoluted U4f 7/2 peaks, recorded after consecutive 5-minute exposures of a Pd doped film, to water plasma at four different temperatures within the range 25 – 400°C.

As shown in Figure 7.41, the degree of oxidation decreases with temperature. The Pd is ineffective at countering the formation of U^{5+} at temperatures < 200°C yet little (if any) U^{6+} forms. At 200°C, most of the uranium remains U^{4+} and at 400°C oxidation can no longer be observed.

The interpretation of the observed temperature effect will further be discussed in terms of the following proposed mechanism:

$$\mathrm{UO_2 + OH \rightarrow UO_2OH} \quad (7.14)$$

$$\mathrm{UO_2OH + OH \rightarrow UO_3 + H_2O} \quad (7.15)$$

$$\mathrm{UO_3 + H \rightarrow UO_2OH} \quad (7.16)$$

$$\mathrm{UO_2OH + H \rightarrow UO_2 + H_2O} \quad (7.17)$$

$$\mathrm{H + H \rightarrow H_2} \quad (7.18)$$

At lower temperature, the plasma induced oxidation of U^{4+} (UO_2) into U^{5+} without further conversion of U^{5+} into U^{6+} suggests formation of a persistent intermediate (likely UO_2OH). The intermediate also appears stable during the low temperature exposure of UO_3, where U^{6+} is at least partially reduced to U^{5+} without further reduction of U^{5+} into U^{4+}. The fact that the first reduction reaction is observed shows that Pd is at least partly effective in converting H_2 into H• (i.e. not fully inactivated). The second reduction-step must therefore be thermally activated or effectively countered by the first oxidation (i.e. $r_{7.14} >> r_{7.17}$ at low temperature). The observation that reduction via bombardment with H• (H_2-plasma) also yields pure U(V) (see deconvoluted U4f 7/2 in Fig. 7.45) supports the former idea (inactivation or reversibility of reaction 7.17). Similarly, the second oxidation must either be inactive or effectively countered by the first reduction (i.e. $r_{7.16} >> r_{7.15}$).

A potential change in the composition of the Pd particles were noted during consecutive plasma exposures. In Fig. 7.42, the evolution of the U4f and Pd3d signals over consecutive exposures are shown.

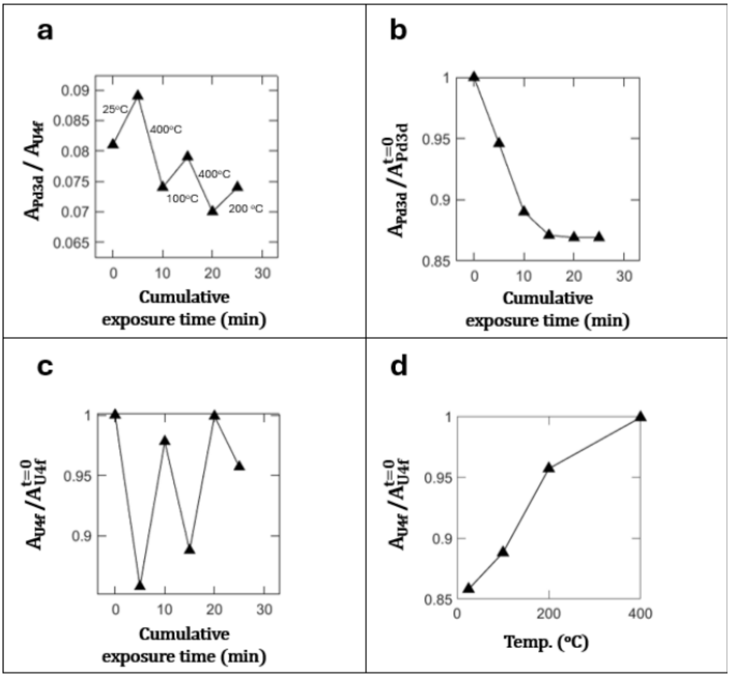

Fig. 7.42. The Pd3d : U4f- (a), Pd3d : initial Pd3d- (b), U4f : initial U4f- (c) signal ratios as functions of cumulative exposure time, and U4f: initial U4f signal ratio as function of temperature.

In Fig. 7.42 c the U4f signal is shown to alternate with alternating temperature as expected based on the lower density of U atoms at higher oxidation states, resulting in a lower signal at lower temperatures. The Pd3d signal on the other hand displays no dependence on temperature but appears to decrease with cumulative time under the plasma. Although the catalytic effect has been shown to reversibly activate/deactivate by temperature variation, a gradual loss of catalytic function is plausible if continuous oxidation and reduction of Pd^{0}/PdO leads to disintegration of the surface-near ε-particles over time. This idea was further investigated by fully oxidizing a Pd doped UO_2 film.

7.4.5 Stability of (near-surface) ε-particles under extreme oxidizing conditions

The Pd doped UO_2 film was fully oxidized by 15 min exposure to O_2-plasma at 400°C. The full oxidation was confirmed by the absence of U5f signal as well as by the sharp features of the Pd3d which shifted to higher energies relative to Pd^{0} indicating formation of pure PdO. The oxidized film was consecutively exposed to H_2O-plasma at 400°C. The valence band- and core level features are shown in Fig. 7.43 and 7.44 respectively.

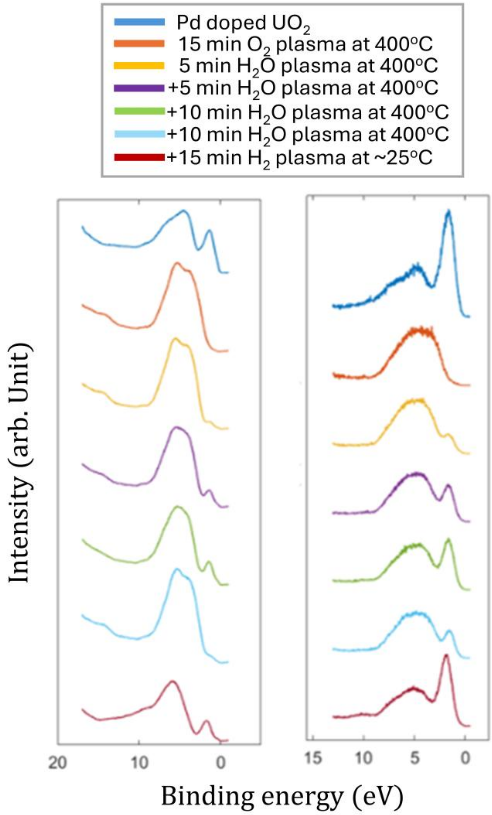

Fig. 7.43. He II UPS and XPS spectra showing the valence band features, and XPS spectra of the core-level regions recorded for consecutive exposures to water plasma at 400°C (reducing) after full oxidation of a Pd doped UO_2 thin film under O_2 plasma. The intensities are normalized with respect to O2p.

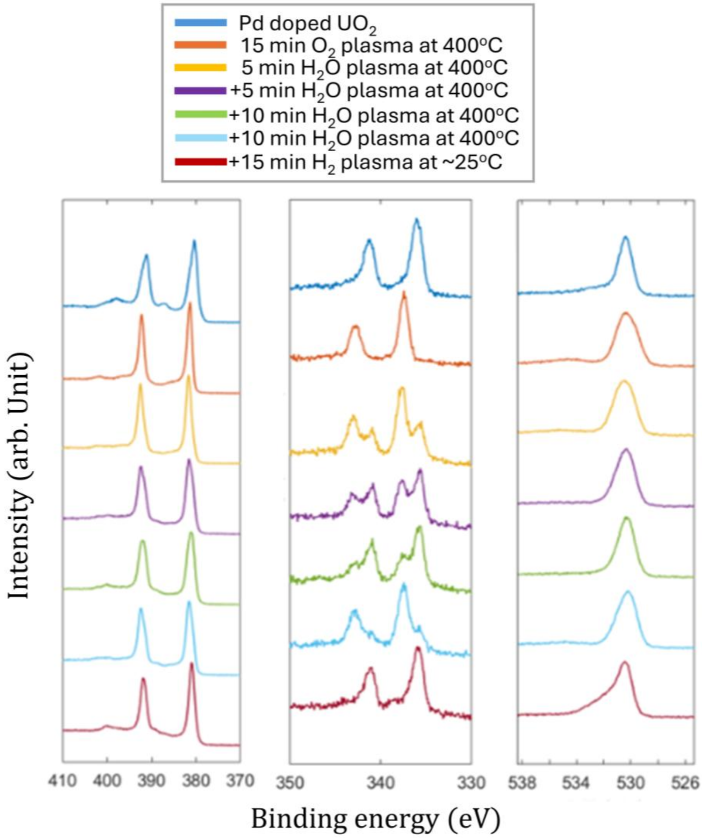

Fig. 7.44. XPS spectra showing U4f, Pd3d and O1s core-level regions recorded for consecutive exposures to water plasma at 400°C (reducing) after full oxidation of a Pd doped UO_2 thin film under O_2 plasma. O1s signals are intensity-normalized.

The first two H_2O-plasma exposures are observed to result in a partial reduction of PdO into Pd^0 as is evident by the splitting of the Pd3d. A minor reduction of UO_3 is also noticeable by the appearance of a small U5f signal. Upon further exposure however, the film re-oxidizes along with oxidation of the Pd^0 back into PdO. Lastly, a forced reduction of the film was induced by exposure under H_2-plasma. This resulted in a near full reduction of the PdO and the film appears to be at or near pure U^{5+} (based on the shape of the valence band and the characteristic 7.9 eV shift of the U4f shake-up satellite). This is an interesting observation as the H_2 plasma directly exposed the film to H• without the need for a catalyst. It further indicates that the inactivation of the catalytic effect is related to an inability of H• to reduce UO_2OH further into UO_2 at lower temperatures, not by the inability of Pd to split H_2. Excess H• (after the film has reached pure UO_2OH) likely recombines to form H_2. Another important observation is the distortion of the valence band and O1s features after the H_2-plasma. This is likely the result of the formation of a U/Pd/O alloy from ε-particle disintegration after being fully oxidized. This would explain the significant loss of catalytic function after the full oxidation under O_2-plasma. The gradual loss of Pd3d signal as a function of cumulative exposure time under H_2O plasma at 400°C is shown in Fig. 7.45.

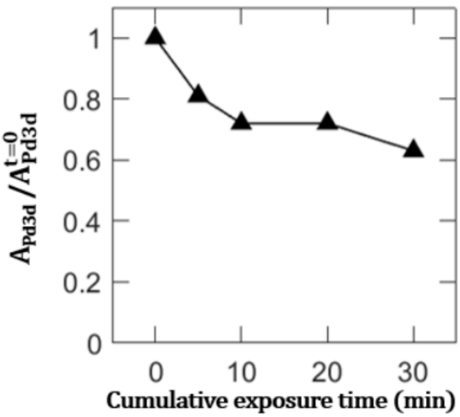

Fig. 7.45. The Pd3d : initial Pd3d signal ratio as function of cumulative exposure time.

The gradual loss of Pd3d signal clearly occurs faster after the full oxidation of the ε-particles (compared to Fig. 7.42 b).

The oxidation state of the film after the final reduction with H_2 appears to be at or near pure U(V) (likely UO_2OH) based on the deconvolution of the U4f 7/2 shown in Fig. 7.46.

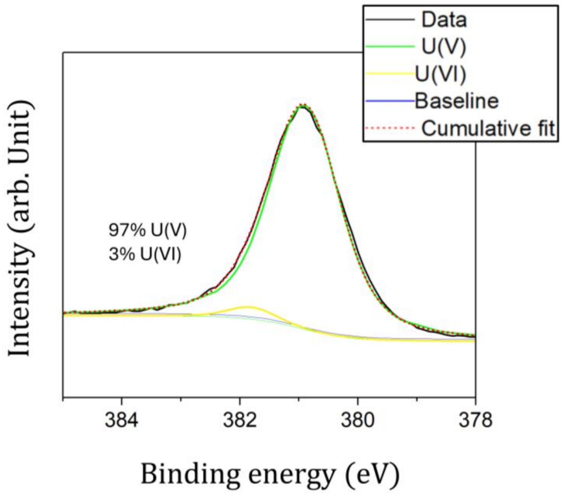

Fig. 7.46. Deconvolution of the U4f 7/2 peak after 15 minutes under H_2-plasma at room temperature (~298K).

The oxidation state after H_2-plasma exposure resembles that observed in Fig. 7.37 for a Pd doped film exposed to H_2O-plasma with simultaneous flushing of the surface with H_2 at room temperature. The difference here is that the catalytic property of Pd is bypassed by directly introducing H• through the plasma. The reason for the absence of U(VI) at room temperature therefore cannot be attributed to an inactivity of the Pd but must be due to inactivation or reversibility of the second reduction step (reaction 7.17) with excess H• likely reforming H_2 through recombination within the film. This observation is in contrast with several earlier reports [68, 141, 148] of a reaction between H_2 and the surface bound hydroxyl radical (formed via splitting of H_2O_2 on UO_2). If the semi-stable U(V) intermediate is indeed UO_2OH as indicated by the charge of the uranium together with the 3:1 O : U ratio (see Table 3), it is hard to see why this intermediate would be scavenged by H_2 but not by H•. One possibility is the different lattice structure of the solid on which they form. The reduction of UO_3 by H_2-plasma has been shown to yield a pure U(V)-film [79]. The surface bound hydroxyl radical formed upon splitting of H_2O_2 on UO_2 (U(IV)O_2OH) could react with H_2 through a mechanism that does not require a rearrangement of the lattice geometry. On the other hand, the further reduction of U(V)O_2OH into U(IV)O_2 (+H_2O) would induce significant lattice contraction. If the energy barrier of the reduction is set by the rearrangement of the lattice rather than the reaction between the $H_2/H^\bullet$ and $U(V)O_2OH$ this could potentially explain the thermal activation of the secondary reduction of U(V) into U(IV). Another possibility is that the further reduction of U(V) at ambient temperature relies on the presence of an aqueous phase. The observation of a semi-stable U(V) is however consistent with XPS observations for UO_2 in irradiated aqueous solutions [55, 56]. The slow dissolution rate for this intermediate in 10 mM bicarbonate solutions [56] brings into question whether ε-particles inhibit dissolution through full reduction of soluble U(VI) into U(IV) or through partial reduction to U(V).

8 Conclusions

This thesis covers several aspects related to radiation-induced oxidative dissolution of UO_2-based spent nuclear fuel. The impact of μ-η^2:η^2-peroxo coordination on both the reactivity of peroxide towards UO_2 and the stability of peroxide in irradiated solutions was studied. Our results show that H_2O_2 is the reactive form and the shift in equilibria towards μ-η^2:η^2-peroxo complexes suppresses the rate of H_2O_2 induced oxidative dissolution. The presence of uranyl ions affects the stability of peroxide in several ways. On one hand, UO_2^{2+} can suppress the buildup of peroxide the presence of O_2 at $[UO_2^{2+}] \geq 100$ µM. This is proposed to occur via a UO_2^{2+}-catalyzed Haber-Weiss type chain reaction between superoxide and μ-η^2:η^2-peroxo complexes. On the other hand, UO_2^{2+} can act as a scavenger of reducing radicals (e^-_{aq} and $H^\bullet$) in the absence of O_2 which increases the peroxide steady-state concentration compared to UO_2^{2+}-free solutions under inert (N_2) atmosphere.

An experimental approach for studying the process of carbonate facilitated dissolution of oxidized UO_2 in the absence of the oxidation process was employed to determine the effects of temperature-, carbonate- and the degree of oxidation of the uranium oxide – on the dissolution kinetics. The carbonate concentration dependence was found to decrease with bicarbonate concentration within the concentration range 1.3 – 15 mM at temperatures ≤ 295K, indicating surface saturation at higher concentrations 10 – 15 mM. Reaction orders ($r = [HCO_3^-]^n$) were found to vary within the range $0.5 \leq n \leq 1.5$ for the temperature range 283 – 333 K and [HCO_3^-] range 1.3 – 15 mM. The observations clarify the inconsistencies between earlier reports, where a concentration dependence ≤ 1 is typically observed for concentrations ≥ 5 mM and concentration dependencies ≥ 1 is observed for concentrations ≤ 5 mM. The activation energy was determined as (34.8 ± 3.2) kJ mol^{-1} which overlaps with the value (35.7 ± 0.2) kJ mol^{-1} reported by de Pablo et al. [92]. A high rate of dissolution was observed for an initial fraction (~ 10 percent of the oxidized product) upon exposure to HCO_3^-. A slower dissolution proceeded at a rate near independent of the change in the fraction of oxidized product remaining in the solid, indicating that the surface available to the carbonate remains the same throughout this stage. As the fraction of remaining oxidized products falls below ~20 percent, the rate of dissolution rapidly decreases, marking a change in the rate determining step (or a change of the reactive surface) as the oxidized product nears depletion.

Studies of Pd doped and undoped UO_2 and UO_3 films were carried out during H_2O-plasma exposures with simultaneous flushing of the surface with H_2. The aim was to elucidate the relative contribution of two hydrogen effects: (1) Pd-catalyzed reduction and (2) a potential reaction between the surface bound hydroxyl radical and H_2. No suppression of the oxidation induced by the plasma at 400°C could be observed for the undoped film, under H_2-pressures as high as could be maintained with the experimental setup (1×10^{-4} mbar). For a doped film with a 15 percent Pd : U atom ratio at the same temperature, the H_2 generated through recombination of $H^\bullet$ in the H_2O plasma (~ 6×10^{-7} mbar) was sufficient to keep the film fully reduced (UO_2). At room temperature, only partial reduction to a pure U(V) intermediate was observed, with no indication of further reduction to U(IV) (or further oxidation to U(VI).

9 Future perspective

Several observations presented in this thesis raise new questions related to the evolution of a failed repository. The observation that UO_2^{2+} can inhibit the reactivity of peroxide towards the fuel matrix by suppressing the fraction of reactive H_2O_2, whilst simultaneously enabling peroxide buildup under anoxic conditions should be further explored by investigating the influence of UO_2^{2+} on the rate of spent nuclear fuel dissolution directly.

A straightforward approach to study the dissolution of UO_2 in the absence of oxidation is presented. This opens for further research where the kinetics of dissolution promoted by other ligands present in groundwater (such as PO_4^{3-} and $C_2O_4^{2-}$) can be assessed.

Lastly, the role of the semi-stable U(V) intermediate has yet to be understood. As determined by comparison of the O : U ratio as well as the average charge of the U atoms, this intermediate is more likely UO_2OH than the U_2O_5 reported in previous works. As no surface analysis was included in earlier studies of the leaching of Pd doped UO_2 it is not clear whether a partial reduction of U(VI) into U(V) (rather than full reduction into U(VI)) can account for the observed inhibition of oxidative dissolution of Pd doped UO_2 in the presence of H_2.

10 Disclosure of Gen AI use

The work presented in this thesis, including its structure and language, is the author's original work. Use of generative artificial intelligence (Gen AI) in connection with the work is limited to OpenAI ChatGPT (GPT-5).

The author's disclosure regarding the nature and limitations of its use is specified below:

- Scientific content – The discussion, interpretation of data, and conclusions presented in this thesis originate entirely from the author and have not been revised or altered by Gen AI.
- Gen AI assistance – Gen AI use is limited to chapters 3, 4 and 7. The use included the following:
  - Identification of scientifically inaccurate statements and potential misinterpretations made by the author related to XPS theory and thermodynamics (chapters 3 and 4).
  - To suggest further reading related to any scientifically inaccurate statement made by the author (chapters 3 and 4).
  - To improve the readability of figures through AI-suggested changes to the formatting of MATLAB plots (chapter 7).

References

(1) International Atomic Energy Agency (IAEA), ”Survey of Wet and Dry Spent Fuel Storage” *IAEA*, 1999, Wien.

(2) International Atomic Energy Agency (IAEA), ”Storage of Spent Nuclear Fuel – Specific Safety Guide” *IAEA Safety Standards Series* no. SSG-15, IAEA, 2020, Wien.

(3) Swedish Nuclear Fuel Supply Co., Division KBS, ”Final Storage of Spent Nuclear Fuel – KBS-3” *Report*, 1983, Stockholm.

(4) Nilsson L. B.; Thegerström, C. ”The Swedish KBS-3 concept and program for continued R&D work” *Proceedings, American Nuclear Society*, 1984, 77–84.

(5) National Research Council ”A Review of the Swedish KBS-3 Plan for Final Storage of Spent Nuclear Fuel” *National Academy Press*, 1984, Washington, D.C.

(6) Swedish Nuclear Fuel and Waste Management Company (SKB) ”Deep Repository for Spent Nuclear Fuel. SR 97 – Post-closure Safety” *SKB-report*, 1999, Stockholm.

(7) Nuclear Energy Agency (NEA) ”An International Review of: SR 97 – Post-closure Safety of a Deep Repository for Spent Nuclear Fuel in Sweden” *OECD Publishing*, 2000, Paris.

(8) SKB, “Post-closure safety for the final repository for spent nuclear fuel at Forsmark” Main report, PSAR version. SKB Technical Report TR-21-01, 2022, Svensk Kärnbränslehantering AB.

(9) World Nuclear Association ”Uranium Enrichment” *World Nuclear Association*. Available online: https://world-nuclear.org/information-library/nuclear-fuel-cycle/conversion-enrichment-and-fabrication/uranium-enrichment.aspx (updated June 2025, accessed 18 Oct 2025).

(10) U.S. Nuclear Regulatory Commission, ”Uranium Enrichment (Fact Sheet)” *NRC*. Available online: https://www.nrc.gov/materials/fuel-cycle-fac/ur-enrichment.html (updated Dec 2020, accessed 18 Oct 2025).

(11) Pastina B.; LaVerne, J. A., ”An Alternative Conceptual Model for the Spent Nuclear Fuel–Water Interaction in Deep Geological Disposal Conditions” *Applied Sciences*, 2021, 11(18), 8566.

(12) Rai D.; Felmy, A. R.; Ryan, J. L., ”Uranium(IV) Hydrolysis Constants and Solubility Product of $UO_2{\cdot}xH_2O$(am)” *Inorganic Chemistry*, 1990, 29(2), 260–264.

(13) Yan, Y.; Çevirim-Papaioannou, N.; Gaona, X.; Fellhauer, D.; Altmaier, M., ”Thermodynamic description of U(IV) solubility and hydrolysis in chloride systems: Pitzer activity model for the system U^{4+}–Na^{+}–Mg^{2+}–Ca^{2+}–H^{+}–Cl^{-}–OH^{-}–H_2O(l)” *Applied Geochemistry*, 2024, 171, 106091.

(14) Steward, S. A.; Mones, E. T. ”Comparison and Modeling of Aqueous Dissolution Rates of Various Uranium Oxides” *MRS Online Proceedings Library*, 1996, 465, 557–564.

(15) Sutton, M.; Warwick, P.; Hall, A.; Jones, C., ”Carbonate-induced dissolution of uranium-containing precipitates under cement leachate conditions” *Journal of Environmental Monitoring*, 1999, 1, 177–182.

(16) Jung, E. C.; Cho, H.-R.; Baik, M. H.; Kim, H.; Cha, W. ”Time-resolved laser fluorescence spectroscopy of $UO_2(CO_3)_3^{4-}$” *Dalton Transactions*, 2015, 44, 18831–18838.

(17) Scanlan, J. P., ”Equilibria in uranyl carbonate systems—II: The overall stability constant of $UO_2(CO_3)_2^{2-}$ and the third formation constant of $UO_2(CO_3)_3^{4-}$” *Journal of Inorganic and Nuclear Chemistry*, 1977, 39(4), 635–639.

(18) Ciavatta, L.; Ferri, D.; Grenthe, I.; Salvatore, F.; Spahiu, K., ”Studies on metal carbonate equilibriums. 4. Reduction of the tris(carbonato)dioxouranate(VI) ion, $UO_2(CO_3)_3^{4-}$, in hydrogen carbonate solutions” *Inorganic Chemistry*, 1983, 22(14), 2088–2092.

(19) SKB, ”Safety Analysis SFR 1. Long-term Safety” *SKB Rapport R-08-130*, 2008, ISSN 1402-3091.

(20) Nuclear Energy Agency (NEA), ”The Safety Case for Deep Geological Disposal of Radioactive Waste: 2013 State of the Art. Symposium Proceedings” *OECD/NEA*, 2013, France.

(21) Spinks J. W. T.; Woods, R. J., ”An Introduction to Radiation Chemistry (3rd ed.)” *John Wiley & Sons*, 1990, New York/Toronto.

(22) Christensen H.; Sunder, S., ”Current State of Knowledge of Water Radiolysis Effects on Spent Nuclear Fuel Corrosion” *Nuclear Technology*, 2000, 131(1), 102–123.

(23) Koppenol, W. H.; Liebman, J. F., ”The oxidizing nature of the hydroxyl radical. A comparison with the ferryl ion (FeO^{2+})” *The Journal of Physical Chemistry*, 1984, 88(1), 99–101.

(24) Armstrong, D. A.; Huie, R. E.; Koppenol, W. H.; Lymar, S. V.; Merényi, G.; Neta, P., Ruscic, B.; Stanbury, D. M.; Steenken, S.; Wardman, P., ”Standard electrode potentials involving radicals in aqueous solution: Inorganic radicals” *Pure and Applied Chemistry*, 2015, 87(11–12), 1139–1150.

(25) Schumb, W. C.; Satterfield, C. N.; Wentworth, R. L., ”Hydrogen Peroxide” *Armed Services Technical Information Agency (ASTIA)*, 1953, Ohio.

(26) Greenwood, N. N.; Earnshaw, A., ”Chemistry of the Elements (2nd ed.)” *Butterworth-Heinemann/Elsevier*, 1997, Oxford.

(27) Sutherland, K. M.; Grabb, K. C.; Karolewski, J. S.; Taenzer, L.; Hansel, C. M.; Wankel, S. D., ”The redox fate of hydrogen peroxide in the marine water column” *Limnology and Oceanography*, 2021, 66(10), 3828–3841.

(28) Cooper, W. J.; Zepp, R. G., ”Hydrogen peroxide decay in waters with suspended soils: evidence for biologically mediated processes” *Canadian Journal of Fisheries and Aquatic Sciences*, 1990, 47(5), 888–893.

(29) Ortiz V.; Rubio, M. A.; Lissi, E. A., ”Hydrogen peroxide decomposition in rain and dew waters” *Atmospheric Environment*, 2000, 34(7), 1139–1146.

(30) Ekeroth E.; Roth O.; Jonsson, M., ”The relative impact of radiolysis products in radiation induced oxidative dissolution of UO_2” *Journal of Nuclear Materials*, 2006, 355(1–3), 38–46.

(31) Shoesmith, D. W.; Sunder, S.; Bailey, M. G.; Wallace, G. J., ”The corrosion of nuclear fuel (UO_2) in oxygenated solutions” *Corrosion Science*, 1989, 29, 1115–1128.

(32) Sunder, S.; Shoesmith, D. W.; Lemire, R. J.; Bailey, M. G.; Wallace, G. J., ”The effect of pH on the corrosion of nuclear fuel (UO_2) in oxygenated solutions” *Corrosion Science*, 1991, 32(4), 373–386.

(33) Hocking, W. H.; Betteridge, J. S.; Shoesmith, D. W., ”The cathodic reduction of dioxygen on uranium oxide in dilute alkaline aqueous solution” *Journal of Electroanalytical Chemistry*, 1994, 379(1–2), 339–351.

(34) Barreiro Fidalgo, A.; Kumagai, Y.; Jonsson, M., ”The role of surface-bound hydroxyl radicals in the reaction between H_2O_2 and UO_2” *Journal of Coordination Chemistry*, 2018, 71(11–13), 1799–1807.

(35) El Jamal, G.; Li, J.; Jonsson, M., ”H_2O_2-induced oxidative dissolution of UO_2 in saline solutions” *European Journal of Inorganic Chemistry*, 2021, 2021(40), 4175–4182.

(36) Montaigne, T.; Szenknect, S.; Broudic, V.; Imbert, P.-H.; Tocio, F.; Martin, C.; Miserque, F.; Jégou, C.; Dacheux, N., ”Oxidative dissolution of (U,Ce)O_2 materials in aqueous solutions containing H_2O_2” *npj Materials Degradation*, 2023, 7, 34.

(37) Kumagai, Y.; Barreiro Fidalgo, A.; Jonsson, M., ”Impact of stoichiometry on the mechanism and kinetics of oxidative dissolution of UO_2 induced by H_2O_2 and γ-irradiation” *The Journal of Physical Chemistry C*, 2019, 123(15), 9919–9925.

(38) Shoesmith, D. W.; Sunder, S.; Johnson, L. H.; Bailey, M. G., ”Oxidation of CANDU UO_2 fuel by the alpha-radiolysis products of water” *MRS Online Proceedings Library*, 1985, 50, 309–316.

(39) Sunder, S.; Shoesmith, D. W.; Johnson, L. H.; Wallace, G. J.; Bailey, M. G.; Snaglewski, A. P., ”Oxidation of CANDU™ fuel by the products of the alpha-radiolysis of groundwater” *MRS Online Proceedings Library*, 1986, 84, 103–113.

(40) Sunder, S.; Shoesmith, D. W.; Christensen, H.; Bailey, M. G.; Miller, N. H., ”Electrochemical and X-ray Photoelectron Spectroscopic Studies of UO_2 Fuel Oxidation by Specific Radicals Formed During Radiolysis of Groundwater” *MRS Online Proceedings Library*, 1988, 127, 317–324.

(41) Sunder, S.; Shoesmith, D. W.; Christensen, H.; Miller, N. H., ”Oxidation of UO_2 fuel by the products of gamma radiolysis of water” *Journal of Nuclear Materials*, 1992, 190, 78–86.

(42) Suzuki T.; Abdelouas, A.; Grambow, B.; Mennecart, T.; Blondiaux, G., ”Oxidation and dissolution rates of UO_2(s) in carbonate-rich solutions under external alpha irradiation and initially reducing conditions” *Radiochimica Acta*, 2006, 94, 567–573.

(43) Christensen H.; Sunder S.; Shoesmith D. W., ”Development of a Kinetic Model to Predict the Rate of Oxidation and Dissolution of Nuclear Fuel (UO_2) by the Radiolysis of Water” *AECL-11102, COG-93-488*, 1994, AECL, Chalk River.

(44) Willis, B. T. M., ”Structures of UO_2, UO_{2+x} and U_4O_9 by neutron diffraction” *Journal de Physique (France)*, 1964, 25(5), 431–439.

(45) Rouse, K. D.; Willis, B. T. M.; Pryor, A. W., ”Anharmonic Contributions to the Debye–Waller Factors of UO_2” *Acta Crystallographica*, 1968, 24, 117–122.

(46) Cooper, R. I.; Willis, B. T. M., ”Refinement of the structure of β-U_4O_9” *Acta Crystallographica*, 2004, 60(4), 322–325.

(47) Loopstra, B. O., ”Neutron diffraction investigation of U_3O_8” *Acta Crystallographica*, 1964, 17, 651–654.

(48) Andresen, A. F., ”The structure of U_3O_8 determined by neutron diffraction” *Acta Crystallographica*, 1958, 11, 612–614.

(49) Debets, P. C., ”The structure of β-UO_3” *Acta Crystallographica*, 1966, 21, 589-593.

(50) Loopstra, B. O.; Taylor, J. C.; Waugh, A. B., ”Neutron powder profile studies of the gamma uranium trioxide phases” *Journal of Solid State Chemistry*, 1977, 20(1), 9–19.

(51) Weller M. T., Dickens P. G., Penny D. J., ”The structure of δ-UO_3” *Polyhedron*, 1988, 7(3), 243–244.

(52) Garrido F.; Ibberson, R. M.; Nowicki, L.; Willis, B. T. M., ”Cuboctahedral oxygen clusters in U_3O_7” *Journal of Nuclear Materials*, 2003, 322(1), 87–89.

(53) Leinders G.; Bes, R.; Kvashnina, K. O.; Verwerft, M., ”Local Structure in U(IV) and U(V) Environments: The Case of U_3O_7” *Inorganic Chemistry*, 2020, 59(7), 4576–4587.

(54) Perrot, A.; Canizares, A.; Miro, S.; Claparede, L.; Podor, R.; Sauvage, T.; Peuget, S.; Jégou, C.; Dacheux, N., ”In situ Raman monitoring of studtite formation under alpha radiolysis in ^{18}O-labeled water” *Journal of Nuclear Materials*, 2024, 600, 155267.

(55) Teterin, Y. A.; Popel, A. J.; Maslakov, K. I.; Teterin, A. Y.; Ivanov, K. E.; Kalmykov, S. N., Springell, R.; Scott, T. B.; Farnan, I., ”XPS Study of Ion Irradiated and Unirradiated UO_2 Thin Films” *Inorganic Chemistry*, 2016, 55(16), 8059–8070.

(56) Li, J.; Liu, X.; Jonsson, M., ”Exploring the change in redox reactivity of UO_2 induced by exposure to oxidants in HCO_3^- solutions” *Inorganic Chemistry*, 2023, 62(19), 7413–7423.

(57) Kern, D. M. H.; Orlemann, E. F., ”The Potential of the Uranium(V), Uranium(VI) Couple and the Kinetics of Uranium(V) Disproportionation in Perchlorate Media” *Journal of the American Chemical Society*, 1949, 71(6), 2102–2106.

(58) Pastina, B.; LaVerne, J. A., ”Effect of molecular hydrogen on hydrogen peroxide in water radiolysis” *The Journal of Physical Chemistry A*, 2001, 105(40), 9316–9322.

(59) Jégou C.; Muzeau, B.; Broudic V.; Peuget, S.; Poulesquen, A.; Roudil, D.; Corbel, C., ”Effect of external gamma irradiation on dissolution of the spent UO_2 fuel matrix” *Journal of Nuclear Materials*, 2005, 341(1), 62–82.

(60) Trummer, M.; Jonsson, M., “Resolving the H_2 effect on radiation induced dissolution of UO_2-based spent nuclear fuel” Journal of Nuclear Materials, 2010, 396(1-2), 163-169.

(61) Thomas, L. E.; McCarthy, J. M.; Gilbert, E. R., ”TEM examination of oxidized LWR spent fuel” *Third International Spent Fuel Storage Technology Symposium/Workshop: Proceedings*, 1986, 2, 40-51.

(62) Clark, R. A.; Conroy, M. A.; Lach, T. G.; Buck, E. C.; Pellegrini, K. L.; McNamara, B. K.; Schwantes, J. M., ”Distribution of metallic fission-product particles in the cladding liner of spent nuclear fuel” *npj Materials Degradation*, 2020, 4, 4.

(63) Buck, E. C.; Mausolf, E. J.; McNamara, B. K.; Soderquist, C. Z.; Schwantes, J. M., ”Nanostructure of metallic particles in light water reactor used nuclear fuel” *Journal of Nuclear Materials*, 2015, 461, 236–243.

(64) Broczkowski, M. E.; Noël, J. J.; Shoesmith, D. W., “The inhibiting effects of hydrogen on the corrosion of uranium dioxide under nuclear waste disposal conditions” Journal of Nuclear Materials, 2005, 346(1), 16-23.

(65) Trummer, M.; Nilsson, S.; Jonsson, M., ”On the effects of fission product noble metal inclusions on the kinetics of radiation induced dissolution of spent nuclear fuel” Journal of Nuclear Materials, 2008, 378(1), 55-59.

(66) Trummer, M.; Roth, O.; Jonsson, M., “H_2 inhibition of radiation induced dissolution of spent nuclear fuel” Journal of Nuclear Materials, 2009, 383(3), 226-230.

(67) Maier., A. C.; Jonsson, M., “Pd-catalyzed surface reactions of importance in radiation induced dissolution of spent nuclear fuel involving H_2” ChemCatChem, 2019, 11(20), 5108-5115.

(68) Hansson, N. L.; Jonsson, M., ”Exploring H_2-effects on radiation-induced oxidative dissolution of UO_2-based spent nuclear fuel using numerical simulations” Radiation Physics and Chemistry, 2023, 210, 111055.

(69) Graham, T., “On the absorption and dialytic separation of gases by colloid septa” Philosophical Transactions, 1866, 156, 399-439.

(70) Park J.; Lee, D. W.; Jeong, H.; Lee, J.; Noh, H. R.; Kim, T.-H.; Kim, J.-Y.; Lim, S. H.; Ryu, H. J.; Choi, S., ”Effect of hydrogen on oxidative dissolution of epsilon particles-doped UO_2 pellets under carbonate condition with hydrogen peroxide” *Journal of Nuclear Materials*, 2025, 603, 155381.

(71) Briggs, D.; Seah, M. P. (Ed.), ”Practical Surface Analysis by Auger and X-ray Photoelectron Spectroscopy” *John Wiley & Sons*, 1983, Chichester.

(72) Hüfner, S., ”Photoelectron Spectroscopy: Principles and Applications (3rd ed.)” *Springer-Verlag*, 2003, Berlin Heidelberg.

(73) Moulder, J. F.; Stickle, W. F.; Sobol, P. E.; Bomben, K. D., ”Handbook of X-ray Photoelectron Spectroscopy” *Perkin-Elmer, Physical Electronics Division*, 1992, Eden Prairie, MN.

(74) Seah, M. P.; Gilmore, I. S.; Beamson, G., ”XPS: Binding energy calibration of electron spectrometers 5 — a re-assessment of the reference energies” *Surface and Interface Analysis*, 1998, 26, 642–649.

(75) Greczynski, G.; Hultman, L., ”A step-by-step guide to perform X-ray photoelectron spectroscopy” *Journal of Applied Physics*, 2022, 132(1), 011101.

(76) El Jamal, G.; Gouder, T.; Eloirdi, R.; Jonsson, M., ”Monitoring the gradual change in oxidation state during surface oxidation or reduction of uranium oxides by photoemission spectroscopy of the 5f states” *Journal of Nuclear Materials*, 2022, 560, 153504.

(77) Powell, C. J., ”Practical guide for inelastic mean free paths, effective attenuation lengths, mean escape depths, and information depths in X-ray photoelectron spectroscopy” *Journal of Vacuum Science & Technology A*, 2020, 38, 023209.

(78) Chambers, S. A.; Du, Y., ”Experimental determination of electron attenuation lengths in complex materials by means of epitaxial film growth: Advantages and challenges” *Journal of Vacuum Science & Technology A*, 2020, 38, 043409.

(79) Gouder, T.; Eloirdi, R.; Caciuffo, R., ”Direct observation of pure pentavalent uranium in U_2O_5 thin films by high-resolution photoemission spectroscopy” *Scientific Reports*, 2018, 8, 8306.

(80) Laidler, K. J., ”Chemical Kinetics (3rd ed.)” *Pearson Education Inc.*, 1987, New York.

(81) Shizu, K.; Kaji, H., ”Quantitative prediction of rate constants and its application to organic emitters” *Nature Communications*, 2024, 15, 4723.

(82) Joseph, J. M.; Choi, B. S.; Yakabuskie, P.; Wren; J. C., ”A combined experimental and model analysis on the effect of pH and O_2(aq) on γ-radiolytically produced H_2 and H_2O_2” *Radiation Physics and Chemistry*, 2008, 77(9), 1009–1020.

(83) Schortmann, W. E.; DeSesa, M. A., ”Topical Report WIN-89: Kinetics of the dissolution of uranium dioxide in carbonate-bicarbonate solutions” *U.S. Atomic Energy Commission*, 1958, Washington, D.C.

(84) McEachern, R. J., Taylor, P., ”A review of the oxidation of uranium dioxide at temperatures below 400 °C” *Journal of Nuclear Materials*, 1998, 254(2–3), 87–121.

(85) Huang Y.; Zhang, L.; Ji, H.; Zhang, Z.; Zhang, Q.; Sun, B.; Liu, H.; Song, H., ”The chemisorption thermodynamics of O_2 and H_2O on AFM UO_2 surfaces unraveled by DFT+U-D3 study” *Applied Surface Science*, 2025, 708, 163687.

(86) Arts I.; Saniz, R.; Baldinozzi, G.; Leinders, G.; Verwerft, M.; Lamoen, D., ”Ab initio study of the adsorption of O, O_2, H_2O and H_2O_2 on UO_2 surfaces using DFT+U and non-collinear magnetism” Journal of Nuclear Materials, 2024, 599, 155249.

(87) Langmuir, I., ”The adsorption of gases on plane surfaces of glass, mica and platinum” The Research Laboratory of The General Electric Company, 1918, 1361–1402.

(88) van Santen, R. A.; Niemantsverdriet, J. W., ”Chemical Kinetics and Catalysis” *Springer Science + Business Media*, 1995, New York.

(89) van't Hoff, J. H., ”Études de dynamique chimique” *Frederik Muller & Co.*, 1884, Amsterdam.

(90) Arrhenius, S. A., ”Über die Dissociationswärme und den Einfluß der Temperatur auf den Dissociationsgrad der Elektrolyte” *Zeitschrift für Physikalische Chemie*, 1889, 4, 96–116.

(91) Eyring, H., ”The Activated Complex in Chemical Reactions” *Journal of Chemical Physics*, 1935, 3(2), 107–115.

(92) de Pablo, J.; Casas, I.; Giménez, J.; Molera, M.; Rovira, M.; Duro, L.; Bruno, J., ”The oxidative dissolution mechanism of uranium dioxide. I. The effect of temperature in hydrogen carbonate medium” *Geochimica et Cosmochimica Acta*, 1999, 63(19–20), 3097–3103.

(93) de Pablo, J.; Casas, I.; Giménez, J.; Molera, M.; Torrero, M. E., ”Effect of temperature and bicarbonate concentration on the kinetics of $UO_2(s)$ dissolution under oxidizing conditions” *MRS Proceedings*, 1996, 465, 535-542.

(94) Nicol, M. J.; Needes, C. R. S., ”The anodic dissolution of uranium dioxide – II in carbonate solutions” *Electrochimica Acta*, 1977, 12, 1381–1384.

(95) Puigdomenech, I.; Bruno, J., ”Modelling uranium solubilities in aqueous solutions: Validation of a thermodynamic data base for the EQ3/6 geochemical codes” *SKB Technical Report 88-21*, 1988, Stockholm.

(96) Blake, C. A.; Coleman, C. F.; Brown, K. B.; Hill, D. G.; Lowrie, R. S.; Schmitt, J. M., ”Studies in the carbonate-uranium system” *Journal of the American Chemical Society*, 1956, 78, 5978–5983.

(97) Sergeyeva, E. I.; Nikitin, A. A.; Khodakovskiy, I. L.; Naumov, G. B., ”Experimental investigation of equilibria in the system UO_3–CO_2–H_2O in 25–200 °C temperature interval” *Geochemistry International*, 1972, 9, 900–910.

(98) Grenthe, I.; Ferri, D.; Salvatore, F.; Riccio, G., ”Studies on metal carbonate equilibria. Part 10. A solubility study of complex formation in the uranium(VI)–

water–carbon dioxide system at 25 °C" *Journal of the Chemical Society, Dalton Transactions*, 1984, 2439–2443.

(99) Chen, R.; Avotinsh, Y.; Freeman, G. R., "Solvent effects on the reactivity of solvated electrons with ions in isobutanol/water mixed solvents" *Canadian Journal of Chemistry*, 1994, 72, 1083–1093.

(100) Zhestkova, T. P.; Obruch, A. N.; Pikaev, A. K., "Radiolysis of concentrated solutions of sodium nitrate in D_2O" *High Energy Chemistry*, 1992, 26, 329–332.

(101) Peiris, S. A.; Freeman, G. R., "Solvent structure effects on solvated electron reactions with ions in 2-butanol/water mixed solvents" *Canadian Journal of Chemistry*, 1991, 69, 884–892.

(102) Sedigallage, A. P.; Freeman, G. R., "Solvent structure effects on solvated electron reactions in mixed solvents: Negative ions in 1-propanol-water and 2-propanol-water" *Canadian Journal of Physics*, 1990, 68, 940–946.

(103) Logager, T.; Sehested, K., "Formation and decay of peroxynitrous acid: A pulse radiolysis study" *Journal of Physical Chemistry*, 1993, 97, 6664–6669.

(104) Smaller, B.; Avery, E. C.; Remko, J. R., "EPR pulse radiolysis studies of the hydrogen atom in aqueous solution. I. Reactivity of the hydrogen atom" *Journal of Chemical Physics*, 1971, 55, 2414–2418.

(105) Khan, M. H.; Warwick, P.; Evans, N., "Spectrophotometric determination of uranium with arsenazo III in perchloric acid" *Chemosphere*, 2006, 63, 1165–1169.

(106) Jauberty, L.; Drogat, N.; Decossas, J.-L.; Delpech, V.; Gloaguen, V.; Sol, V., "Optimization of the arsenazo III method for the determination of uranium in water and plant samples" *Talanta*, 2013, 115, 751–754.

(107) Golmohammadi, H.; Rashidi, A.; Safdari, S. J., "Simple and rapid spectrophotometric method for determination of uranium(VI) in low-grade uranium ores using arsenazo III" *Chemistry & Chemical Technology*, 2012, 6(3), 245–249.

(108) Ghormley, J. A.; Stewart, A. C., "Effects of γ-radiation on ice I" *Journal of the American Chemical Society*, 1956, 78, 2934–2939.

(109) Wei, Y.-J.; Liu, C.-G.; Mo, L.-P., "Ultraviolet absorption spectra of iodine, iodide ion and triiodide ion" *Chinese Journal of Spectroscopy*, 25(1), 2005, 86–88 [PMID 15852827].

(110) Rahn, R. O.; Stefan, M. I.; Bolton, J. R.; Goren, E.; Shaw, P.-S.; Lykke, K. R., "Quantum yield of the iodide–iodate chemical actinometer: Dependence on wavelength and concentration" *Photochemistry and Photobiology*, 2007, 78(2), 146–152.

(111) Štefanić, I.; Asmus, K.-D.; Bonifačić, M., ”Quantification of iodide oxidation by trichloromethyl peroxyl radicals and $I^- + I_2 \rightleftharpoons I_3^-$ equilibrium in alcohol/water mixtures” *Physical Chemistry Chemical Physics*, 2003, 5(13), 2783–2789.

(112) Li, Q.; Sritharathikhun, P.; Motomizu, S., ”Development of a novel reagent for Hantzsch reaction for determination of formaldehyde by spectrophotometry and fluorometry” *Analytical Sciences*, 2007, 23(4), 413–417.

(113) Munhoven, G., ”Mathematics of the total alkalinity–pH equation – pathway to robust and universal solution algorithms: the SolveSAPHE package v1.0.1” *Geoscientific Model Development*, 2013, 6, 1367–1388.

(114) Bielski, B. H. J.; Allen, A. O., ”Mechanism of the disproportionation of superoxide radicals” *Journal of Physical Chemistry*, 1977, 81(11), 1048–1050.

(115) Bielski, B. H. J., ”Reevaluation of the spectral and kinetic properties of HO_2 and O_2^- free radicals” *Photochemistry and Photobiology*, 1978, 28(4–5), 645–649.

(116) Rabani, J.; Nielsen, S. O., ”Absorption spectrum and decay kinetics of O_2^- and HO_2 in aqueous solutions by pulse radiolysis” *Journal of Physical Chemistry*, 1969, 73(11), 3736–3744.

(117) Perrin D. D., ”Ionisation Constants of Inorganic Acids and Bases in Aqueous Solution (2nd ed.)” *Pergamon Press*, 1983, Oxford.

(118) Cai, Z.; Li X.; Katsumura, Y.; Urabe, O., ”Radiolysis of bicarbonate and carbonate aqueous solutions: Product analysis and simulation of radiolytic processes” *Nuclear Technology*, 2001, 136(2), 231–240.

(119) Draganic, Z. D.; Negron-Mendoza, A.; Sehested, K.; Vujosevic, S. I.; Navarro-Gonzalez, R.; Albarran-Sanchez, M. G.; Draganic, I. G., ”Radiolysis of aqueous solutions of ammonium bicarbonate over a large dose” *Radiation Physics and Chemistry*, 1991, 38, 317–321.

(120) Eriksen, T. E.; Lind, J.; Merényi, G., ”On the acid–base equilibrium of the carbonate radical” *Radiation Physics and Chemistry*, 1985, 26, 197–199.

(121) Buxton, G. V.; Greenstock, C. L.; Helman, W. P.; Ross, A. B., ”Critical review of rate constants for reactions of hydrated electrons, hydrogen atoms and hydroxyl radicals ($\cdot OH/\cdot O^-$) in aqueous solution” *Journal of Physical and Chemical Reference Data*, 1988, 17, 513–886.

(122) Christensen, H.; Sehested, K.; Corfitzen, H.; ”Reactions of hydroxyl radicals with hydrogen peroxide at ambient and elevated temperatures” *Journal of Physical Chemistry*, 1982, 86, 1588–1590.

(123) Elliot, A. J.; McCracken, D. R.; Buxton, G. V.; Wood, N. D., ”Estimation of rate constants for near-diffusion-controlled reactions in water at high temperatures” *Journal of the Chemical Society, Faraday Transactions*, 1990, 86, 1539–1547.

(124) Elliot, A. J., ”A pulse radiolysis study of the temperature dependence of reactions involving H, OH and e^{-}_{aq} in aqueous solutions” *Radiation Physics and Chemistry*, 1989, 34, 753–758.

(125) Janata, E.; Schuler, R. H., ”Rate constant for scavenging e^{-}_{aq} in N_2O-saturated solutions” *Journal of Physical Chemistry*, 1982, 86, 2078–2084.

(126) Sweet, J. P.; Thomas, J. K., ”Absolute rate constants for H-atom reactions in aqueous solutions” *Journal of Physical Chemistry*, 1964, 68, 1363–1368.

(127) Czapski, G.; Peled, E., ”On the pH dependence of $G_{reducing}$ in the radiation chemistry of aqueous solutions” *Israel Journal of Chemistry*, 1968, 6, 421–436.

(128) Weinstein, J.; Bielski, B. H. J., ”Kinetics of the interaction of HO_2 and O_2^- radicals with hydrogen peroxide – The Haber–Weiss reaction” *Journal of the American Chemical Society*, 1979, 101, 58–62.

(129) Olsson, D.; Aydogan, H.; Jonsson, M., ”The influence of bicarbonate concentration and ionic strength on peroxide speciation and overall reactivity towards UO_2” *RSC Advances*, 2024, 14, 16248–16254.

(130) Delacroix, D.; Guerre, J.-P.; Leblanc, P.; Hickman, C., ”Radionuclide and Radiation Protection Data Handbook (2nd ed.)” *Radiation Protection Dosimetry*, Nuclear Technology Publishing, 2002.

(131) Stumpf, S.; Seibert, A.; Gouder, T.; Huber, F.; Wiss, T.; Römer, J., ”Development of fuel-model interfaces: Investigations by XPS, TEM, SEM and AFM” *Journal of Nuclear Materials*, 2009, 385, 208–211.

(132) Stumpf S.; Seibert, A.; Gouder, T.; Huber, F.; Wiss, T., Römer, J.; Denecke, M. A., ”Development of fuel-model interfaces: Characterization of Pd containing UO_2 thin films” *Journal of Nuclear Materials*, 2010, 397(1–3), 19–26.

(133) Eloirdi, R.; Cakir, P.; Huber, F.; Seibert, A; Konings, R.; Gouder, T., ”X-ray photoelectron spectroscopy study of the reduction and oxidation of uranium and cerium single oxide compared to (U–Ce) mixed oxide films” *Applied Surface Science*, 2018, 457, 566–571.

(134) Thangavelu, S. G.; Cahill, C. L., ”Uranyl-Promoted Peroxide Generation: Synthesis and Characterization of Three Uranyl Peroxo [$(UO_2)_2(O_2)$] Complexes” *Inorganic Chemistry*, 2015, 54(9), 4208–4221.

(135) Zanonato, P. L.; Di Bernardo, P.; Szabó, Z.; Grenthe, I., ”Chemical equilibria in the uranyl(VI)–peroxide–carbonate system: Identification of precursors for the formation of poly-peroxometallates” *Dalton Transactions*, 2012, 41, 11635–11641.

(136) Behar, D.; Czapski G.; Duchovny I., ”Carbonate radical in flash photolysis and pulse radiolysis of aqueous carbonate solutions” *Journal of Physical Chemistry*, 1970, 74, 2206–2210.

(137) Rigo, A.; Stevanato, R.; Finazzi-Agrò, A.; Rotilio G., ”An attempt to evaluate the rate of the Haber–Weiss reaction by using OH radical scavengers” *FEBS Letters*, 1977, 80, 130–132.

(138) Ferradini, C.; Foos J.; Houée C.; Pucheault, J., ”The reaction between superoxide anion and hydrogen peroxide” *Photochemistry and Photobiology*, 1978, 28, 697–700.

(139) Shilov, V. P.; Pikaev, A. K., “Issledovanie reaktsionnoj sposobnosti ionov urana i neptuniya otnositel’no atomov H v vodnykh rastvorakh metodom impul’snogo radioliza”. Khim. Vys. Energ. 1982, 16 (5), 468–469.

(140) Saini, R. D.; Bhattacharyya, P. K., “Radiolytic oxidation of U(IV) sulfate in aqueous solution by alpha particles from cyclotron”. Int. J. Radiat. Appl. Instrum., Part C. Radiat. Phys. Chem. 1987, 29(5), 375–379.

(141) Badley, M. D. M.; Shoesmith, D. W.; Noël, J. J., ”Effect of hydrogen on the dissolution of uranium dioxide in peroxide-containing environments” *Journal of The Electrochemical Society*, 2023, 170(9), 096506.

(142) Broczkowski, M. E.; Keech, P. G.; Noël, J. J.; Shoesmith, D. W., ”The role of dissolved hydrogen on rare earth–doped uranium dioxide corrosion in the presence of hydrogen peroxide” *Journal of The Electrochemical Society*, 2011, 158, C439

(143) Razdan, M.; Shoesmith, D. W.; ”The influence of hydrogen peroxide and hydrogen on the corrosion of simulated spent nuclear fuel” *Faraday Discussions*, 2015, 180, 283–299.

(144) Bauhn, L.; Hansson, N.; Ekberg, C.; Fors P.; Delville, R.; Spahiu, K., ”The interaction of molecular hydrogen with α-radiolytic oxidants on a (U,Pu)O_2 surface” *Journal of Nuclear Materials*, 2018, 505, 54–61.

(145) Collette, S.; Dufour, T.; Reniers, F., “Reactivity of water vapor in an atmospheric argon flowing post-discharge plasma torch” Plasma Sources Science and Technology, 2016, 25, 025014.

(146) Willis, C.; Boyd, W. A., “Excitation in the radiation chemistry of inorganic gases” Journal of Radiation Physics and Chemistry, 1976, 8, 71-111.

(147) Hartwig, C.; Sparwasser, K.; Jones, T. E.; Greiner, M., ”Isolated Pd atoms in a silver matrix: Spectroscopic and chemical properties” *Journal of Chemical Physics*, 2021, 154(18), 184703.

(148) Guo, Z.; Liu T.; Li W.; Zhang C.; Zhang D.; Pang Z., ”Carbon supported oxide-rich Pd–Cu bimetallic electrocatalysts for ethanol electrooxidation in alkaline media enhanced by Cu/CuOx” *Catalysts*, 2016, 6(5), 62.

(149) Hansson, N. L.; Tam, P. L.; Ekberg, C.; Spahiu, K., ”XPS study of external α-radiolytic oxidation of UO_2 in the presence of argon or hydrogen” *Journal of Nuclear Materials*, 2016, 543, 152604.